



MISSOURI
S&T

CENTER FOR TRANSPORTATION
INFRASTRUCTURE AND SAFETY



**Design, Construction and Load Testing
of the Pat Daly Road
Bridge in Washington County, MO,
with Internal Glass Fiber
Reinforced Polymers Reinforcement**

by

**Zhibin Lin, Mostafa Fakhairfar,
Chenglin Wu, Genda Chen, Wesley Bevans,
Arun Vijay Kumar Gunasekaran,
and Sahra Sedighsarvestani**

**NUTC
R275**

Disclaimer

The contents of this report reflect the views of the author(s), who are responsible for the facts and the accuracy of information presented herein. This document is disseminated under the sponsorship of the Department of Transportation, University Transportation Centers Program and the Center for Transportation Infrastructure and Safety NUTC program at the Missouri University of Science and Technology, in the interest of information exchange. The U.S. Government and Center for Transportation Infrastructure and Safety assumes no liability for the contents or use thereof.

Technical Report Documentation Page

1. Report No. NUTC R275	2. Government Accession No.	3. Recipient's Catalog No.	
4. Title and Subtitle Design, Construction and Load Testing of the Pat Daly Road Bridge in Washington County, MO, with Internal Glass Fiber Reinforced Polymers Reinforcement	5. Report Date January 10, 2013		6. Performing Organization Code
	8. Performing Organization Report No. Project #00034512		
7. Author/s Zhibin Lin, Mostafa Fakhairfar, Chenglin Wu, Genda Chen, Wesley Bevans, Arun Vijay Kumar Gunasekaran, and Sahra Sedighsarvestani	10. Work Unit No. (TRAIS)		11. Contract or Grant No. DTRT06-G-0014
9. Performing Organization Name and Address Center for Transportation Infrastructure and Safety/NUTC program Missouri University of Science and Technology 220 Engineering Research Lab Rolla, MO 65409	13. Type of Report and Period Covered Final		
	14. Sponsoring Agency Code		
12. Sponsoring Organization Name and Address U.S. Department of Transportation Research and Innovative Technology Administration 1200 New Jersey Avenue, SE Washington, DC 20590			
15. Supplementary Notes			
16. Abstract The overarching goal of this project is to deploy and assess an innovative corrosion-free bridge construction technology for long-term performance of new and existing bridges. The research objective of this project is to conduct a comprehensive study (instrumentation, construction, both laboratory and field evaluation) of a rapidly constructed and durable, three-span bridge with cast-in-place cladding steel reinforced concrete substructure and precast concrete decks/girders reinforced with glass fiber reinforced polymers (GFRP). The bridge has one conventional concrete-girder span, one conventional steel-girder span, and one innovative concrete box-girder span. The conventional concrete and steel girders were used to demonstrate the effective use of corrosion-free bridge decks in deck replacement projects and, as benchmarks, to demonstrate the pros and cons of the innovative concrete box girders. The bridge was instrumented with embedded strain gauges to monitor the strains at critical locations during load testing. The collected data will allow the understanding of load distribution in various GFRP bars of the innovative concrete box girders and bridge deck slabs. Specifically, a full-scale concrete box girder and a full-scale concrete slab with internal GFRP reinforcement were tested in the Highbay Structures Laboratory at Missouri S&T to ensure that the test bridge components behaved as designed prior to the field construction. Furthermore, in-situ load tests of the completed bridge were conducted to demonstrate the load capacity and behavior of individual components and the bridge as a system. The field validated technology will have a longlasting value for future deck replacement projects of existing bridges and new constructions. It will provide a viable alternative to conventional bridge systems/materials for the improvement of our Nation's deteriorating infrastructure.			
17. Key Words Bridge design, Corrosion-free concrete deck, GFRP bars, and bridge instrumentation	18. Distribution Statement No restrictions. This document is available to the public through the National Technical Information Service, Springfield, Virginia 22161.		
19. Security Classification (of this report) unclassified	20. Security Classification (of this page) unclassified	21. No. Of Pages 210	22. Price

Acknowledgments

Financial support for this study was provided in part by the Federal Highway Administration (FHWA) Innovative Bridge Research and Construction (IBRC) Program, by Washington County, MO, and by the U.S. Department of Transportation under the auspices of the Center for Transportation Infrastructure and Safety at Missouri S&T. Thanks are due to Hughes Brother, NE, for providing their engineering assistance related to the design and fabrication of glass or carbon fiber reinforced polymers (FRP) bars, Great River Associates, MO, for their overall bridge design and construction management, Washington County, MO, for their bridge construction and support during in-situ load tests, and Missouri Department of Transportation for overseeing the project activities from design through field construction to bridge inspection. In particular, the authors would like to express their sincere appreciations to Mr. Steve Brown and Mr. Darrel Whitman from Great River Associates, Mr. Marvin Wright and Mr. Todd Moyers from Washington County, and Mr. Dennis Krenning from Missouri Department of Transportation.

Special thanks go to Mr. Jason Cox (Sr. Research Specialist) at Missouri University of Science and Technology (Missouri S&T) for his coordination and expertise in FRP applications and construction, Mr. John Bullock, Mr. Brian Swift, and Mr. Gary Abbott at Missouri S&T for their assistances in laboratory and field tests. We are also grateful to Dr. Ying Huang (recently graduated from Missouri S&T and took an Assistant Professor position at North Dakota State University), Mr. Fujian Tang (Ph.D. candidate), Mr. Yi Bao (Ph.D. candidate), and Mr. Brandon Schafer (M.S. student) at Missouri S&T for their help in the course of the research project.

EXECUTIVE SUMMARY

The existing culvert located on the Pat Daly Road over Arnault Branch, Washington County, MO, was an unreinforced, slab-on-ground concrete structure with two corrugated steel pipes running parallel through the concrete underneath the roadway as water passages. The culvert was structurally inadequate and functionally obsolete, and posed a real safety issue when water passed over the structure during flood seasons.

In collaboration with Great River Associates (GRA), Springfield, MO, Missouri University of Science and Technology (Missouri S&T) proposed to replace the culvert with a rapidly constructed and durable, three-span bridge with precast concrete decks and box girders reinforced with glass fiber reinforced polymers (GFRP) bars and cast-in-place cladding steel reinforced concrete substructure, striving for high corrosion resistance and durability of the bridge structure.

To ensure that the technologies validated in this project can be applied into both new construction and the deck replacement of existing bridges, one conventional steel-girder span, one conventional concrete-girder span, and one innovative concrete box-girder span were designed and built as the bridge superstructure. The conventional steel- and concrete-girder structures provide two popular benchmarks for the box-girder superstructure. Each span of the bridge was 21 ft wide and 27 ft long, totaling 81 ft in length of the entire bridge. Specifically, the first and third spans were composed of three precast deck slabs that were supported on five steel- or concrete-girders and post-tensioned longitudinally at the bridge site. The idea of using GFRP as flexural and shear reinforcement would be implemented with relevant implications from both the structural and constructability standpoints.

The middle span had four precast box girders, each reinforced with GFRP bars and simply supported on piers at both ends. The box girders were transversely post-tensioned at the bridge site to close the longitudinal joints between them. This span represents a new application of GFRP bars in the design of precast box girders. In this way, no additional bridge deck needs to be cast at the bridge site and no separate bridge slabs need to be cast at precast yards, enabling the accelerated construction of future short-span bridges. The proposed bridge was constructed by the Washington County crew except that the post-tensioning of carbon fiber reinforced polymer (CFRP) bars was completed by Missouri S&T. The bridge deck was finished with an approximately 3 in. asphalt overlay wearing surface.

The bridge was instrumented with embedded sensors to monitor the strain at critical locations during load testing in the laboratory and at the bridge site. Prior to field construction, a full-size, 27-ft long and 5-ft wide box girder and a full-size 9-ft long and 21-ft wide deck slab with GFRP reinforcement were tested in the Highbay Structures Laboratory at Missouri S&T. The load capacities of both the tested slab and box girder exceeded their respective design values and thus validated their original designs. About one month after the completion of construction, the bridge was tested under one or two dump trucks with full loads. The test results demonstrated that the new bridge behaved as expected in terms of the bridge stiffness and the strain distribution among GFRP bars. The maximum deflection under the full design loads was significantly smaller than the specified allowable value in design codes. Therefore, the constructed three-span bridge met all the design requirements and was ready to be put in operation.

Table of Contents

List of Figures	xii
List of Tables	xvi
Nomenclature	xvii
Chapter 1. Introduction	1
1.1 Introduction.....	1
1.2 The existing Pat Daly Road culvert	1
1.3 New bridge with innovative material and construction	2
1.4 Objectives	3
1.5 Report organization.....	4
Chapter 2. Literature Review of Bridge Systems	9
2.1 Introduction.....	9
2.2 Literature review.....	9
2.2.1 Performance of existing bridges	9
2.2.2 Corrosion control in bridge systems	10
2.2.3 Structural health monitoring with applications to bridges.....	11
2.3 Summary.....	12
Chapter 3. Review on GFRP-bar Reinforced Concrete Design	15
3.1 Introduction.....	15
3.2 The bridge substructure	15
3.3 The bridge superstructure	16
3.3.1 Concrete deck slabs reinforced with GFRP bars	16
3.3.2 Concrete box girders reinforced with GFRP bars.....	17
3.4 Summary.....	17
Chapter 4. Bridge Instrumentation and Monitoring System	23
4.1 Introduction.....	23
4.2 General monitoring guidelines.....	23
4.2.1 Sensors	24
4.2.2 Data collection and monitoring system.....	25
4.3 Sensor arrays.....	27
4.3.1 Sensor layout and placement	28
4.3.2 Long-term strain gauges installations	29
4.4 Summary.....	30
Chapter 5. Precast of GFRP-bar Reinforced Concrete Bridge Elements and Accelerated Bridge Construction	39
5.1 Introduction.....	39
5.2 Precast of bridge deck slabs and box girders	40
5.2.1 Concrete	40
5.2.2 GFRP bar	40
5.2.3 Precast bridge elements.....	41
5.3 Construction of bridges.....	43
5.3.1 Construction management and procedures	43

5.3.2 Bridge substructure components and concrete/steel girders	44
5.3.3 Bridge deck slabs	45
5.3.4 Bridge box girders.....	46
5.3.5 Internal unbounded post-tension of the bridge system	47
5.4 Summary	48
Chapter 6. Overview of Laboratory and Field Test Programs	65
6.1 Introduction.....	65
6.2 Laboratory testing program of bridge elements.....	65
6.3 Load rating for field tests.....	65
6.3.1 Load rating.....	65
6.3.2 Truck weight and size	66
6.4 Truck positions and load protocols for field tests.....	67
6.4.1 Truck position along the longitudinal direction.....	67
6.4.2 Truck pass along the transverse direction.....	68
6.4.3 Load protocol for field tests	68
6.5 Instrumentation plan for field tests	69
6.5.1 Instrumentation Layout.....	69
6.5.2 Data collection	71
6.6 Summary.....	71
Chapter 7. Performance of GFRP-bar Reinforced Concrete Slabs.....	99
7.1 Introduction.....	99
7.2 Laboratory test program.....	99
7.2.1 Test schemes	99
7.2.2 Test setups.....	100
7.2.3 Instrumentation Plan	101
7.2.4 Load protocols	102
7.3 Laboratory test results and discussion	103
7.3.1 Flexural behavior	103
7.3.2 Shear behavior	106
7.4 Field test program.....	108
7.4.1 Instrumentation Plan	108
7.4.2 Load protocols for field testing.....	109
7.5 Field test results and discussion.....	109
7.5.1 Longitudinal distribution of vertical deflections.....	109
7.5.2 Transverse distribution of vertical deflections.....	110
7.5.3 Dynamic deflection and impact factor for live load	111
7.6 Summary.....	112
Chapter 8. Performance of GFRP-bar Reinforced Box Girders.....	147
8.1 Introduction.....	147
8.2 Laboratory test program.....	147
8.2.1 Test schemes	147
8.2.2 Test setups.....	148
8.2.3 Instrumentation plan	149
8.2.4 Load protocols	150
8.3 Laboratory test results and discussion	151

8.4 Field test program	153
8.4.1 Instrumentation plan	153
8.4.2 Load protocols for field testing.....	153
8.5 Field test results and discussion.....	153
8.5.1 Longitudinal distribution of deflections.....	154
8.5.2 Transverse distribution of deflections.....	155
8.5.3 Dynamic deflection and live load impact factor	155
8.6 Summary.....	156
Chapter 9. Conclusions and Recommendations.....	181
9.1 Project Summary.....	181
9.2 Conclusions.....	182
9.3 Recommendations.....	184
References.....	185
Appendix A: Strain Gauges (Half-bridge) Installation and Protection Procedures for Long-term Bridge Monitoring.....	191

List of Figures

Figure 1.1: Location map of the bridge replacement over Arnault branch creek, Washington County, Mo	6
Figure 1.2: New three-span bridge over Arnault branch creek, Washington County, Mo	7
Figure 2.1: Missouri deteriorated bridge deck (from the Missouri Department of Transportation in http://minnesota.publicradio.org/display/web/2008/02/11/missouri_bridges/)	13
Figure 2.2: Epoxy coated steel reinforcement used in bridge deck (http://minnesota.publicradio.org/display/web/2008/02/11/missouri_bridges/).....	13
Figure 2.3: Damaged epoxy coating and rebar corrosion	14
Figure 2.4: FRP reinforcement in concrete deck (http://www.engr.wisc.edu/centers/wsmtl/WSMTL-WEB-pg02R-NEWS-IBRC-I.htm).....	14
Figure 3.1: Layout of the new three-span bridge.....	19
Figure 3.2: GFRP bar reinforcement layout for steel-girder supported deck slabs	19
Figure 3.3: GFRP bar reinforcement layout for concrete-girder supported deck slabs	20
Figure 3.4: Connection details of the Washington County Bridge.....	21
Figure 3.5: Detailed GFRP bar reinforcement layout for concrete box girder	21
Figure 4.1: Architectures of SmartBrick motherboard (left) and daughterboard (right)	31
Figure 4.2: Half-bridge configuration and multiplexer in SmartBrick Daughterboard	31
Figure 4.3: Prototype daughterboard in SmartBrick for strain gauge measurement	32
Figure 4.4: Instrumentation layout in GFRP reinforced box-girder span of the Washington County Bridge.....	32
Figure 4.5: Longitudinal strain gauges layout in the GFRP reinforced box-girder span.....	33
Figure 4.6: Transverse strain gauges layout in the GFRP reinforced box-girder span.....	34
Figure 4.7: Strain gauges layout in the GFRP reinforced concrete deck of the concrete- or steel-girder span	35
Figure 4.8: Strain gauges installation on GFRP bars.....	36
Figure 4.9: Preparation of GFRP-bar cages with installed sensors for the precast plant.....	37
Figure 5.1: Wrapped and sand-coated GFRP bar	51
Figure 5.2: GFRP-bar cages.....	52
Figure 5.3: Steel formwork for concrete deck slab at the precast plant.....	52
Figure 5.4: Form work for casting concrete deck slab in prefab plant	53
Figure 5.5: Integral construction of bridge curb with deck slab (upside down casting).....	54
Figure 5.6: Strain sensors in concrete deck slab	54
Figure 5.7: Formwork for concrete box girder	54
Figure 5.8: Finished precast elements.....	55
Figure 5.9: Transportation of precast bridge elements	55
Figure 5.10: Erection steps of the bridge	56

Figure 5.11: Placement of GFRP-bar reinforced concrete deck slabs	57
Figure 5.12: Completion of all concrete deck slabs on top of steel- and concrete- girders.....	58
Figure 5.13: Installation of CFRP tendons for post-tensioning	58
Figure 5.14: Placement of GFRP-bar reinforced concrete box girders	59
Figure 5.15: Pulling through CFRP tendons for post-tensioning	60
Figure 5.16: Bridge girders seated on a rubber pad.....	60
Figure 5.17: The newly erected three-span bridge.....	60
Figure 5.18: Schematics of a post-tensioned, steel-girder deck (3 slabs) with ten CFRP tendons	61
Figure 5.19: Schematics of a post-tensioned box-girder deck (4 girders) with five CFRP tendons (3 fractured during installation).....	61
Figure 5.20: Post-tensioning of one CFRP tendon	62
Figure 5.21: Overview of the bridge.....	63
Figure 6.1: Overview of laboratory test setups for full-scale precast bridge elements.....	74
Figure 6.2: Trucks used in field tests	75
Figure 6.3: Preliminary design of load protocol for field tests	76
Figure 6.4: Determination of truck location in longitudinal direction for field tests.....	77
Figure 6.5: Determination of truck location (pass) in transverse direction for field tests	82
Figure 6.6: Schematics of locations of truck passes and stops	84
Figure 6.7: Illustrated four stops of one truck over each span.....	85
Figure 6.8: Load cases SSLC 011 to SSLC 014	86
Figure 6.9: Load cases SSLC 021 to SSLC 024.....	87
Figure 6.10: Load cases SSLC 031 to SSLC 034	88
Figure 6.11: Load cases SDLC 041 and SDLC 042 (one truck, dynamic with $v=35$ mph)	89
Figure 6.12: Load cases DSLC 051 to DSLC 054(two trucks, static).....	90
Figure 6.13: Load cases DDLC 061 and DDLC 062 (two trucks, dynamic with $v=15$ mph)	91
Figure 6.14: Stop signs and traffic control.....	92
Figure 6.15: DC-LVDT transducers layout (red dots).....	93
Figure 6.16: Accelerometer layout (red dots).....	94
Figure 6.17: Inclinometer layout (red dots)	95
Figure 6.18: Installation process of representative sensors	96
Figure 6.19: Data collection and acquisition system used in field testing.....	97
Figure 7.1: Laboratory test schemes for a full-size concrete slab.....	115
Figure 7.2: Photos of the laboratory setup for concrete slab testing.....	116
Figure 7.3: Details of slab test setup.....	117
Figure 7.4: Data acquisition and calibration devices	118
Figure 7.5: DC-LVDTs for box girder tests.....	118
Figure 7.6: Calibration of a DC-LVDT with calibration block	118

Figure 7.7: Instrumentation layout for Load Case 1	119
Figure 7.8: Load protocol for flexural tests (Load Case 1).....	120
Figure 7.9: Load protocol for shear tests (Load Case 2).....	120
Figure 7.10: Crack pattern during the slab test with initial cracks observed at 10 kips	121
Figure 7.11: Flexural failure process	122
Figure 7.12: Slab failure by concrete crushing at compression zone	123
Figure 7.13: Load-deflection curves at various locations.....	125
Figure 7.14: Stress-strain curve at mid-span bottom GFRP bar	125
Figure 7.15: Load-strain curves of GFRP bars at various locations	125
Figure 7.16: Stress-strain curves for quarter span bottom GFRP bar (Load Case 1)	126
Figure 7.17: Setup for shear test in Load Case 2	127
Figure 7.18: Shear failure process and cracking propagation.....	128
Figure 7.19: Slab failure by shear	129
Figure 7.20: GFRP bar condition at shear failure	130
Figure 7.21: Overview of the collapsed slab after two load cases.....	130
Figure 7.22: Load-deflection curves at various locations	132
Figure 7.23: Load-strain curves for quarter span GFRP bar (Load Case 2).....	132
Figure 7.24: DC-LVDTs layout on each span in field test	133
Figure 7.25: Inclinator layout on each span in field tests	134
Figure 7.26: Accelerometer layout on each span in field tests	135
Figure 7.27: Deflection distribution along north exterior steel girder under various load cases	137
Figure 7.28: Deflection distribution along center steel girder under various load cases.....	139
Figure 7.29: Transverse distribution of deflections of the steel-girder span under various load cases	141
Figure 7.30: Mid-span deflection time history	142
Figure 7.31: Dynamic effects and impact factor for live load due to truck(s).....	146
Figure 8.1: Schematic of laboratory test setup for concrete box girder.....	158
Figure 8.2: Photos of laboratory test setup for concrete box girder.....	159
Figure 8.3: Attachment details at supports and loading mechanism	160
Figure 8.4: Instrumentation layout.....	161
Figure 8.5: Load protocol of the box girder.....	162
Figure 8.6: Crack development and propagation.....	163
Figure 8.7: Box girder failure by concrete crushing in compression zone	164
Figure 8.8: Crack pattern across the span	165
Figure 8.9: Shear failure details	166
Figure 8.10: Load-displacement curves at various locations.....	168
Figure 8.11: Stress-strain curves of GFRP bars at mid-span	168
Figure 8.12: Static deflections of north exterior box girder under various load cases	170

Figure 8.13: Static deflections of north interior box girder under various load cases	172
Figure 8.14: Static deflections at mid-span of multiple box girders under various load cases	174
Figure 8.15: Deflection time histories at mid-span.....	175
Figure 8.16: Dynamic effects and impact factor for live load due to truck(s).....	179
Figure 9.1: Preparation for strain gauge installation.....	191
Figure 9.2: Installation of strain gauges.....	193
Figure 9.3: Soldering and protection of strain gauges	194

List of Tables

Table 4.1: Number of strain gauges used.....	32
Table 5.1: Material properties of Aslan 100 GFRP bars	50
Table 6.1: Truck axle spacing.....	72
Table 6.2: Loading case records in field tests.....	73

Nomenclature

A_f	=	Area of GFRP bars
b_w	=	Width of the concrete member
d	=	Effective depth from extreme compression fiber to the centroid of GFRP bars
E_f, E_c	=	Young's modulus of GFRP reinforcement and concrete
f'_c	=	Compressive strength of concrete
f_r	=	Modulus of rupture
f_{ut}	=	Ultimate tensile strength of GFRP bars
I_g	=	Moment of inertia for uncracked section
L	=	Span length
M_{cr}	=	Cracking moment of concrete
P	=	Applied load
P_{cr}	=	Applied load corresponding to cracking moment
w_c	=	Weight of concrete
\bar{y}	=	Distance from the extreme compression fiber to the neutral axis of the cross section
ρ_f	=	GFRP reinforcement ratio
ϵ_{ut}	=	Ultimate strain of GFRP bars
ϕ	=	Reduction factor for GFRP bar ultimate strength

Chapter 1. Introduction

1.1 Introduction

The final design of the Pat Daly Road Bridge over the Arnault Branch Creek in Washington County, Missouri, as shown in Figure 1.1 was presented in Yan et al. (2010). This report mainly summarizes the long-term instrumentation, precast and construction of corrosion-free GFRP-bar reinforced bridge decks and girders, the laboratory validation of the final design of a representative bridge deck and a representative box girder, and the understanding of the bridge system stiffness and strain distribution among various GFRP bars under static and moving loads in field condition.

1.2 The existing Pat Daly Road culvert

The existing culvert was located on the Pat Daly Road over Arnault Branch Creek in Washington County, MO. The culvert was a 5 ft (1.52 m) thick unreinforced concrete slab-on-ground structure with a total length of 40 ft (12.19 m) and width of 15 ft (4.57 m). The approach roadway was 16 ft (4.88 m) wide. Two 3 ft (0.91 m) diameter corrugated steel pipes ran parallel through the concrete underneath the roadway and allowed water flowing in normal situations. The culvert structure was functionally obsolete and structurally inadequate, posing a safety threat. For example, the roadway was frequently submerged under water during severe floods in recent years due to a) insufficient height of the roadway, and b) insufficient discharge of the two through-concrete pipes. The floods resulted in disruption to passing traffic and gradually eroded away the roadway pavement that is in need of continuous maintenance. The affected local residents were forced to detour for at least 30 minutes. Therefore, the Washington County

Commission decided to replace the culvert with a rapidly-constructed, corrosion-free, elevated bridge as schematically shown in Figure 1.2.

1.3 New bridge with innovative material and construction

In collaboration with Great River Associates, Springfield, MO, Missouri S&T proposed to replace the culvert with a durable three-span bridge with precast concrete decks and girders with internal GFRP reinforcing bars and with cast-in-place cladding steel reinforced concrete substructure. As illustrated in Figures 1.2a through 1.2c, the new bridge had three 27 ft (8.23 m) long simply-supported spans with a total length of 81 ft (24.69 m), and an out-to-out deck width of 21 ft (6.40 m). The increased roadway length and height above the creek water will minimize the risk of floods, while the increased roadway width will improve the traffic safety in normal operations.

To ensure that the technologies validated in this project can be applied into both new construction and the deck replacement of existing bridges, one conventional steel-girder span, one conventional concrete-girder span, and one innovative concrete box-girder span were designed and built for the bridge superstructure. The conventional concrete- and steel-girder structures provide two popular benchmarks for the box-girder superstructure. Specifically, the first and third spans were composed of three GFRP-reinforced precast deck slabs that were supported on five steel girders and five concrete girders, respectively, and post-tensioned longitudinally with carbon fiber reinforced polymers (CFRP) bars at the bridge site. The middle span had four precast box girders, each reinforced with GFRP bars and simply supported on piers at both ends. The box girders were transversely post-tensioned with CFRP bars at the bridge site to close the longitudinal joints between them. This span represents a new application of GFRP bars in the design of precast box girders.

The proposed bridge was constructed by the Washington County crew except that the post-tensioning of all CFRP bars was completed by Missouri S&T. The bridge deck was finished with an approximately 3 in. (7.62 mm) asphalt overlay wearing surface. The bridge deck slabs and box girders were instrumented with embedded sensors to monitor the strain at critical locations during load testing in the laboratory and at the bridge site. Prior to field constructions, a full-size, 27 ft (8.23 m) long and 5 ft (1.52 m) wide box girder and a full-size 9 ft (2.74 m) long and 21 ft (6.40 m) wide deck slab with GFRP reinforcement were tested in the Highway Structures Laboratory at Missouri S&T. The load capacities of both the tested slab and box girder exceeded their respective design values and thus validated their original designs. About one month after the completion of construction, the bridge was tested under one or two dump trucks with full loads. The test results demonstrated that the new bridge behaved as expected in terms of the bridge stiffness and the strain distribution among GFRP bars. In addition, the deflection of the constructed bridge is significantly less than the allowable deflection specified in AASHTO Bridge Design Specifications.

1.4 Objectives

The overarching goal of this project is to deploy and assess an innovative corrosion-free bridge construction technology for long-term performance of new and existing bridges. The research objective of this project is to conduct a comprehensive study (instrumentation, construction, both laboratory and field evaluation) of a rapidly constructed, corrosion-free, three-span bridge with cast-in-place cladding steel reinforced concrete substructure and precast concrete decks/girders reinforced with GFRP bars. The scope of work included:

- 1) Develop and deploy a smart sensor system for long-term monitoring of the bridge superstructure;
- 2) Conduct laboratory testing of a full-size precast concrete deck slab and a full-size precast concrete box girder for performance validation of the bridge designs;
- 3) Cast in place two intermediate wall piers and two abutments that are reinforced with high grade cladding steel;
- 4) Erect precast box girders and precast bridge slabs with post-tensioning as well as build two cast-in-place wall piers and two abutments; and
- 5) Perform field testing of the completed bridge for the understanding of the bridge behavior under service loads (operational load rating), live load impact factor, lateral load distribution and global stiffness characteristics.

1.5 Report organization

This report is organized as follows. Both the existing culvert and the new bridge on the Pat Daly Road are introduced in Chapter 1. A brief review of bridge deteriorations is provided in Chapter 2. The basic bridge design, including GFRP-bar reinforced concrete deck slabs and concrete box girders, is described in Chapter 3. Instrumentation of the bridge deck slabs and concrete box-girders, and the development of a wireless structural health monitoring system are discussed in Chapter 4. Precast and field constructions of the GFRP-bar reinforced concrete bridge system are documented in Chapter 5. Laboratory and field test programs are briefly described in Chapter 6. The performances of GFRP-bar reinforced concrete bridge deck slabs both in laboratory and field tests are discussed in Chapter 7 while the performances of GFRP-bar

reinforced concrete box girders are presented in Chapter 8. In addition to a summary of main conclusions, future research topics are identified in Chapter 9.

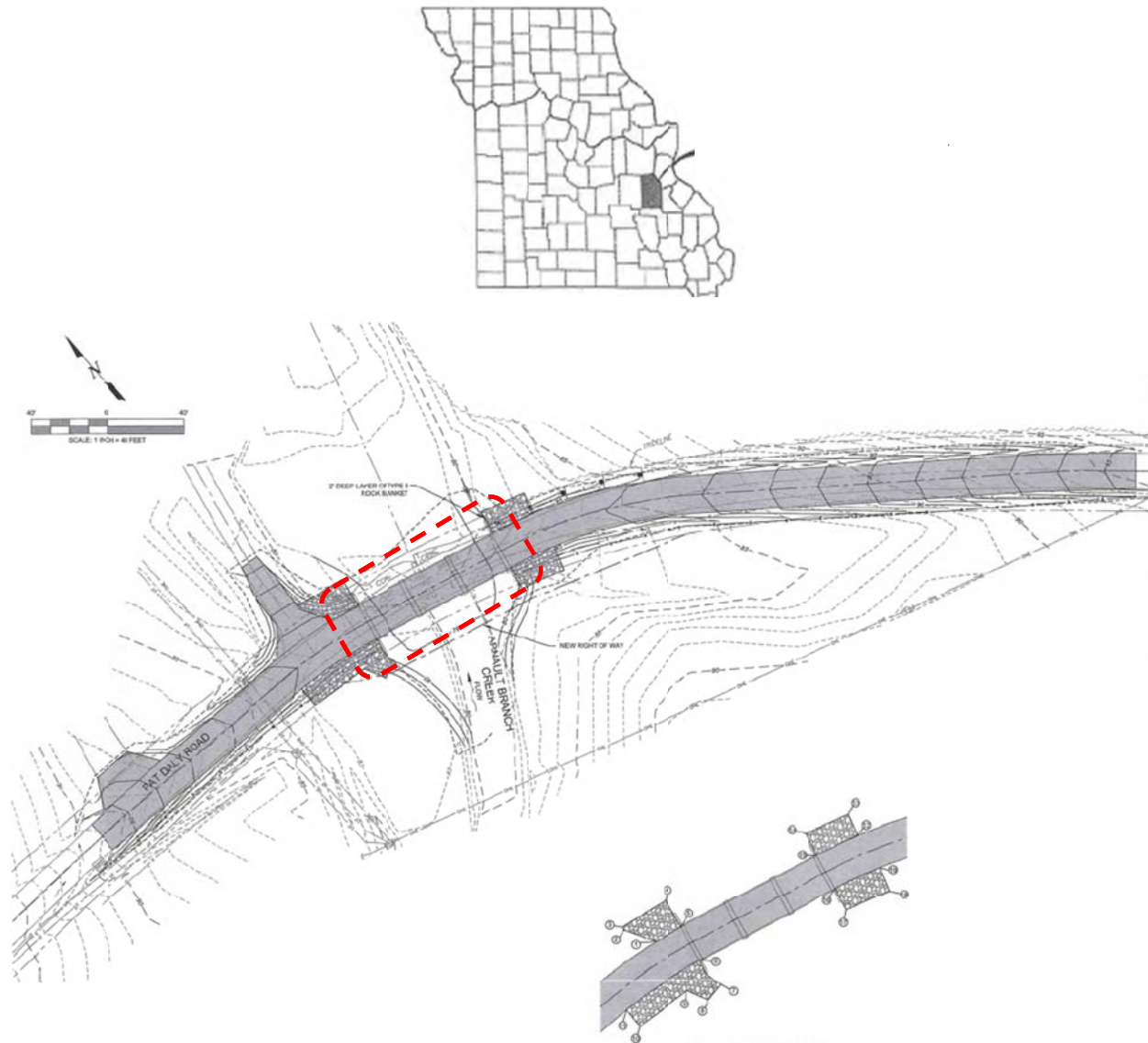
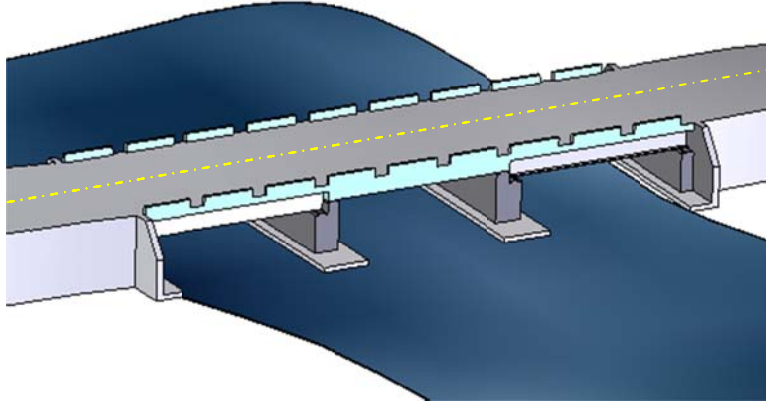
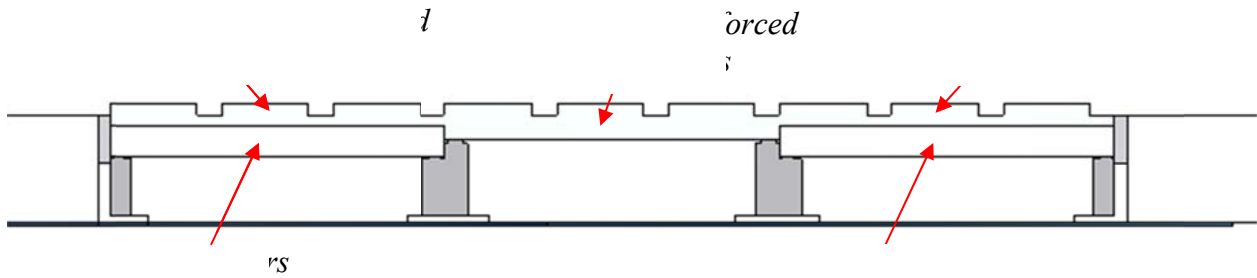


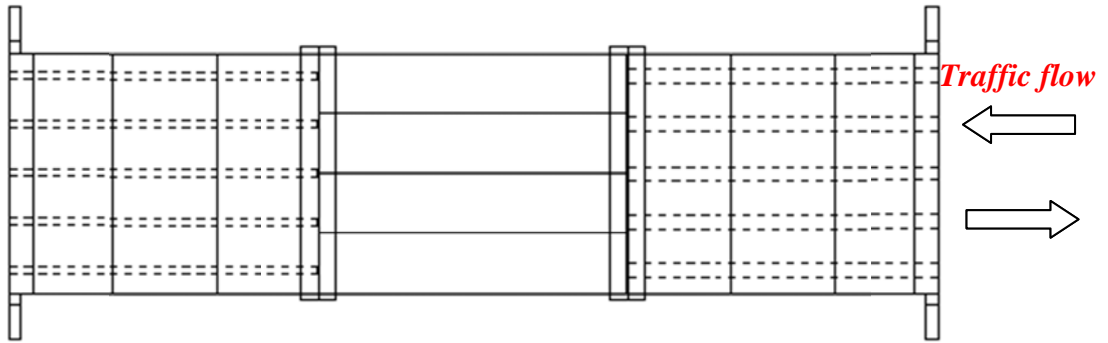
Figure 1.1: Location map of the bridge replacement over Arnault branch creek, Washington County, Mo



(a) Isometric view



(b) Elevation view



(c) Plan view

Figure 1.2: New three-span bridge over Arnault branch creek, Washington County, Mo

Chapter 2. Literature Review of Bridge Systems

2.1 Introduction

Structural degradation of transportation infrastructures due to environmental and loading effects is a growing concern both nationally and internationally (ACI Committee 201 and CEB, 1999). It could cause a significant safety hazard to bridges as a critical component of transportation networks. According to the U.S. Federal Highway Administration (FHWA), approximately 15 % of the bridges in the National Bridge Inventory are structurally deficient. This statistics underscores the importance of structural condition assessment for an effective maintenance and preservation of existing bridges.

2.2 Literature review

2.2.1 Performance of existing bridges

Our nation's 590,000 bridges and their transportation network are backbone of the U.S. economy in moving natural resources, agricultural products, industrial goods, and people. Mainly constructed in the 1950s and 1960s, the U.S. bridges are approximately 45 years old on the average. Even 50 % of the newer bridges age over 35 years old. According to FHWA (2006; 2008), it would cost \$140 billion to repair all deficient bridges in 2006. The actual cost would increase due to inflation and rising construction costs over time since addressing all deficient bridges at once is financially impractical. In addition, bridge deck deterioration is a continuous process that is affected by the bridge design, material selection, construction, environmental attacks, and traffic loading. The environmental attacks on bridge decks may include freeze/thaw actions on concrete in saturated or near-saturated conditions; scaling of concrete exposed to

deicing salts; and chloride penetration and the resulting corrosion of steel reinforcements, as typically shown in Figure 2.1. Thus, concrete bridge decks need multiple repairs and even replacements during the design lifespan of bridges (Cady and Weyers, 1984; Elzafraney and Soroushian, 2005). Daily truck traffic might cause fatigue-related damage to bridge decks (Oh, 1999; Laman and Ashbaugh, 2000; Boothby and Laman, 1999; Lin et al., 2012). Laboratory studies (Aldea et al., 1999 and Lin et al., 2012) have indicated the possibility of damaging bridge decks and other elements due to chloride ions ingress. Thus, corrosion of reinforcement (Bertolini et al., 2004) in bridge systems plays an essential role in the durability and service life of bridges (ACI Committee 201 and CEB, 1999).

2.2.2 Corrosion control in bridge systems

Among various corrosion control methods (Mehta and Gerwick, 1982; Sarja and Vesikari, 1996), epoxy coating has been widely accepted for reinforcing steel bars in reinforced concrete structures as shown in Figure 2.2. Significant research has demonstrated that epoxy coated bars can decelerate the corrosion process of steel if it remains intact. However, epoxy coating is often subjected to local damage during shipping and handling as well as at construction sites. As illustrated in Figure 2.3, a pinhole defect or a breach that occurs during handling or placement at a construction site will cause an epoxy coated bar to degrade rapidly. In addition, both laboratory tests and field inspections indicate that epoxy-coated bars in a marine environment are susceptible to corrosion. Therefore, it is imperative to find alternative methods or materials with enhanced corrosion resistance or corrosion-free performance. For example, fiber reinforced polymer (FRP) products as exemplified in Figure 2.4 have received significant attentions in construction industries due to their corrosion-free, magnetics-immune, and high strength-to-weight ratio features.

2.2.3 Structural health monitoring with applications to bridges

Traditional structural health monitoring (SHM) techniques that require an in-situ evaluator are prohibitively expensive to address all deficient bridges and may be subjected to subjectivity. For these reasons, autonomous SHM has emerged as an increasingly active research area. Several wired SHM systems have recently been developed but are limited in applications due to their high cost, design restraint, and difficulty in installation. The high power requirement of wired SHM systems limits their deployment to the locations with easy access to the power grid, as portable power sources are rarely adequate. A more important constraint associated with the use of wired SHM systems is the wiring required to supply power and interconnect components of the systems. This difficulty in bridge retrofitting hampers the applicability of wired SHM systems in bridges.

Therefore, a number of wireless SHM systems have recently been developed to address the challenges associated with the wired SHM systems. Salient examples of these systems are described in the next section. Their sensing operations are typically carried out by low-power sensing nodes, which lack the data storage and processing capability required for producing meaningful information. Processing is often delegated to an onsite laptop computer, which is prone to hardware and software failures and consumes very high power in operation, which again limits the deployment of the SHM systems to structures with access to the power grid. To overcome the shortcomings associated with many existing wireless SHM systems, a new wireless monitoring system was designed to facilitate the collection of field data. For example, a Smart Brick network (Harms et al., 2010, Gunasekaran et al., 2012) has been proposed as a wireless and fully autonomous system for SHM activities. Central to the system is the Smart Brick base station that offers extensive SHM capabilities, including onboard and external sensors

for environmental and structural measurements such as temperature, strain, tilt, and vibration. The new smart sensor system and its application in bridges will be detailed in Chapter 4.

2.3 Summary

Steel corrosion is the main reason for accelerated deterioration in bridge decks and girders. Such an effect on the integrity and functionality of bridges cannot be completely removed unless corrosion-free materials are used in bridge construction. In this study, GFRP bars are used as main reinforcement and stirrups in bridge deck slabs and concrete box girders, which will be discussed in Chapter 3.



Figure 2.1: Missouri deteriorated bridge deck (from the Missouri Department of Transportation in http://minnesota.publicradio.org/display/web/2008/02/11/missouri_bridges/)

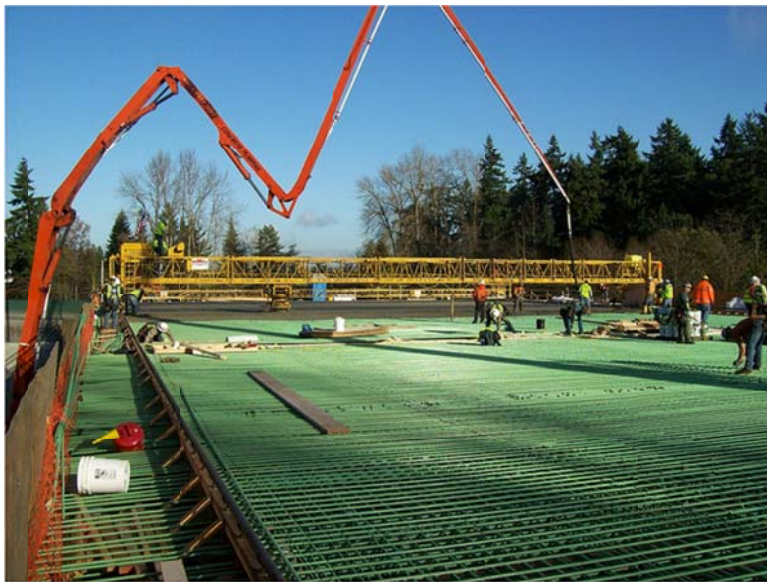


Figure 2.2: Epoxy coated steel reinforcement used in bridge deck (http://minnesota.publicradio.org/display/web/2008/02/11/missouri_bridges/)



Figure 2.3: Damaged epoxy coating and rebar corrosion



Figure 2.4: FRP reinforcement in concrete deck (<http://www.engr.wisc.edu/centers/wsmtl/WSMTL-WEB-pg02R-NEWS-IBRC-I.htm>)

Chapter 3. Review on GFRP-bar Reinforced Concrete Design

3.1 Introduction

The design approaches and calculations of the Pat Daly Road Bridge were summarized in Yan et al. (2010). Figures 3.1a through 3.1d present the overview and reinforcement detail of the bridge. To ensure that the validated technologies in this study are applicable to both new construction and the deck replacement of existing bridges, one conventional steel-girder span, one conventional concrete-girder span, and one innovative concrete box-girder span were considered for the bridge superstructure. The conventional steel- and concrete-girder structures served as good benchmarks for the box-girder structure. Their performance will be compared over time in an identical operating environment. Each span of the bridge was 21 ft (6.40 m) wide and 27 ft (8.23 m) long, totaling 81 ft (24.69 m) in length of the entire bridge. Specifically, the innovative strategies for bridge design and accelerated construction are introduced below.

3.2 The bridge substructure

The three spans are supported on two intermediate wall piers and two abutments, which in turn rest on reinforced concrete footings keyed into rocks by 6 in. The walls and abutments were concrete structures reinforced with high grade cladding steel (MMFX steel). The cladding steel has a microstructure that is fundamentally different from the conventional steel. Typical carbon steel forms a matrix of chemically dissimilar materials – carbide and ferrite. Carbide is strong but brittle – immovable at grain boundaries. In a moist environment, a microgalvanic cell forms between the carbide and the ferrite, resulting in a battery-like effect and destroying the steel from the inside out. This effect is the primary reason why carbon steel corrodes. On the

other hand, the cladding steel has a completely different structure at the nano or atomic scale. Steel made using the MMFX nanotechnology does not form any microgalvanic cell (the driving force behind corrosion of carbon steel). The “plywood” effect of MMFX steel gives the required strength, ductility, toughness and corrosion resistance in civil engineering applications. The use of MMFX steel in wall piers and abutments will allow for a complete non-corrosive system for the bridge substructure.

3.3 The bridge superstructure

3.3.1 Concrete deck slabs reinforced with GFRP bars

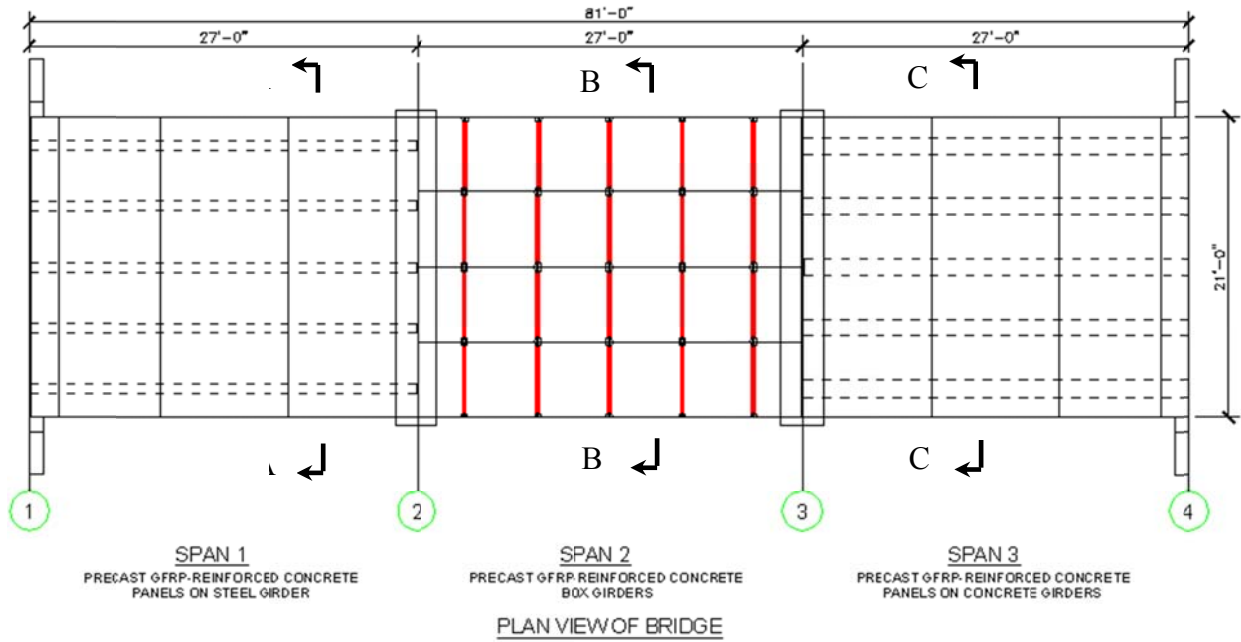
The two side spans with conventional steel and concrete girders have three precast deck slabs each. As displayed in Figures 3.2 and 3.3, the three precast deck slabs are reinforced with GFRP bars and supported on five steel girders and concrete girders, respectively. For each span, the three slabs were post tensioned longitudinally at the bridge site. The constructability and field performance of GFRP bars as flexural and shear reinforcement have been further demonstrated in the present project. The constructability of GFRP reinforcement will be optimized in order to reduce the material cost and make it competitive with standard steel cages. In this study, GFRP reinforcement was preassembled at the prefabricated site, greatly saving field construction time. The intellectual merit of the proposed solution lied in the ultimate exploitation of the inherent advantages of FRP materials following a rational design strategy and in the introduction of a standardized assembly reducing the high cost associated with the use of FRP reinforcement. To ensure that the deck slabs worked together with their supporting girders (partial composite action), several pockets as shown in Figures 3.4a and 3.4b were introduced and filled with non-shrink grout.

3.3.2 Concrete box girders reinforced with GFRP bars

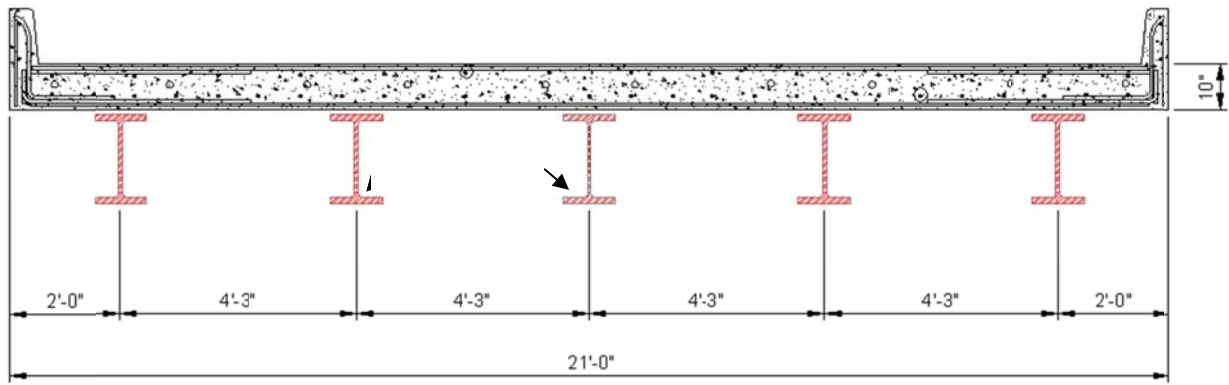
The middle span of the bridge consists of four precast, twin-cell hollow box girders that are all simply supported on two intermediate wall piers and transversely post tensioned at the bridge site to close the longitudinal joints between the girders. The box girders were reinforced with Aslan 100 GFRP bars that are manufactured by Hughes Brothers. They were designed in accordance with the AASHTO LRFD Specifications (2010) and ACI 440 1R-06 Specifications (2006). The cross section and longitudinal reinforcement layout of each hollow box girder are presented in Figure 3.5.

3.4 Summary

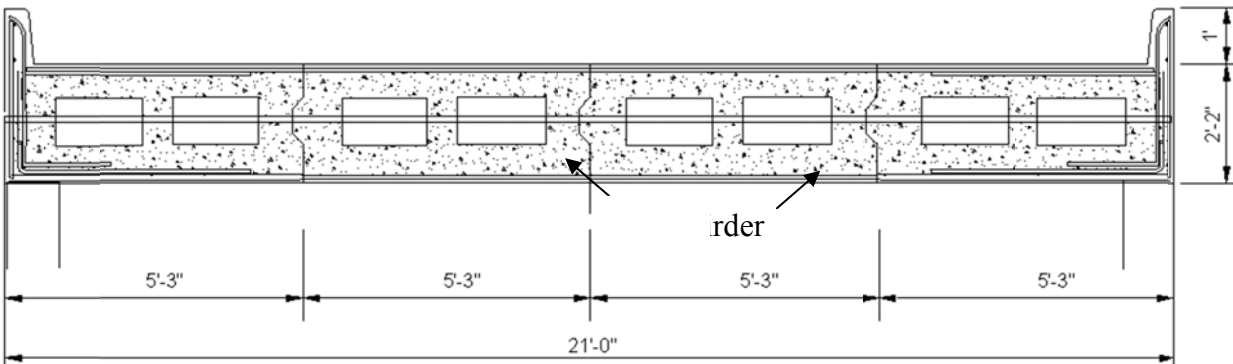
As aforementioned, the proposed bridge system consists of three spans, two side spans with three precast post-tensioned deck slabs rested on five steel and concrete girders, respectively, and the other middle span with four precast box girders. The precast deck slabs were erected and post-tensioned at the construction site to save significant construction time. The precast box girders were transversely post-tensioned at the bridge site to close the longitudinal joints between them. The middle span with precast box girders represents a new design of GFRP bars reinforced bridge, which requires no additional deck and further saves construction time. The end product would be a document summarizing the accumulated experience and performance data, enabling the accelerated construction of future short-span bridges.



(a) Plan view



(b) Concrete deck slab over steel girders (section A-A)



(c) Concrete box girders (section B-B)

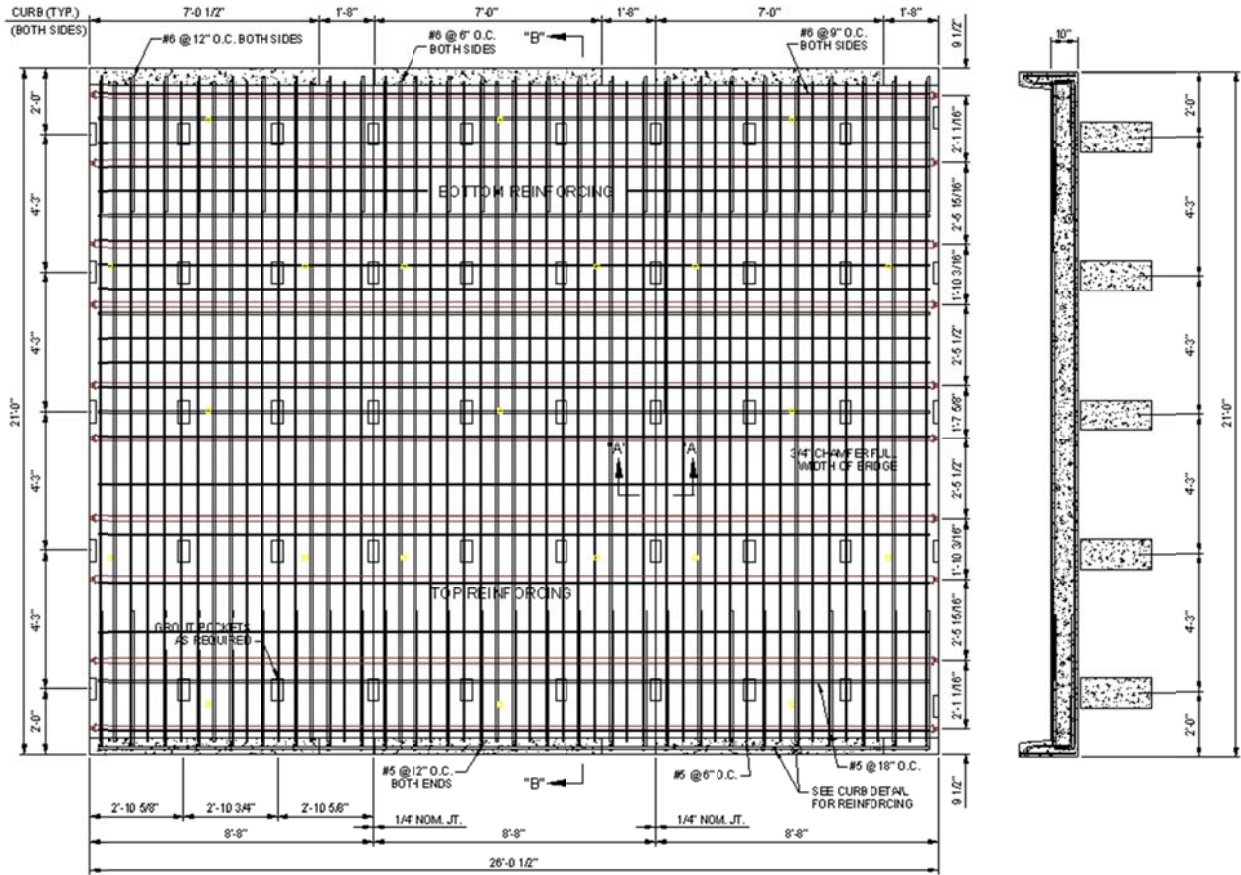
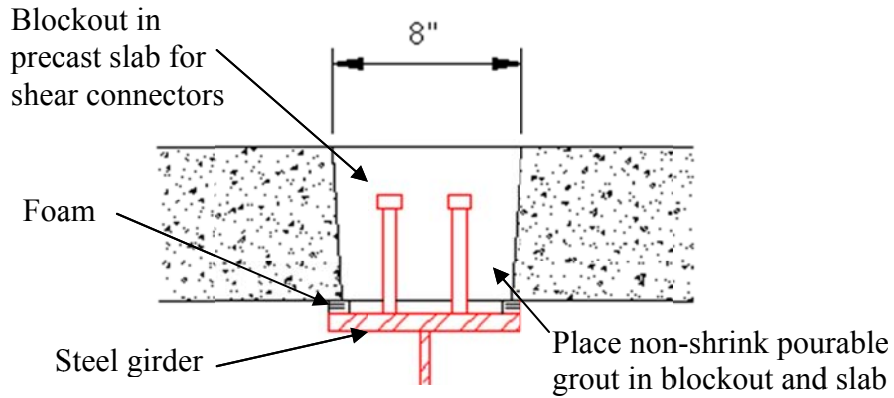
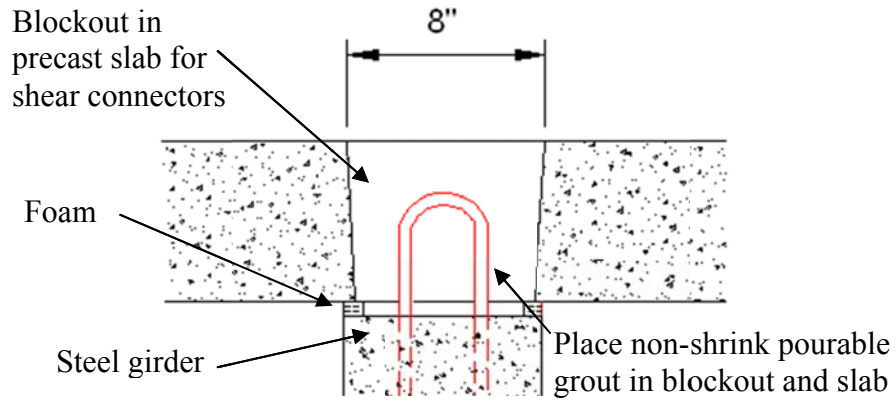


Figure 3.3: GFRP bar reinforcement layout for concrete-girder supported deck slabs



(a) Steel girder supported concrete deck slabs



(b) Concrete girder supported concrete deck slabs
 Figure 3.4: Connection details of the Washington County Bridge

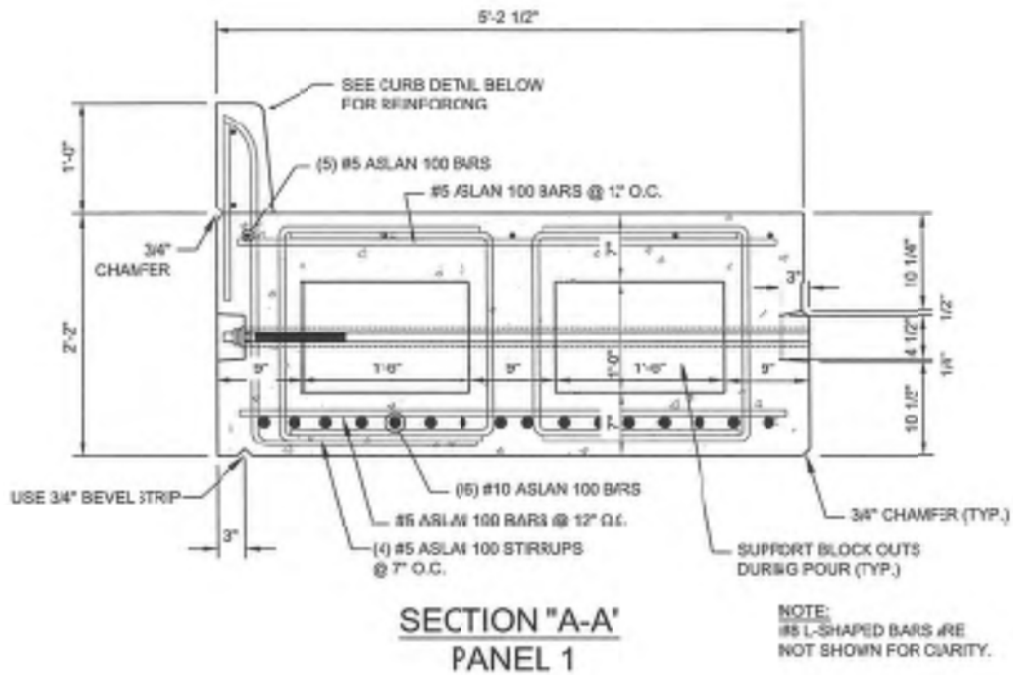


Figure 3.5: Detailed GFRP bar reinforcement layout for concrete box girder

Chapter 4. Bridge Instrumentation and Monitoring System

4.1 Introduction

The main objective of this chapter is to describe the planning, design and installation of a wireless monitoring system on the Pat Daly Road Bridge. The most significant feature of the bridge is the use of corrosion-free materials (FRP and cladding steel) for main reinforcement and stirrups. Therefore, the bridge is expected to be more durable than other conventional concrete bridges reinforced with carbon steel. Even so, bridge structures could deteriorate over time in non-corrosion forms due to environmental, overloading and other effects.

The unique design of the GFRP-bar reinforced concrete girder span and their comparison with two girder spans warrant the design and deployment of a sensing system for the long-term performance monitoring of all bridge spans under service loads. To better understand the characteristics and behavior of the bridge under environmental and traffic effects, strain gauges were installed on GFRP bars to understand the load distribution and dynamic impact factor in this study. For long-term monitoring, a wireless SHM system with the SmartBrick network was developed. The measured data may offer critical information for the evaluation of advanced materials and innovative designs of the Pat Daly Road Bridge. However, the wireless transmission signal was extremely low at the bridge site so that the wireless network was not tested at the bridge site. Even cellular phones did not receive any signal.

4.2 General monitoring guidelines

The scope of work for the bridge monitoring is to assess the impact of vehicle loads, thermal movement, and their induced strains in various bridge components throughout their

service life. In what follows, the sensor, data acquisition, and network system are selected according to the general guidelines in three main parts: a) sensors for detection of a physical quantity, b) system control unit for overall management of monitoring tasks, data organization and storage, and c) communication interface for data transmission and command exchange. The proposed wireless SmartBrick network realizes the last two parts with an on-board base station and a two-way long-range communication system over the cellular phone infrastructure.

4.2.1 Sensors

Sensors in this chapter are referred to those electronic devices that are embedded inside concrete members during their fabrication at the precast yard. The sensors embedded in concrete sometimes become malfunctional during concrete casting, transportation and erection in the field. Even so, embedded sensors have been significantly applied for strain, temperature, moisture and pressure measurements. Commonly accepted sensors include electrical strain gauges, fiber optic sensors, wireless sensors, and others. Among them, the electrical strain gauges have been long accepted for over 50 years in structural applications due to their technical maturity and reliability. Handled with care, strain gauges have been successfully used to offer critical information in key structural elements and components in a cost-effective manner (Choi, 2008). In this study, strain gauges were attached on the surface of GFRP bars and embedded in concrete members at a prefabrication yard; they were used as an important element in the monitoring system developed for the Washington County Bridge.

Temperature gradient between the top and bottom bridge components may change the bridge behavior and significantly impact the performance of the monitoring system. To minimize the temperature effect on strain readings from GFRP rebar, a half-bridge configuration was used for data acquisition in a Wheatstone bridge, which proved to be a critical consideration in the

monitoring system design for bridges. At each location, two strain gauges were mounted on the top and bottom surfaces of a GFRP bar, respectively; they can compensate for the thermal expansion of materials in a half bridge designed to acquire strain data.

4.2.2 Data collection and monitoring system

As previously reviewed in Chapter 2, traditionally wired communication systems have significant drawbacks such as high cost, difficulty in installation, potential interference with construction, and high power consumption. As a result, they are often deployed at limited areas that are convenient for power supply and interconnection of various components of the monitoring system.

Therefore, wireless monitoring systems have recently received significant attentions in the research community. In this study, a wireless and autonomous system has been developed for the monitoring of the Pat Daly Road Bridge in Washington County, MO. The system is referred to as the SmartBrick network that represents a general base station with onboard and external sensors for environmental and structural measurements. Such a base station is achieved through an embedded quad-band GSM/GPRS modem, enabling a long-range two-way communication over the cellular phone infrastructure. The base station can be characterized with ultra-low power consumption and redundant power supply features, which allows it to operate wirelessly for remote monitoring, maintenance, and calibration over a long time. Following is a presentation of the hardware and software (firmware) developments made to the previous SmartBrick prototype (Harms et al., 2010). All new functions implemented in the new SmartBrick have been tested in laboratory conditions.

The major hardware update involved the design and development of a new SmartBrick motherboard with integrated long-range (GSM/GPRS) and short-range (ZigBee) communication

capabilities. The motherboard is mostly used as a key component of the base station but can also be used as a sensor node when the GSM modem is not soldered to the printed circuit board and the required software is configured accordingly. The other major hard update was the implementation of a sensor daughterboard. The daughterboard can interface with up to 40 external sensors by means of a three-pin screw terminal. The entire operation of the sensor daughterboard is controlled by the SmartBrick motherboard. Figure 4.1 shows the architectures of the motherboard and the daughterboard, respectively, and the data flow between them.

The SmartBrick motherboard features an improved Microchip DSPIC33F-series microcontroller and a MRF24J40 ZigBee transceiver. The merits of these two improvements have been discussed elsewhere (Harms et al., 2010, Gunasekaran et al., 2012). Additional sensors have been embedded in the motherboard, including a three-axis inclinometer and temperature and vibration sensors. The board also features a serial-to-parallel port expander to overcome pin constraints and allow for interface with an increased number of external sensors. Although the DSPIC33F microchip has a 100-pin chip, additional interfacing capabilities are often required to monitor a large-scale transportation structure for sensors, input, display and other devices. As such, the daughterboard is introduced and connected to the SmartBrick motherboard as illustrated in Figure 4.1. The two boards are connected with three buses for power, data, and control handling. The control line governs the supply of power to the daughterboard and the switching of the power supply and measurement channels (sensors) for power conservation. Separate regulators are used to control power to the analog and digital parts of the circuit, respectively. The strain gauges used in this study are 120 Ohms and consume approximately 36 mA when excited by a 3.3 V power supply.

Once the daughterboard is switched on, the demultiplexer decodes the input control signal and excites the strain gauges in sequence. This setup helps maintain the average power consumption at a fixed level and conserve power when the strain gauges are not in use. Switching on all 32 strain gauges at once, as indicated in Figure 4.2, and taking the readings concurrently would consume 1.152 A at 3.3 V. A tradeoff is made between the sampling rate achieved and power consumption. The strain gauges are used in half-bridge configuration, and after they are excited, the output voltage is amplified by means of an analog multiplexer and sent to the A2D port of the microcontroller. Figure 4.3 shows the actual fabricated daughterboard.

Perhaps the most important feature of the SmartBrick base station is the embedded quad-band GSM/GPRS modem. For more efficient monitoring of larger structures, the SmartBrick base station has been supplemented with sensor nodes that are similar to the base station in sensing capabilities but without the modem, which is the most expensive hardware component. Short-range, low-power wireless Zigbee transceivers link these nodes to the base station and to each other. Extensive I/O and several expansion headers are provided for the base station and sensor nodes, enabling the interface with additional 35 digital or analog sensors and facilitating control of external devices such as actuators. For the bridge with rapid construction of precast components, strain gauges were spatially distributed throughout the structure, particularly providing critical information on the behavior of individual structural components.

4.3 Sensor arrays

The location of two SmartBrick networks and the distribution of 64 strain gauges in the box girders are illustrated in Figure 4.4. The two smart bricks were mounted on the two intermediate wall piers for access and communication convenience in collecting the strain data from all three spans of the bridge. Following is a brief description of the strain gauges layout in

steel-/concrete-girder and box-girder spans. The step-by-step installation procedure for preparation, deployment, and protection of strain gauges for long-term monitoring of the bridge are referred to Appendix A.

4.3.1 Sensor layout and placement

A total of 192 strain gauges were mounted on the GFRP bars and embedded either in the GFRP reinforced box girders or the GFRP reinforced concrete deck slabs at the prefabrication yard of precast members. For each of the steel-girder, concrete-girder, and box-girder spans, 32 pairs of strain gauges (64 for each span) were deployed both longitudinally and transversely. As indicated in Figure 4.5 for the longitudinal/traffic direction, the number of strain gauges deployed at the bottom flange of each box girder is 3 at mid-span, 2 at the quarter span, and 2 at the three-quarter span, respectively. As indicated in Figure 4.6 for the transverse direction, each box girder was instrumented with 2 strain gauges at the bottom side of GFRP stirrups in mid-span only. The above instrumentation plan was developed based on the following considerations: a) longitudinal and transverse distributions of traffic loads, b) structural integrity at joints between any two adjacent box girders, and c) potential end support effect on the theoretically simply-supported girders. Note that the negative strain at the top GFRP bars was not monitored due to limited channels available and, more importantly, due to expected low strains under operational loads so that the neutral axis likely passes through the centroid of each cross section of concrete. Similarly, the steel-girder and concrete-girder spans were each instrumented with 64 strain gauges, 32 in longitudinal direction and 32 in transverse direction. In general, strain gauges were deployed on the top GFRP bars above the supporting girders and on the bottom GFRP bars in between the girders to measure the tensile strains expected in the bridge deck slabs. The number and location of strain gauges used in each span are summarized in Table 4.1.

4.3.2 Long-term strain gauges installations

Strain gauges are intended to be mounted on the GFRP bars in the bridge, as indicated in Figures 4.9a through 4.9c. Each detail for strain gauges installation, from soldering, adhesive or protection to transportation, may impact the sensing. Having good bond between the strain gauge sensor and the GFRP bar, present in Figure 4.8a, is essential for efficient strain sensing of the bridge. Unlike the common adhesives used for strain gauges in short-term applications, selection adhesive is important. It is because a good interfacial adhesive can minimize the possibility of slip between the sensor and the bar, which helps to provide effective force transfer from the GFRP bar to the embedded sensor as well. Many adhesives typically formulated for improving bonding are available commercially. Different commercial adhesives were selected for evaluation and the quality of bonds for sensor surface and types of adhesive for long-term performance were assessed based on manuals provided by manufactures. One long-term adhesive with six-hour curing was selected. Such adhesive also required constant pressure on the sensor during the curing period.

On the other hand, extra efforts to a good protection of the embedded strain gauge sensors away from any potential damage or impact during precast, construction or transportation period in the host concrete materials is another critical key for efficient strain sensing. Multiple rubber-like protection materials used herein for covering the sensors, illustrated in Figure 4.9b, can minimize the possibility of damage. Sensor installation and procedures was presented in Appendix A.

The new prototype of Smartbricks were carried out on an experimental the bridge. Figure 4.4 depicted the layout of the bridge and instrumentation, respectively. The strain gauges were interfaced to the daughterboard and the variation in the strain was studied.

4.4 Summary

SHM network systems have been designed to collect information on performance of the bridge, which also help to develop detailed knowledge of how the GFRP bar bridge behaves, particularly with respect to overweight vehicles and other environmental effects. The goal aims to develop a network of remote wireless monitoring systems to provide first-hand information of the new bridge, therefore providing a solid foundation for the enhancement of these systems.

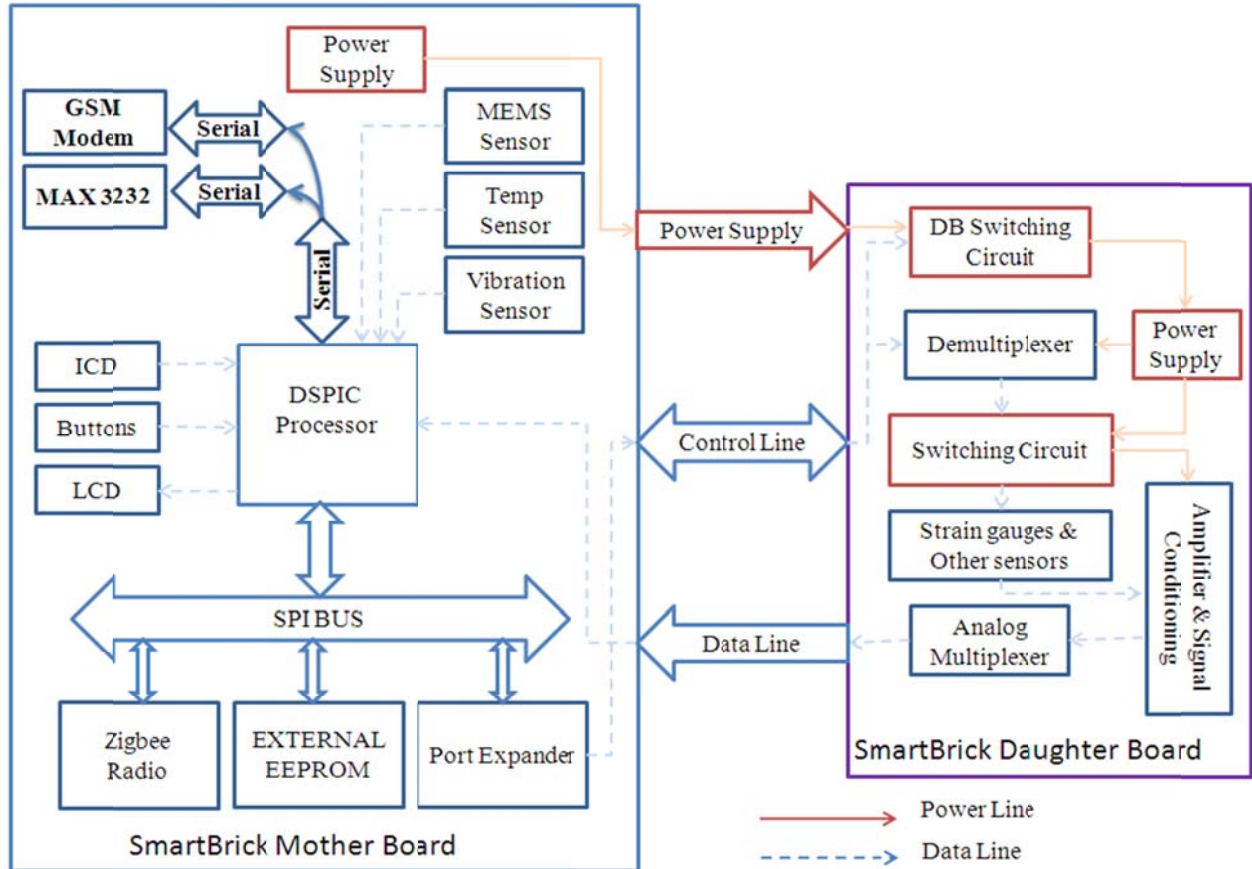


Figure 4.1: Architectures of SmartBrick motherboard (left) and daughterboard (right)

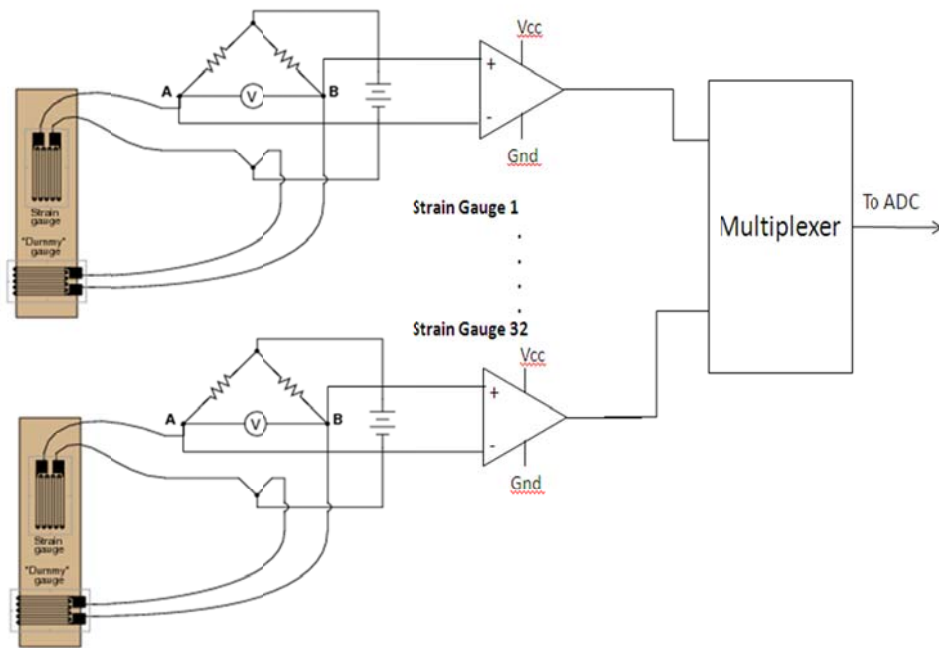


Figure 4.2: Half-bridge configuration and multiplexer in SmartBrick Daughterboard

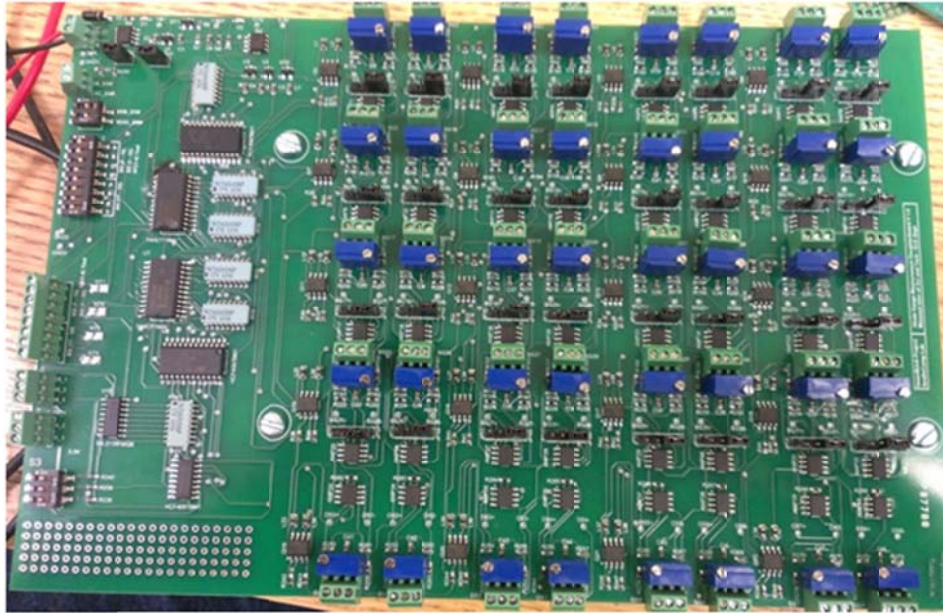


Figure 4.3: Prototype daughterboard in SmartBrick for strain gauge measurement

Table 4.1: Number of strain gauges used

	Direction	Box girders	Concrete girder deck slabs	Steel girder deck slabs
Bottom Rebar	longitudinal	56	14	14
	transverse	8	14	14
Top Rebar	longitudinal	0	18	18
	transverse	0	18	18
Total strain gauges		64	64	64

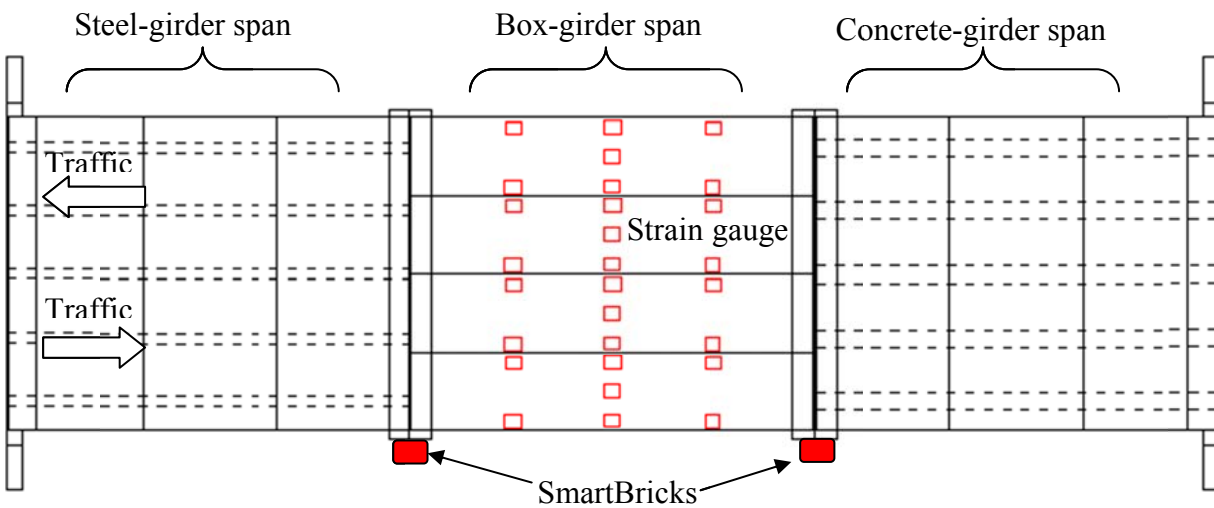
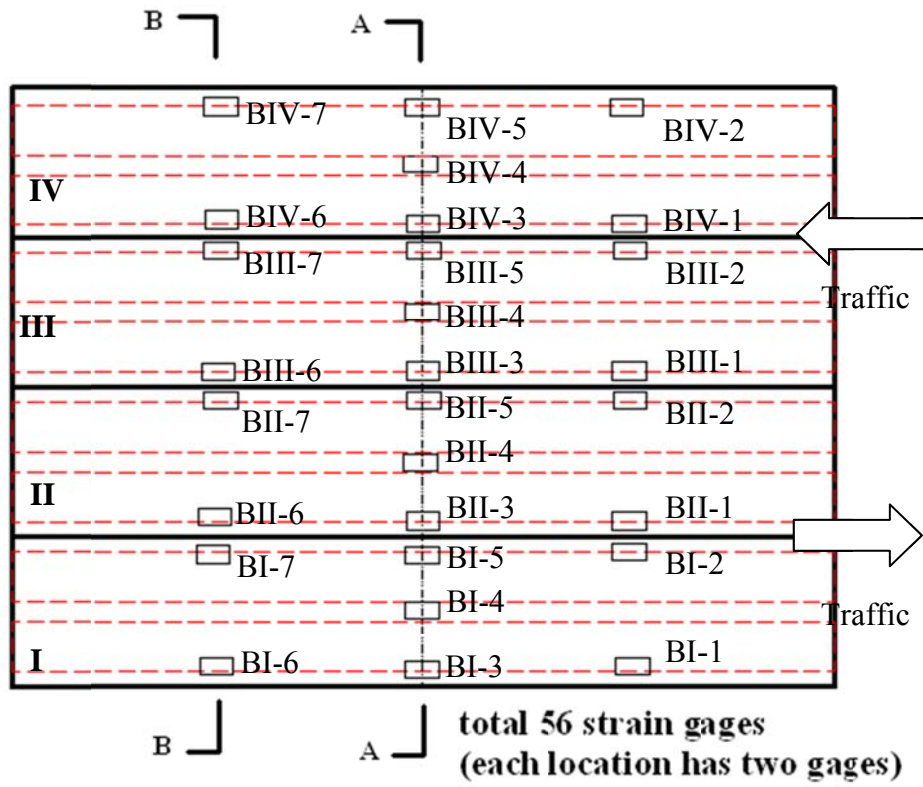
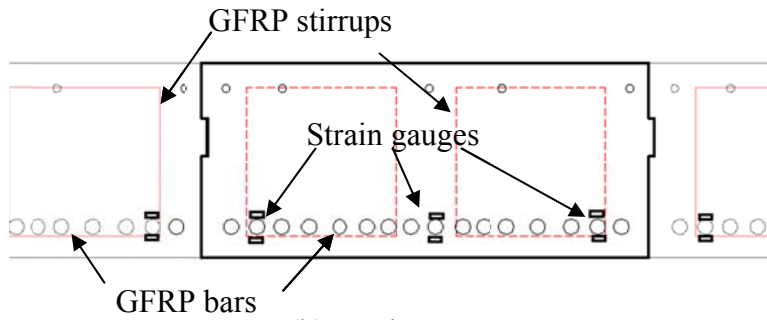


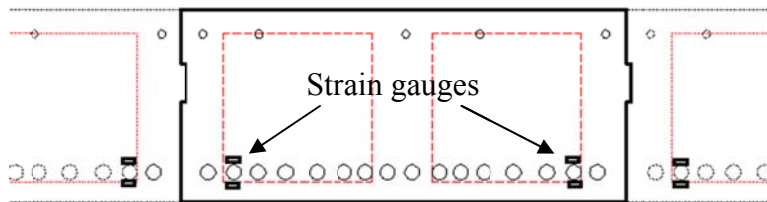
Figure 4.4: Instrumentation layout in GFRP reinforced box-girder span of the Washington County Bridge



(a) Plan view (56 strain gauges total)

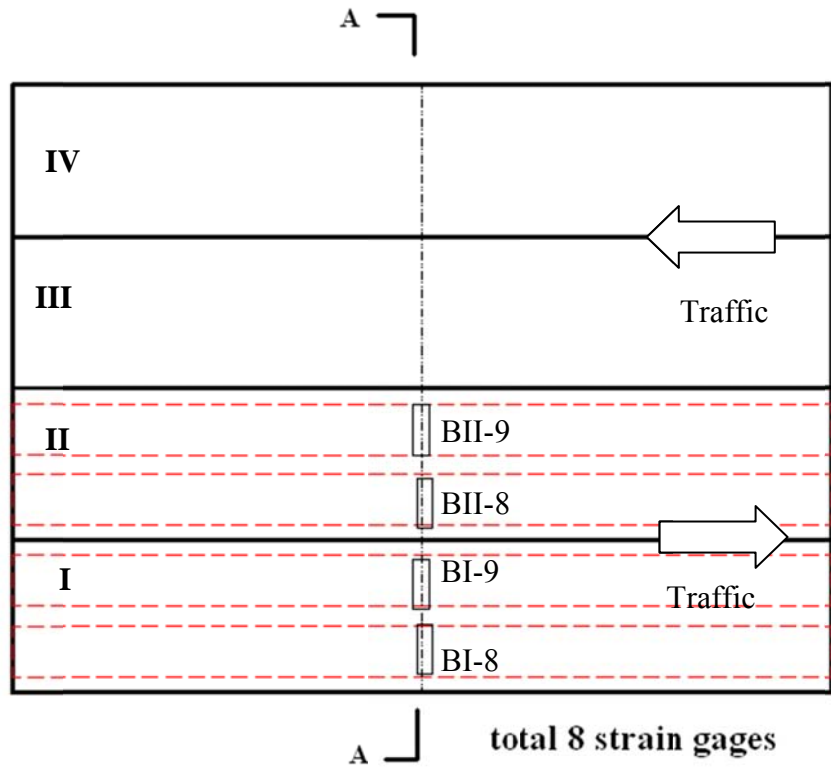


(b) Section A-A

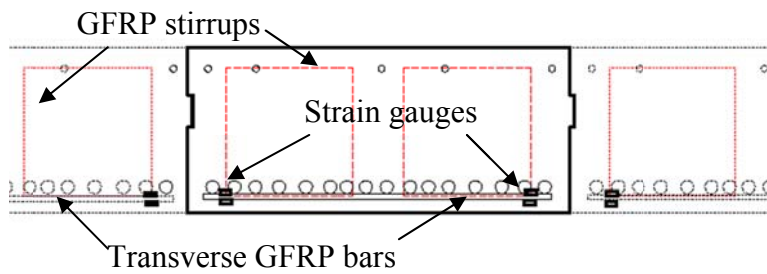


(c) Section B-B

Figure 4.5: Longitudinal strain gauges layout in the GFRP reinforced box-girder span

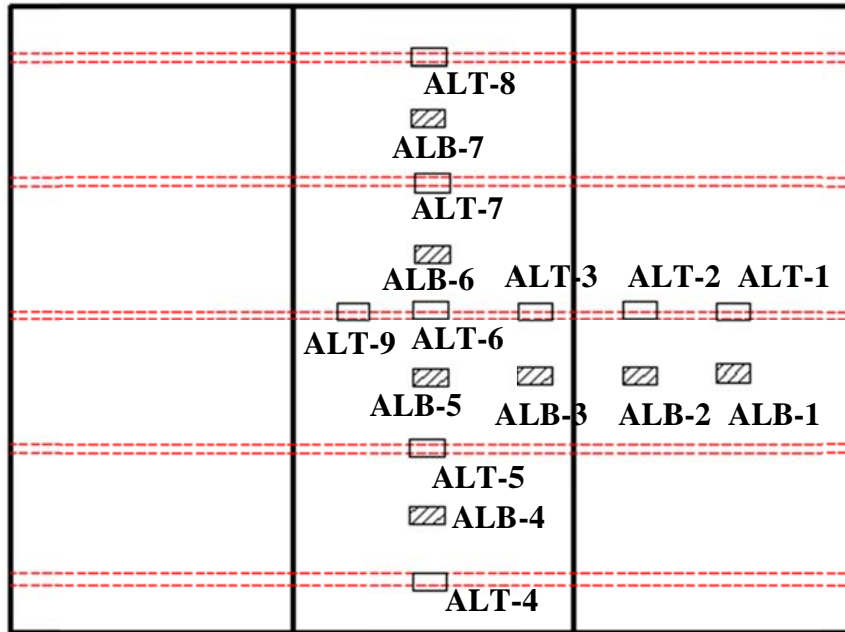


(a) Plan view (8 strain gauges total)



(b) Section A-A

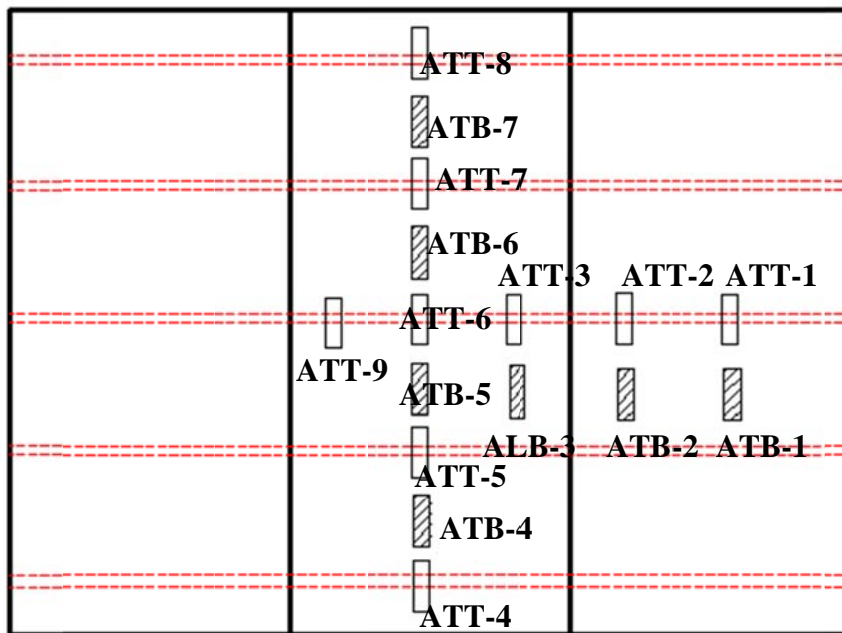
Figure 4.6: Transverse strain gauges layout in the GFRP reinforced box-girder span



▨ Strain gauges on bottom layer

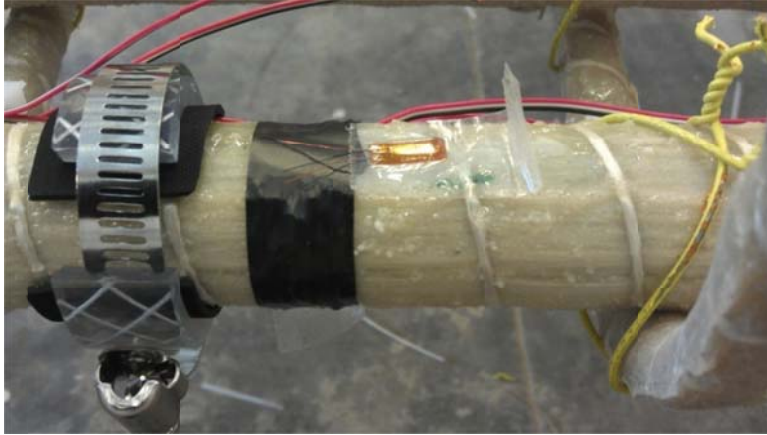
□ Strain gauges on top layer

(a) Longitudinal strain gauges in deck slabs (32 total)



(b) Transverse strain gauges in deck slabs (32 total)

Figure 4.7: Strain gauges layout in the GFRP reinforced concrete deck of the concrete- or steel-girder span



(a) Installation of two half-bridge strain gauges at each location



(b) Long-term protection of strain gauges

Figure 4.8: Strain gauges installation on GFRP bars



(a) Box girder cage with installed strain gauges



(b) Loading and unloading of GFRP-bar cages

Figure 4.9: Preparation of GFRP-bar cages with installed sensors for the precast plant

Chapter 5. Precast of GFRP-bar Reinforced Concrete Bridge Elements and Accelerated Bridge Construction

5.1 Introduction

Accelerated construction, rehabilitation, and repair of bridges have received increasing attention in modern society. It is mainly because rapid construction and rehabilitation can improve work zone safety, minimize traffic disruption, and improve the quality of bridges. Central to the accelerated bridge construction is the use of precast bridge elements (concrete members or structures) that are fabricated at the precast plant and then transported to the bridge site for construction. Due to easy-to-control casting conditions at precast plants, precast bridge elements often have better quality than cast-in-place components. As a result, precast bridges may be more durable.

In this project, all superstructure bridge components such as bridge deck slabs and concrete box girders were fabricated in a local precast plant located in Springfield, MO. Specifically, six 9 ft by 21 ft GFRP-bar reinforced concrete slabs and four 27 ft by 5.25 ft GFRP-bar reinforced concrete box girders were fabricated at the prefabrication yard. In addition, one additional concrete slab and one additional box girder were fabricated for laboratory tests to validate the design of the bridge elements. The bridge deck slabs were supported on steel girders or concrete girders that rest on two end supports. The concrete box girders were simply supported at both ends. Therefore, the CFRP post-tension tendons were used only to close the construction joint between two adjacent precast elements.

5.2 Precast of bridge deck slabs and box girders

5.2.1 Concrete

The mixture design of commercial self-consolidated concrete was used in this project. The water-cement ratio (w/c) was kept at 0.36 (with superplasticizer), and the maximum size of coarse aggregates was 17 mm. Compressive tests of cured concrete cylinders were conducted using a universal compression testing system following the ASTM C39. The hardened concrete had an average compressive strength of 7.8 ksi (53.8 MPa) at age of 28 days.

5.2.2 GFRP bar

Much work (Nanni, 2000; Nanni, and Lopez, 2004; Nystrom et al., 2002; El-Sayed et al., 2005; Deitz et al., 1999; Breña et al., 2001; Winkelman, 2002;) has already been done to characterize the mechanical properties of FRP composites. In addition, FRP bars in concrete structures serve as corrosion resistant reinforcement, which results in the more durable concrete structures. Each FRP bar as shown in Figure 5.1a represents a composite of millions of thin and high strength fibers covered by polymeric resins (Nanni and Lopez, 2004), as schematically shown in Figure 5.1b. The fibers in an FRP composite are main load-carrying elements while the remaining resins hold the fibers together and also protect fibers against potential environmental and mechanical damage (Nanni, 1999). The physical characteristic of the surface treatment of GFRP bars was considered as an important property for mechanical bond with concrete matrix. Among three types of commercially available surface patterns of GFRP bars, the wrapped and sand-coated surface treatment was selected herein. In terms of flexural capacity, such bars have relatively higher ductility than carbon fibers or other types of commercially available fibers, even though carbon fibers have the highest strength and stiffness. Figure 5.1c shows the SEM

micrograph of glass fibers embedded in resins (Kornmann et al., 2005). Typically assembled GFRP-bar cages for box girders were shown in Figure 5.2.

Concrete slabs as detailed in Figure 4.3 were reinforced with No. 5 (#16) and No. 6 (#19) GFRP bars while concrete box girders were reinforced with No. 10 (#32) longitudinal reinforcement and No. 5 (#16) stirrups and transverse reinforcement. In this project, Aslan 100 GFRP bars manufactured by Hughes Brothers were used in precast elements. Their material properties are listed in Table 5.1, including the Young's Modulus E for three sizes of GFRP bars, the low ultimate tensile strength, f_{ut} , and the low ultimate strain ε_{ut} . No. 5 (#16) GFRP bars with a specified ultimate tensile strength of 95 ksi (655 MPa) were used as longitudinal and transverse reinforcement on the top layer of concrete slabs and stirrups in concrete box girders. No. 6 (#19) GFRP bars with 90-ksi (621 MPa) ultimate tensile strength were used as reinforcement at the bottom layer of concrete slabs while No. 10 (#32) bars with 70 ksi (483 MPa) tensile strength were for main reinforcement in concrete box girders. The design properties of GFRP bar materials were derived from those values in accordance with ACI 440 Guidelines (2006) by:

$$f_{ut}^e = \phi f_{ut} \quad (5.1a)$$

$$\varepsilon_{ut}^e = \phi \varepsilon_{ut} \quad (5.1b)$$

where f_{ut}^e and ε_{ut}^e are the design ultimate tensile strength and ultimate strain, respectively, and ϕ is the reduction factor (=0.7 as recommended by the ACI 440 1R-06 Guidelines).

5.2.3 Precast bridge elements

Concrete slabs and box girders were fabricated in the precast plant in Springfield, MO. The casting bed (formworks) for each concrete slab was first laid down as shown in Figure 5.3. The GFRP bar cage for the slab was then assembled inside the formworks according to the steps

illustrated in Figures 5.4a through 5.4c. The concrete slabs rested on five steel or concrete girders in the first or third span, as illustrated in Fig. 4.1, were designed as a non-composite slab-girder system. The only connection between the slab and girder was achieved by several grout pockets that are filled with non-shrink grouts at the bridge site. Ten rectangular foams, as illustrated in Figure 5.4a, were placed at specified locations in each GFRP bar cage to provide various grout pockets in the finished concrete slab. PVC pipes were embedded along the longitudinal direction of each slab (parallel to traffic flow in its final position) to allow the longitudinal post-tensioning tendons through such prescribed ducts. As shown in Figures 5.5a and 5.5b, curbs at both ends of the slab were cast together with the bridge deck slab with L-shaped GFRP reinforcing bars. Note that the GFRP bar cage was placed upside down as illustrated in Figure 5.5b to make a smooth finished slab surface, which will be the bottom face of bridge decks in field construction. During the bar assemblages and concrete pouring, the long-term strain gauges as shown in Figure 5.6 were carefully treated. The reinforcement bars were carefully placed to ensure that the design slab thickness and concrete cover be achieved by inserting bar supports at the top and bottom GFRP bars. For each concrete box girder, a GFRP bar cage was assembled with two strips of foams embedded in the center of the cage as shown in Figure 5.7.

Precast of bridge components was performed according to the Manual for Precast, Prestressed Concrete Products in the Missouri Department of Transportation Standard Specifications for Road and Bridge Construction (1999). The prepared formworks were first sprayed with a release agent prior to concrete pouring to facilitate de-molding of the cast elements. Bridge elements were then cast with commercial self-consolidated concrete and de-molded after one-day setting. The precast elements were finally cured under a plastic cover for 7

days before they were moved outside the plant in air dry condition, as indicated in Fig. 5.8. All precast bridge elements were placed in the fabrication yard for over 28 days.

5.3 Construction of bridges

5.3.1 Construction management and procedures

Construction management and procedures were based on the specified contract drawings and specifications. Construction controlling and layouts consisted of the construction procedure for each type of bridge superstructure/substructure component and the establishment of construction control points that were used to maintain the horizontal and vertical alignment of scheduled works. To ensure that the completed bridge was in correct alignment with the approach roadway, the initial survey and layout established one or more centerlines to guide the construction process of the three-span bridge.

Following the required survey at various control points, the substructure components were cast in place according to the bridge design specifications, including two abutments, and two intermediate wall piers that were cast-in-place with footing socketed into rock by at least 6” (152 mm). I-shaped steel girders for the first span (Figure 3.1b) and rectangular concrete girders for the third span (Figure 3.1d) were then seated on top of the piers and the abutments along the survey line. To ensure accurate placements, all points were checked for horizontal and vertical alignment through the station of bench marks at both abutments.

When transported to the bridge site as illustrated in Figure 5.9, the precast concrete slabs were erected as part of the bridge superstructure according to an erection plan as schematically illustrated in Figure 5.10 after the cast-in-place substructures have been completed and concrete/steel girders have been placed as shown in Figures 5.10a and 5.10b in the first (east)

and third (west) spans shown in Figure 5.10c. Similarly, the precast concrete box girders were erected for the middle span shown in Figure 5.10d. Once in place, various precast slabs in the first and third spans were connected with post-tensioned CFRP rods, and various precast box girders were connected with post-tensioned CFRP rods.

The bridge decks were covered with an approximately 3” (76 mm) asphalt overlay. The approach roadway and bridge wearing surface treatments were built in accordance with the contract drawings and specifications. The bridge girders and decks were placed in alignment with the existing roadway, and the edge and center line of the roadway. Their placement was always checked after each step of construction. Due to the solid rock ground, a truck-mounted crane was used during the entire erection process of all precast bridge elements.

5.3.2 Bridge substructure components and concrete/steel girders

Abutments, two intermediate wall piers, and footings were cast in place with cladding steel reinforcement as shown in Figure 5.10a. Alignment of various bridge substructure components was crucial to ensure the accurate placement of a whole bridge system. Cast-in-place substructures were mainly checked during the construction period of:

(a) Foundation Footings:

- Lateral alignment
- Level or vertical alignment at the top of footings of abutments and intermediate piers.
- Cross-sectional dimensions

(b) Abutments:

- Lateral alignment
- Level or vertical alignment

- Cross-sectional dimensions

(c) Piers:

- Lateral alignment
- Level or vertical alignment
- Cross-sectional dimensions
- Girder seat elevations (elastomeric pad and no-shrink grout)

Concrete girders and steel girders for the first (east) and third (west) spans were then placed on the wall piers and abutments by the truck-mounted crane as schematically shown in Figure 5.10b. Elastomeric pads were used between girders and their supports.

5.3.3 Bridge deck slabs

Six bridge deck slabs and four box girders were delivered to bridge site by trailers as show in Figure 5.9. The slabs were stored at east side of the creek bank and placed on the bridge using a truck-mounted crane. The truck-mounted crane was parked at south side of the bridge to perform the placement of bridge components as indicated in Figure 5.11.

Slabs were first placed in the first (east) span of the bridge from the east end to the middle of the river. Figures 5.11a through 5.11c showed the erection operation and the sequence of seating of the deck slabs. The first deck slab was seated at the east side near the approach roadway (Figure 5.11b). To avoid any difficulty associated with duct misalignment between three pieces of deck slabs, ten post-tensioning CFRP tendons were inserted into their prescribed ducts in longitudinal direction (traffic flow) following the placement of each slab. Two high-strength threaded rods were connected with couplers to the two ends of each CFRP tendon to allow site post-tensioning. The second and third deck slabs were then uplifted and seated adjacent to the first one. To enable the placement of middle-span box girders from both east and

west ends, the deck slabs in the third (west) span were then placed as illustrated in Figures 5.13a through 5.13c. Figure 5.12 showed an overview of the bridge after the complete placement of the three slabs at east end. The slight gap between slabs was sealed after post-tensioning of the deck slabs was completed. In addition to following the survey line and the benchmarks on abutment at east side, compatible adjustments were made within tolerance to allow the predetermined deck pocket slots matching with shear studs on top of the steel/concrete girders during the seating process.

5.3.4 Bridge box girders

After the deck slabs for the first and third spans had been seated on abutments and intermediate piers, the remaining four box girders were ready to be placed as shown in Figure 5.14. The box girders were directly lifted from the truck and placed on the two intermediate piers using the truck-mounted crane. To avoid potential hazards associated with the twisting of a box girder during the uplifting, two cables were tied at two ends from opposite directions to stabilize its movement.

The box girders were placed one-by-one from upstream on the north side to downstream on the south side. Figures 5.14a through 5.14c showed a typical seating process of one box girder. Similar to the placement of deck slabs, post-tensioning CFRP tendons as illustrated in Figure 5.15 were fed through the pre-embedded ducts in transverse direction (perpendicular to traffic flow) after each box girder had been put in place on the two intermediate piers. During the box girder seating process, lateral alignment was checked against the first and third span curbs. To alleviate potential impact effects after the bridge opened to traffic, a 0.5” (13 mm) thick rubber was placed between each girder and its supporting wall pier or abutment as typically

indicated in Figure 5.16. Figure 5.17 plotted the new erected bridge after all bridge elements were completely put in place.

5.3.5 Internal unbounded post-tension of the bridge system

Post-tensioning of bridge elements (e.g., deck slabs and concrete girders) is generally a cost-effective way of improving mechanical properties/durability of the bridge (Poston et al., 1987; Wipf et al., 2003). In this project, since precast slabs are stably supported by steel/concrete girders and precast girders are stably supported by intermediate wall piers, post-tensioning is merely to close the construction joints for improved durability.

In simple terms, post-tensioning is to apply a compressive force on a concrete structure by tensioning a steel/CFRP tendon through pre-embedded ducts in the concrete so that the concrete structure is subjected to compression at zero external loads. The process of post-tensioning started with installation of a hydraulic jack at one end of the tendon while the other end of the tendon was beard with a square plate against the concrete structure and tensioned after precast deck slabs as schematically shown in Figures 5.18a and 5.18b have been placed on steel/concrete girders and each tendon passed through three slabs for each bridge span. After the tendon was mechanically locked, the tensile force in the hydraulic jack was released, applying a compression force to the concrete transferred from the jack, as shown in Figure 5.18b. Such a compression force may not only offset some tensile forces and reduce the likelihood of tensile cracks developed, but also make three slabs work together. Similar to the deck slabs, four box girders were tied together transversely by two post-tensioning CFRP rods, as shown in Figures 5.19a and 5.19b.

Specifically, after three deck slabs were put in place for each span, ten post-tensioning CFRP tendons were applied through the pre-embedded ducts in concrete slabs. Each CFRP

tendon was first connected by a coupler to two high-strength threaded rods at both ends. One threaded rod was then connected to a hydraulic jack by a coupler as shown in Figures 5.20a through 5.20c. The hydraulic jack was mounted on a load frame supported on a Forklift as shown in Figure 5.20a. A Daytronic Conditioner (Model 3270) with a 200 kip (890 kN) Cooper load cell and an LCD display was mounted on the hydraulic jack and used to monitor the loading applied to the CFRP tendon as indicated in Figure 5.20b. A tendon force of 20 kips (89 kN) was then applied to each of the ten tendons to snug up the three slabs by using a hand pump as shown in Figure 5.20c. To symmetrically apply post-tensioning forces for each span, post-tensioning forces were first applied around the centerline of cross section and then towards both sides of the cross section. This process was repeated after the entire slab cross section or box girder was compressed. Note that for the middle span, only two CFRP tendons on one side of the box girders were successfully implemented and others were fractured due to misalignment of the pre-embedded ducts in several box girders. After the post-tensioning operation was complete, all the slots at the ends of tendons were sealed by non-shrink grouts for protection of the tensioning tendons.

Polyurethane elastomeric joint sealants were used to seal joints among precast slabs and among box girders. Once the erection of the bridge superstructure was completed, two approaches were casted at both east and west sides. Finally, a 3-in. hot-rolled asphalt wearing surface was used to cover the entire bridge deck. Figures 5.21a through 5.21c displayed the overview of the bridge and views from east and west approaches.

5.4 Summary

In this section, the entire process of precast, transportation and construction of the new bridge system were addressed. The complete erection of precast bridge elements demonstrated

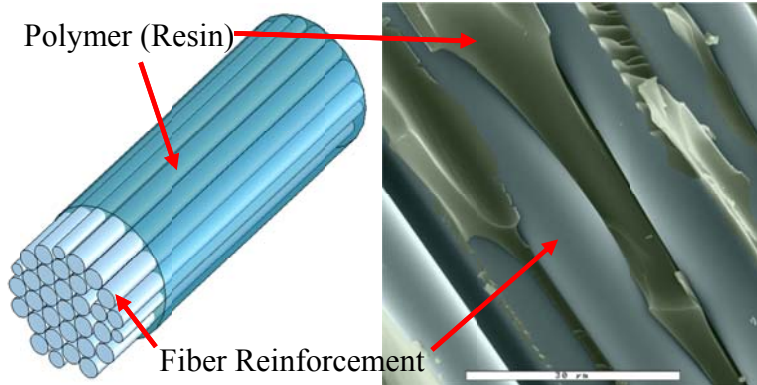
that the proposed concept of assembling bridge elements (deck slabs and box girders) with GFRP bar reinforcement is practically feasible, minimizing the actual construction time at bridge site with less equipment and labors.

Table 5.1: Material properties of Aslan 100 GFRP bars

I.D.	Young's modulus, E_G ($\times 10^6$ psi)	Ultimate tensile strength, f_{ut} (psi)	Ultimate strain, ϵ_{ut} (in./in.)
# 5	5.92	95,000	0.01605
# 6	5.92	90,000	0.01520
# 10	5.92	70,000	0.01182



(a) Wrapped and sand-coated Aslan 100 GFRP-bars



(b) Representation of FRP bar

(c) SEM image of GFRP composites (Kornmann et al., 2005)

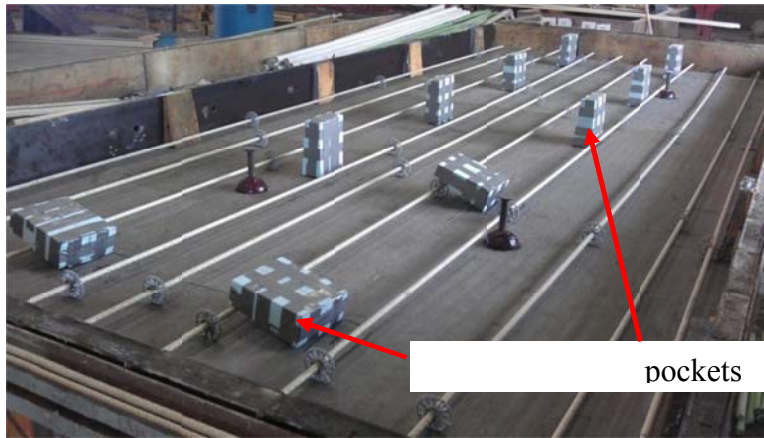
Figure 5.1: Wrapped and sand-coated GFRP bar



Figure 5.2: GFRP-bar cages



Figure 5.3: Steel formwork for concrete deck slab at the precast plant



(a) Transverse bars and embedded foams



(b) Top layer of reinforcement (casting upside down of the precast slab)



(c) All reinforcement, embedded foams and embedded PVC pipes for post-tensioning

Figure 5.4: Form work for casting concrete deck slab in prefab plant



Figure 5.5: Integral construction of bridge curb with deck slab (upside down casting)



Figure 5.6: Strain sensors in concrete deck slab



Figure 5.7: Formwork for concrete box girder



(a) Box girders

(b) Concrete deck slabs

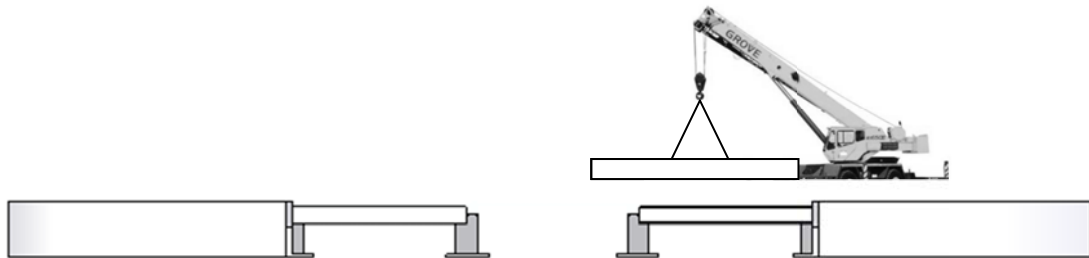
Figure 5.8: Finished precast elements



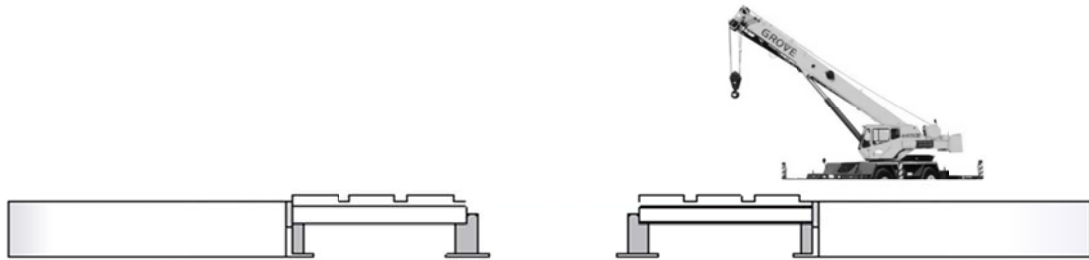
Figure 5.9: Transportation of precast bridge elements



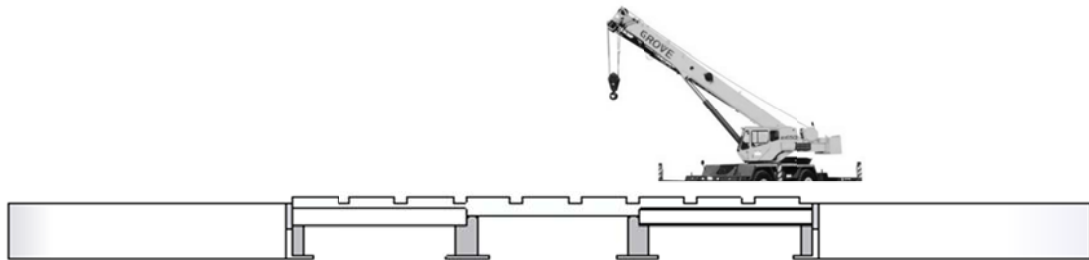
(a) Completed cast-in-place substructures with cladding steel reinforcement



(b) Placement of concrete/steel girders in the first (east) and third (west) spans



(c) Placement of deck slabs in the first (east) and third (west) spans



(d) Placement of box girders in the middle span

Figure 5.10: Erection steps of the bridge



(a) Uplifting one deck slab by a crane



(b) Placing one deck slab on top of steel girders



(c) Placing second concrete deck slab

Figure 5.11: Placement of GFRP-bar reinforced concrete deck slabs



Figure 5.12: Completion of all concrete deck slabs on top of steel- and concrete- girders



(a) Post-tensioning tendons through deck slabs over steel girders



(b) Feeding post-tensioning tendons through deck slabs over concrete girders

Figure 5.13: Installation of CFRP tendons for post-tensioning



(a) Lifting one box girder



(b) Placing one box girder in the middle span



(c) Finishing of one box girder placement

Figure 5.14: Placement of GFRP-bar reinforced concrete box girders



Figure 5.15: Pulling through CFRP tendons for post-tensioning



Figure 5.16: Bridge girders seated on a rubber pad



Figure 5.17: The newly erected three-span bridge

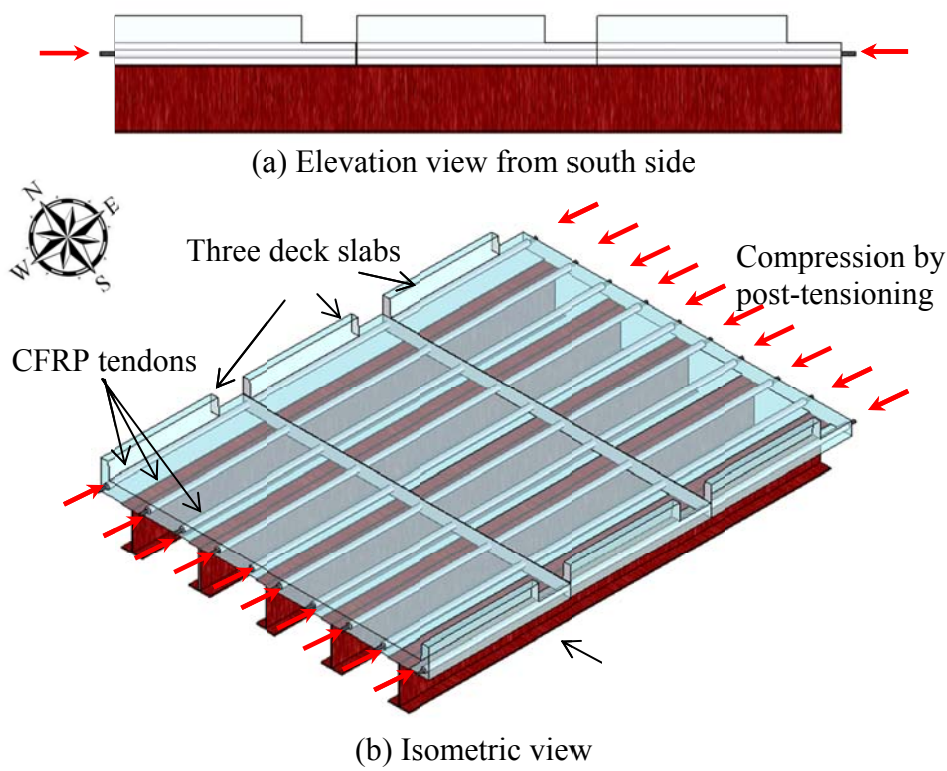


Figure 5.18: Schematics of a post-tensioned, steel-girder deck (3 slabs) with ten CFRP tendons

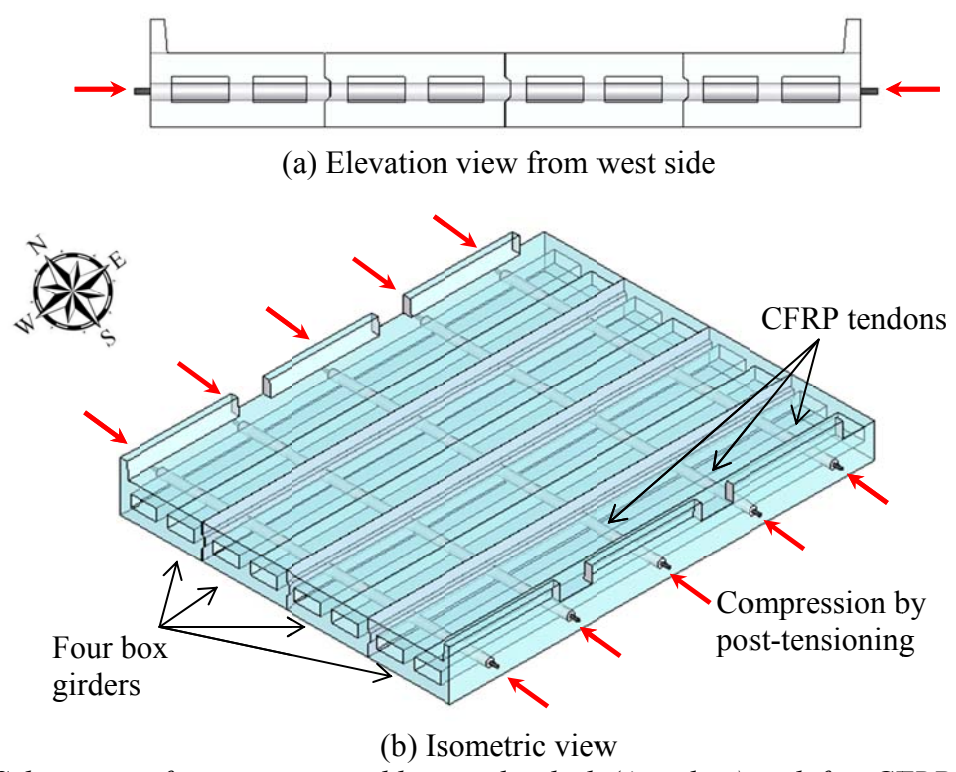
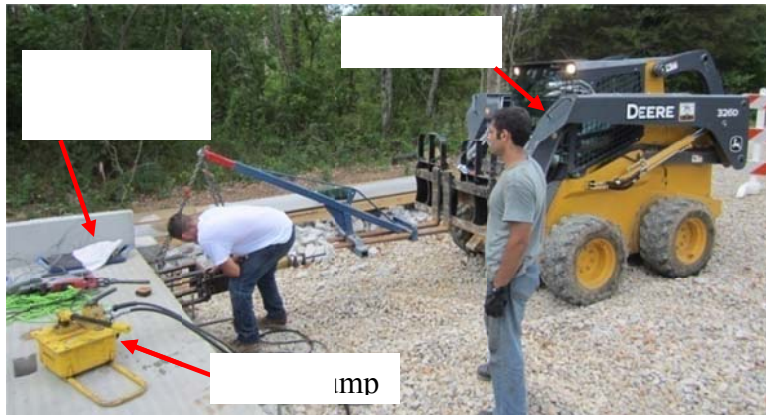
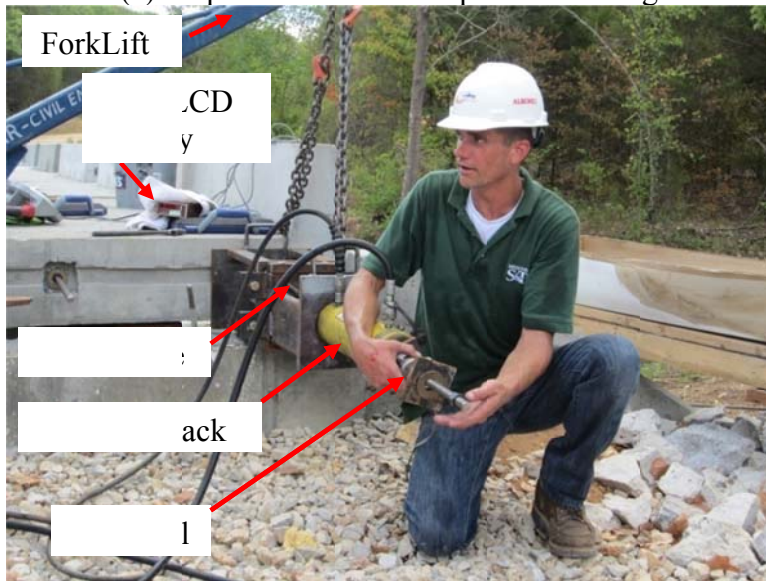


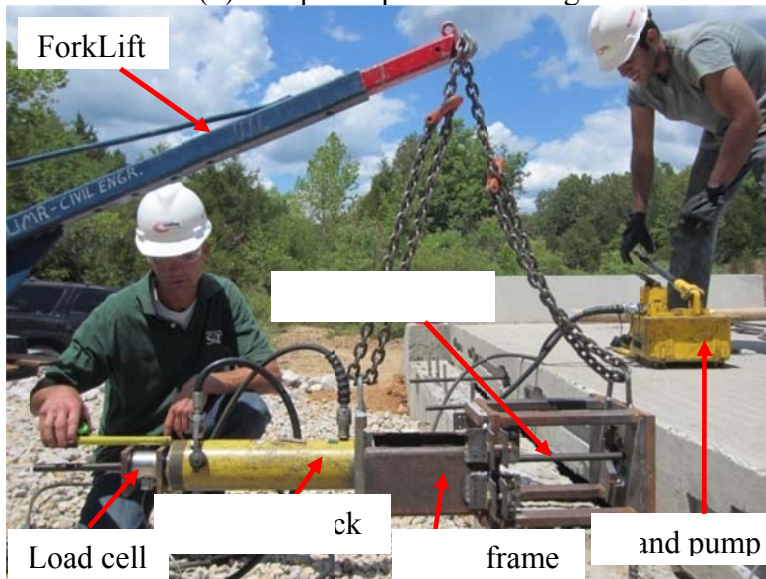
Figure 5.19: Schematics of a post-tensioned box-girder deck (4 girders) with five CFRP tendons (3 fractured during installation)



(a) Preparation for on-site post-tensioning



(b) Setups for post-tensioning



(c) Inspection during the post-tensioning process

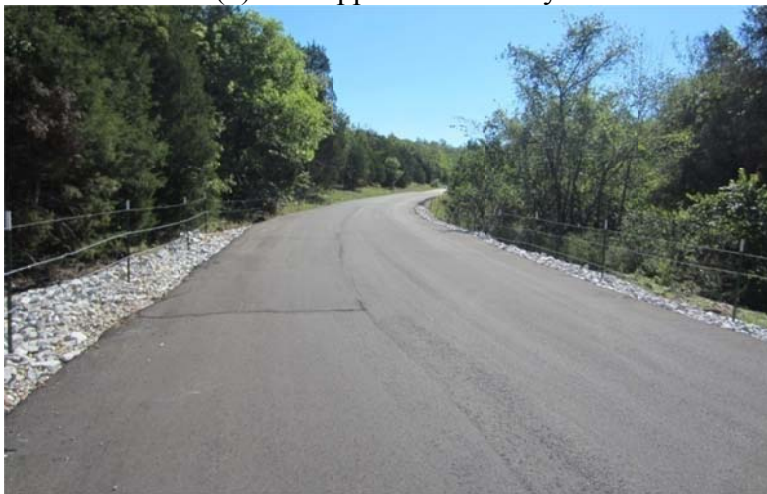
Figure 5.20: Post-tensioning of one CFRP tendon



(a) Finished bridge with 3-in. asphalt wearing overlay



(b) East approach roadway



(c) West approach roadway

Figure 5.21: Overview of the bridge

Chapter 6. Overview of Laboratory and Field Test Programs

6.1 Introduction

This Chapter describes the laboratory and field test programs of precast deck slabs and box girders of the bridge. Laboratory tests were performed with one representative concrete slab and one concrete box girder in the Highbay Structures Laboratory at Missouri S&T. Field tests were conducted with one or two fully-loaded vehicles one month after the completion of bridge construction with the placement of a 3-in. asphalt overlay wearing surface. An emphasis is placed on the load testing procedure and instrumentation setup at the bridge site. In-depth discussion on the testing data and performance of the deck slab and box girder will be included in Chapters 7 and 8, respectively. Long-term performance of the bridge system will be monitored in the years to come.

6.2 Laboratory testing program of bridge elements

To understand the flexural and/or shear behavior and validate the design of the proposed precast deck slabs and box girders reinforced with GFRP bars, laboratory tests were carried out for one full-size concrete deck slab and one full-size concrete box girder as indicated in Figure 6.1. Further details for laboratory deck slab and box girder tests will be addressed in Chapter 7 and Chapter 8, respectively.

6.3 Load rating for field tests

6.3.1 Load rating

Load rating is a measure of bridge live load capacity, which is a function of the material

properties, structural configuration and geometry, and boundary conditions of a bridge under a certain standard vehicle load (Huria et al., 1994). The bridge rating is usually done using the recommended material properties and thus quite conservative in most cases. Careful considerations should be given to the factors that can unnecessarily cut short of the bridge service life. Bridges are often rated in two categories: operating rating and inventory rating. The Operating Rating represents the maximum permissible load that should be allowed on the bridge. Exceeding this level could damage the bridge. Even at the Operating Rating level, unlimited usages of a bridge can reduce the life of the bridge. The Inventory Rating is the load level that the bridge can carry on a daily basis without damaging the bridge. The Operating Rating is based upon the appropriate ultimate capacity using the current AASHTO specifications. Load posting is established using the H20 and 3S2 vehicles at 86% of the Operating Rating. According to MoDOT's current load rating guidelines, any structure built, rehabilitated, or reevaluated shall be rated using the Load Factor Method (MoDOT, 1996). The legal load in Missouri is 23 tons for H20 vehicles (MoDOT, 1996). In many cases, the deficiency in demand is only a small percentage of the capacity of the bridge. Therefore, upgrading these bridges can provide savings for state DOTs and lead to the removal of many load posting signs.

6.3.2 Truck weight and size

A literature review demonstrated that using loaded dump trucks for bridge field tests has been widely accepted as an effective and simple means to evaluate new or rehabilitated bridges (Nystrom et al., 2002). The load testing procedure for the field tests of the Washington County Bridge was conducted by using two fully loaded H20 dump trucks provided by MoDOT, as shown in Figures 6.2a through 6.2d. The loaded tandem-axle dump truck(s) were placed at various bridge locations according to Figures 6.2c and 6.2d. The dimensions of the two dump

trucks were listed in Table 6.1. Each truck weighed 44 kips (196.4 kN) and was slightly lighter than that specified in MoDOT (46 kips). From the front to the rear of each truck as schematically displayed in Figure 6.2b, the axle loads were 13.67 kips (61.05 kN), 15.05 kips (67.2 kN), and 15.27 kips (67.18 kN), respectively.

6.4 Truck positions and load protocols for field tests

To collect a meaningful set of data from the new bridge, a preliminary design of load patterns was conducted. Each span of the bridge was idealized as a simply supported beam along longitudinal direction (traffic flow) based on the boundary conditions, as shown in Figure 6.3a. Similarly, the bridge deck was simplified as a four-span continuous beam restrained by five steel/concrete girders along transverse direction. Several passes of the truck(s) were made at various transverse and longitudinal positions on the bridge.

6.4.1 Truck position along the longitudinal direction

The maximum positive bending moment of a simply-supported bridge span is achieved at the location of slightly off the mid-span as illustrated in Figure 6.3a under a three-axle truck. The maximum shear force over the span can be found at either end of the span, depending on the truck direction. For the maximum effects on bending moment and shear force, four truck patterns were chosen as shown in Figures 6.4a through 6.4d. The bridge span was then analyzed for various load patterns; the shear force, bending moment and deflection in $1/EI$ were plotted in Figures 6.4a through 6.4d. Figure 6.4a showed the load pattern that created the maximum shear force while Figure 6.4c likely results in the maximum positive bending moment. As such, four load patterns in Figures 6.4a through 6.4d were utilized to guide the load testing of the bridge as illustrated in Figure 6.7.

6.4.2 Truck pass along the transverse direction

Several passes of the truck(s) were selected to create the maximum responses to exterior girder, interior girder, and deck slab, respectively. Several load patterns used during the field testing were plotted in Figures 6.5a through 6.5e based on the extensive parametric studies. For example, Load Case 1 as shown in Figure 6.5a can produce the maximum deflection at the exterior girder when the truck passed across the top of the girder by the minimum distance of 24 in.(61 mm) away from the edge. Figure 6.5b plotted the maximum response of the deck slab when the truck was over the middle of slab between the first and second girders. The maximum response of the interior girder can be found in Load Case 3 as shown in Figure 6.5c. It should be noted that the minimum specified clear distance from center to center axles for two trucks was 4 ft (1.22 m) as indicated in Figure 6.5e. Based on the truck configuration with axle loads and spacing, two truck location 4 (Figure 6.5d) corresponded to the worst-case loading condition for the maximum deflection of interior girder at mid-span. Thus, three truck passes were selected (Load Case 1 through 3 with one truck in Figures 6.5a through 6.5c) while the fourth truck pass was utilized for two truck passing through the bridge as shown in Figure 6.5d. Moreover, to account for the dynamic response of the bridge, two additional passes were conducted at 35 mph (56 kph) for one truck (pass 1) and at 15 mph (24 kph) for two trucks (pass 4). Consider the symmetry of the bridge, the truck patterns for symmetric load passes were ignored.

6.4.3 Load protocol for field tests

In general, truck passes and stops along both transverse and longitudinal directions were plotted in Figure 6.6. Several photos in Figure 6.7 illustrated the truck stops during load testing. The load protocol for Passes 1 through 4 and Stops 1 through 4 was selected based on the design for individual transverse and longitudinal directions. Overall, six groups of tests were conducted

as summarized in 21 test cases in the test matrix in Table 6.2. The first four groups of tests were performed with one truck passing the predetermined locations (Stop 1 through 4) as illustrated in Figures 6.8 through 6.13. The other group of tests (Groups 5 and 6 in Table 6.2) were performed by utilizing two trucks. Specifically, Groups 4 and 6 were designed to have truck(s) passing at a predetermined speed over the bridge. For convenience in discussion, a test identification (ID) code was developed to represent the No. of truck, loading type, and truck stop as summarized in Table 6.2. For example, SDLC 042 represents the test Group 4 with a single truck parked at Stop 2. Typical truck stop sign and traffic control were illustrated in Figures 6.14a and 6.14c.

6.5 Instrumentation plan for field tests

6.5.1 Instrumentation Layout

With the aforementioned load patterns, the instrumentation layout was correspondingly designed to collect a meaningful set of data for bridge engineering and design. Both structural symmetry and simple support of each bridge span were taken into account in the design of instrumentation. In combination with the embedded strain gauges during precast element casting as discussed in Chapter 4, the field test instrumentation layout was designed such that both transverse and longitudinal distributions of truck loads among steel/concrete girders in the first and third spans, stress distribution among CFRP bars in each deck slab, load distribution inside each box girder in the middle span, and load transfer between adjacent box girders can be investigated. Specifically, emphasis was placed on the response measurement along girders on north side (upstream) and near the mid-span of each bridge span. The instrumentation details were slightly different for the precast deck slabs in the first/third spans and box girders in the second span.

Twenty direct current, linear variable differential transformer (DC-LVDT) transducers were mounted on stands underneath the bridge, as shown in Figure 6.15, to monitor the vertical deflections of the bridge deck and girders as truck(s) was driven over the bridge. For the first and third spans as shown in Figure 6.15(a), five DC-LVDT transducers were placed along the north exterior girder, five along the center girder, three on other girders at mid-span, six between Girder 1 and Girder 2 at various longitudinal positions, and one between Girder 2 and Girder 3 at mid-span. For the middle span as shown in Figure 6.15(b), five DC-LVDT transducers were instrumented along the centerline of the north exterior box girder, five along the north interior box girder, and ten on all four box girders at mid-span.

Seven accelerometers were mounted on each span as illustrated in Figure 6.16 to evaluate the acceleration response as truck(s) passed through the bridge at a predetermined speed. For the first or third span, five accelerometers were placed along the center girder and the other two on the north side girders at mid-span. For the middle span, five accelerometers were deployed along the centerline of the north exterior girder and the other two were placed on the north-side interior girder at mid-span. In addition, six inclinometers were mounted on the end deck slab as shown in Figure 6.17a or along the north exterior box girder as shown in Figure 6.17b. As a truck passed through the bridge, the data collected from the inclinometers were used to understand the longitudinal and transverse rotation distribution in a small region for the steel/concrete girder span, and to understand the global distribution of rotations in the middle span, respectively. A series of photos that illustrated the installation process of various sensors are shown in Figure 6.18.

6.5.2 Data collection

As mentioned previously, the strain gauges embedded in the precast bridge elements were used to provide short-term and long-term performance monitoring of the new bridge. Strain data can be collected with the Smarbrick unit or other standard data acquisition as previously described in Chapter 4. Its prototype devices have been tested in the laboratory to verify reliability and repeatability of results and have been compared to analytical results. Field measurements of deflection, rotation and acceleration using DC-LVDTs, inclinometers and accelerometers were taken with a multi-channel yellow box as shown in Figure 6.19.

6.6 Summary

This Chapter discussed the setup and instrumentation of laboratory and field tests. For field testing, the type of truck(s) and their positions as well as load protocol were first determined. Instrumentation layout was then designed corresponding to various positions of loading. With the load protocol and test program, performance of the precast bridge elements and the entire bridge system can be evaluated in laboratory and field conditions. The test data and results are presented in the following chapters.

Table 6.1: Truck axle spacing

	Center-to-center spacing (ft)	
Width	Front axle	6.63
	Middle axle	6.14
	Rear axle	6.14
Length	From front axle to middle axle	15.1
	From middle axle to rear axle	4.3

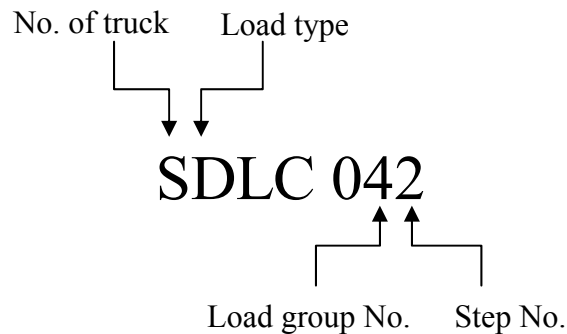
Note: 1 ft = 0.305 m

Table 6.2: Loading case records in field tests

No.	Load group	Stop	Pass	I.D.	Load type	Temperature		time	Note
						Initial	Final		
1	1	1	1	SSLC 011	Static				Single truck
2		2	1	SSLC 012	Static				
3		3	1	SSLC 013	Static				
4		4	1	SSLC 014	Static				
5	2	1	2	SSLC 021	Static				
6		2	2	SSLC 022	Static				
7		3	2	SSLC 023	Static				
8		4	2	SSLC 024	Static				
9	3	1	3	SSLC 031	Static				
10		2	3	SSLC 032	Static				
11		3	3	SSLC 033	Static				
12		4	3	SSLC 034	Static				
13	4	1	1	SDLC 041	Dynamic				V=35 mph
14		2	1	SDLC 042	Dynamic				
15		3	1	SDLC 043	Dynamic				
16	5	1	4	DSLCL 051	Static				Double trucks
17		2	4	DSLCL 052	Static				
18		3	4	DSLCL 053	Static				
19		4	4	DSLCL 054	Static				
20	6	1	4	DDLCL 061	Dynamic				V=15 mph
21		2	4	DDLCL 062	Dynamic				

Note: SSLC = Single truck under Static Load Case, SDLC = Single truck under Dynamic Load Case, DSLC = Double trucks under Static Load Case, DDLC = Double trucks under Dynamic Load Case.

Test Case Identification:



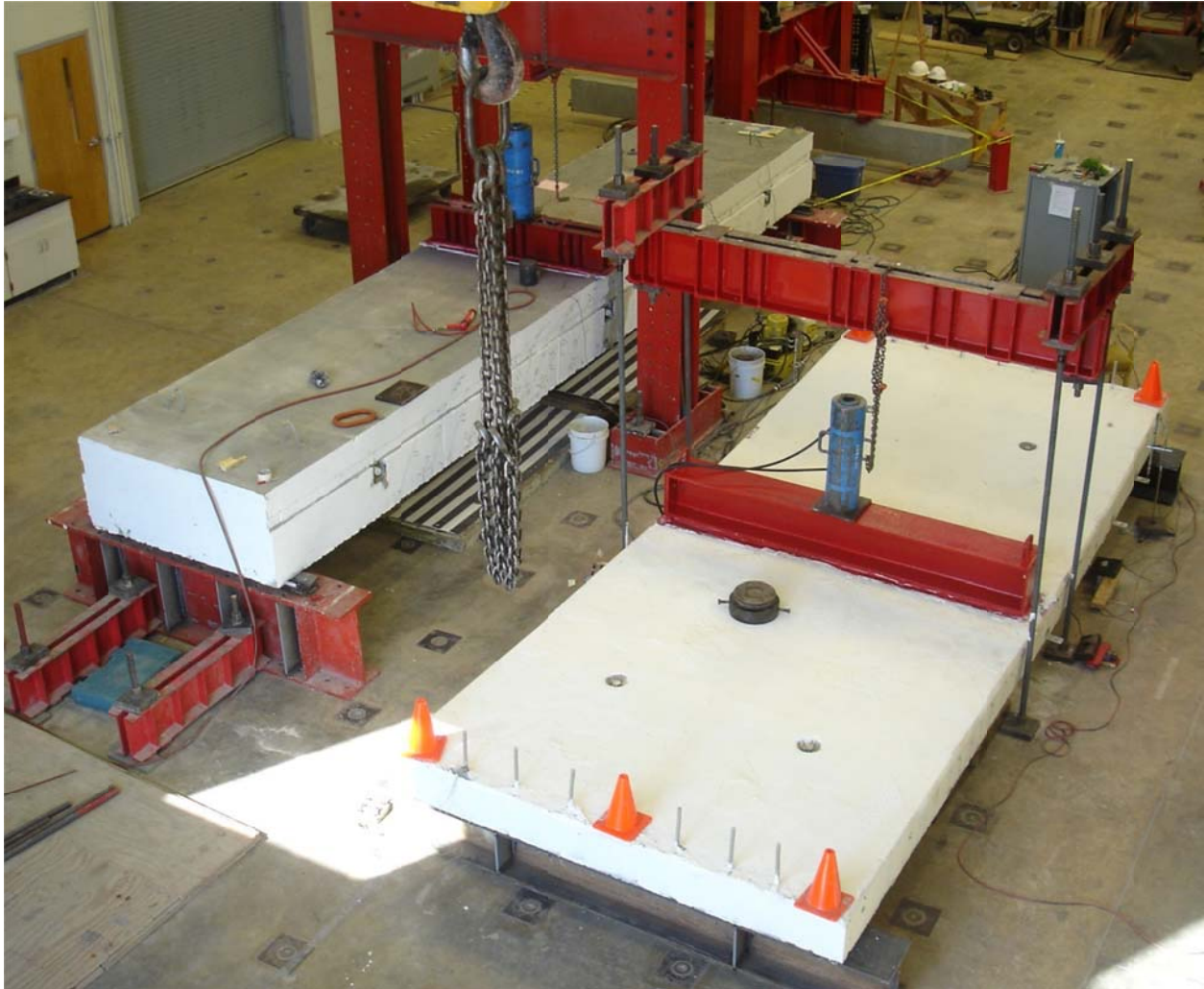
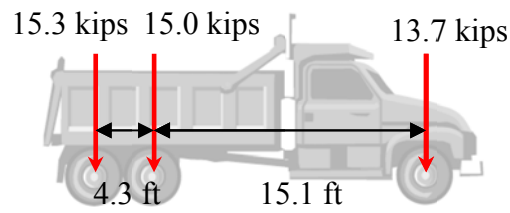


Figure 6.1: Overview of laboratory test setups for full-scale precast bridge elements



(a) Fully loaded dumb truck (44 kips total)



(b) Truck load distribution (1 kip = 4.448 kN and 1 ft = 0.305 m)

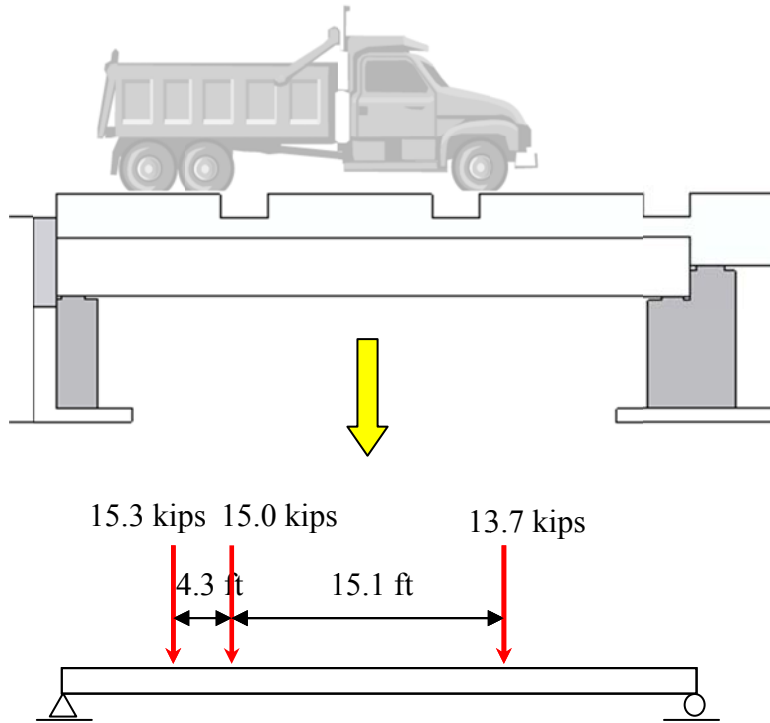


(c) Load cases with one truck

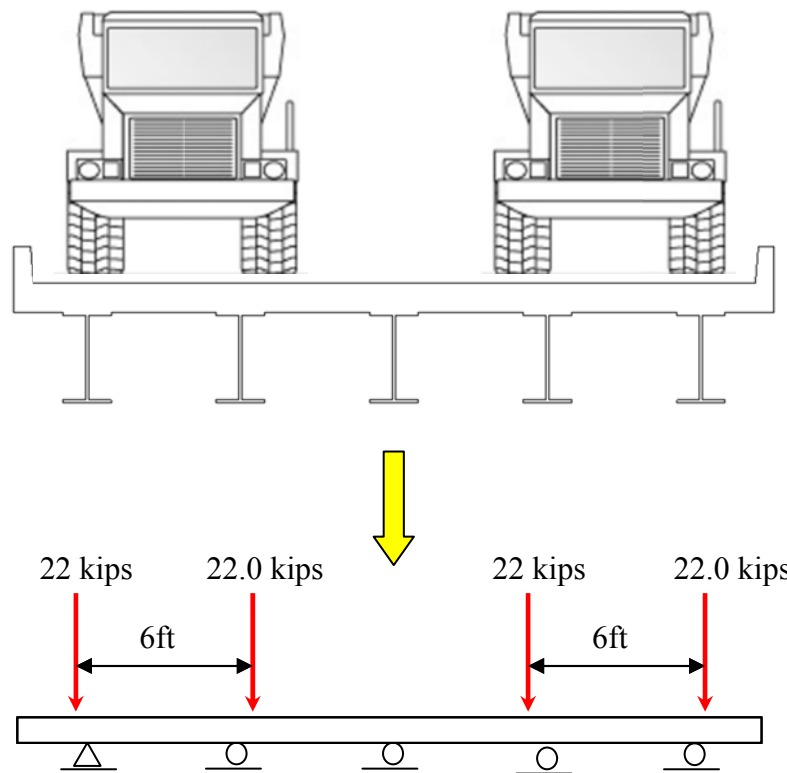


(d) Load cases with two trucks

Figure 6.2: Trucks used in field tests



(a) Idealized simply-supported beam along longitudinal direction (traffic flow)



(b) Idealized continuous beam along transverse direction (river flow)

Figure 6.3: Preliminary design of load protocol for field tests

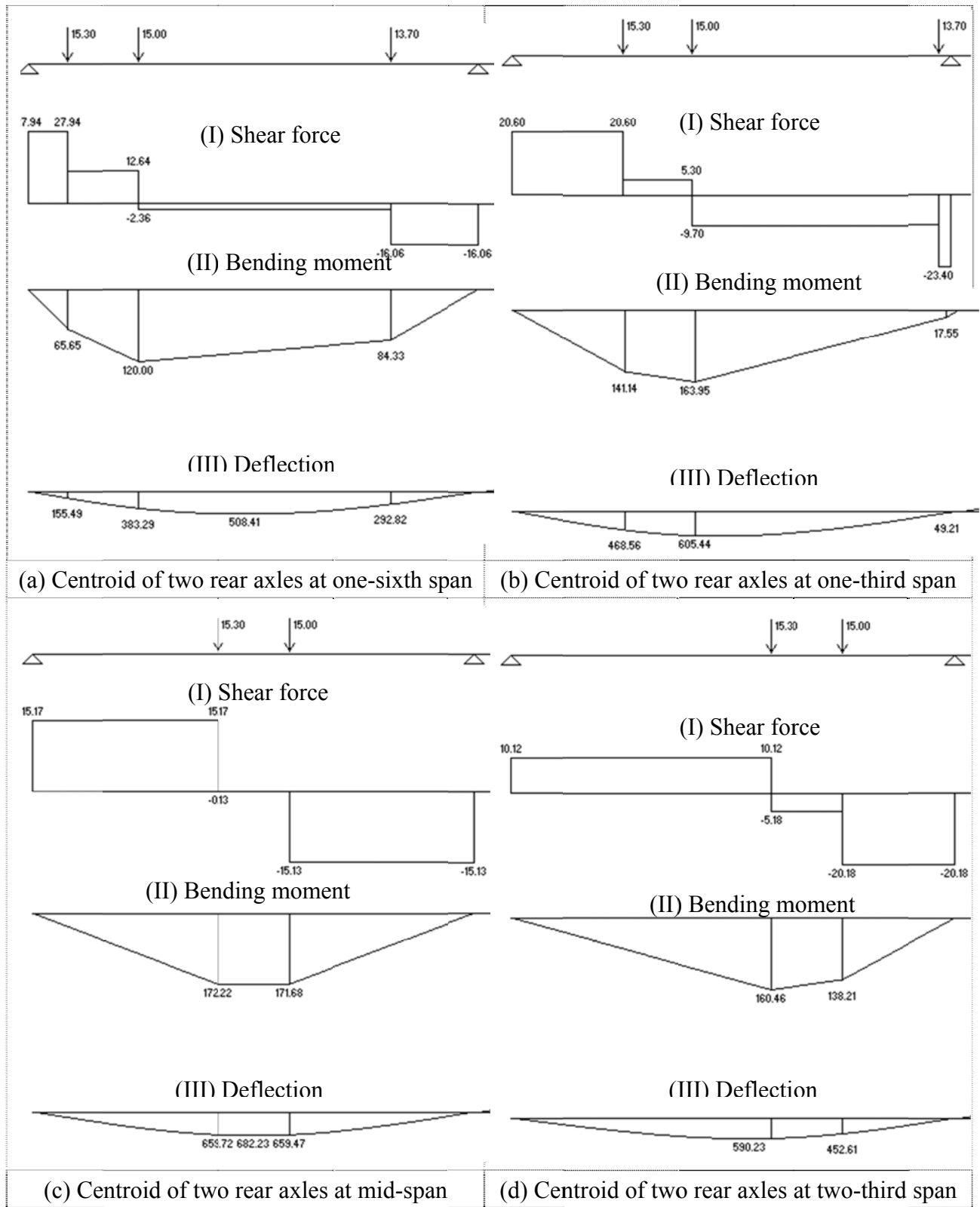
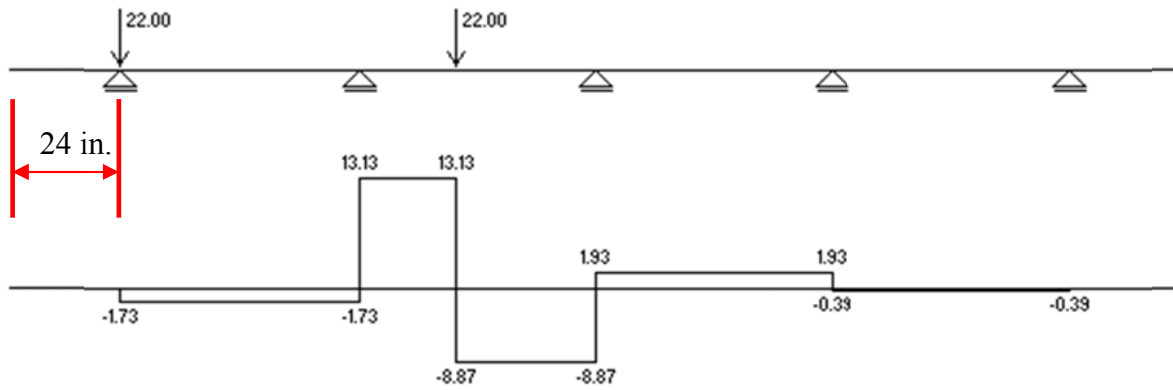
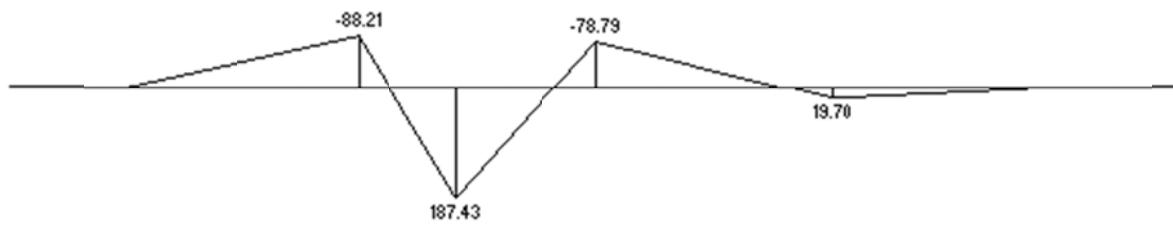


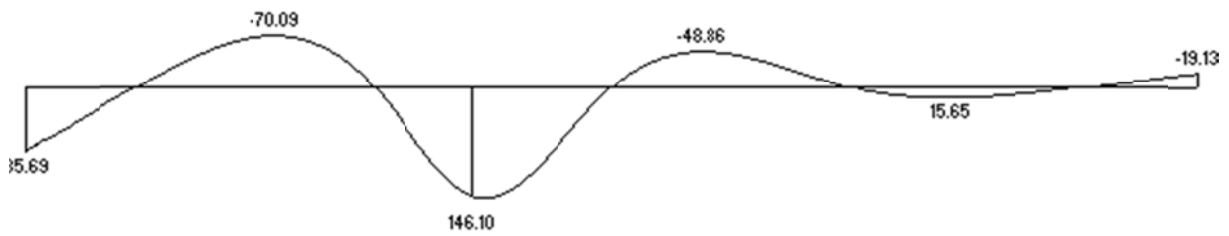
Figure 6.4: Determination of truck location in longitudinal direction for field tests



(I) Shear force

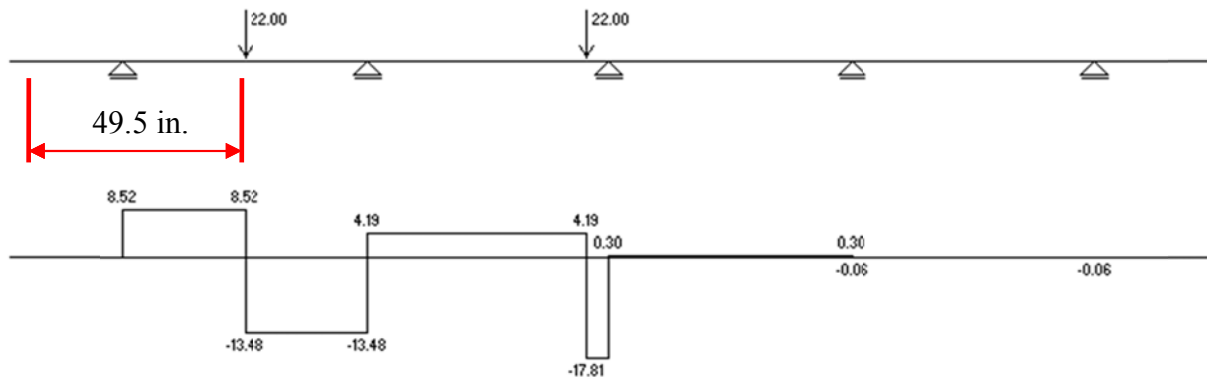


(II) Bending moment

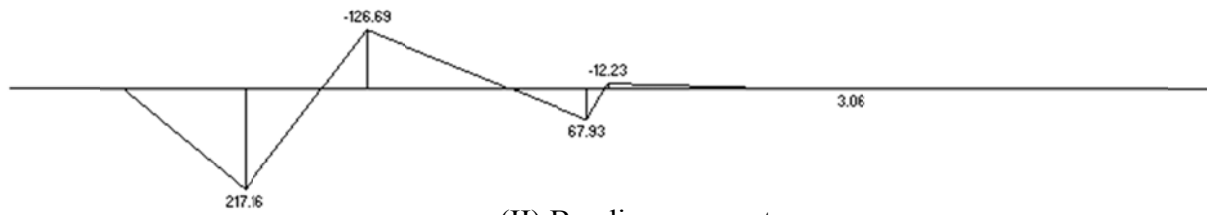


(III) Deflection

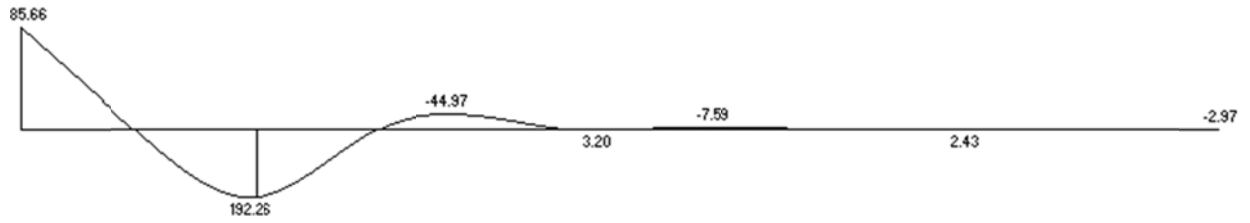
(a) Load case 1 with one truck



(I) Shear force

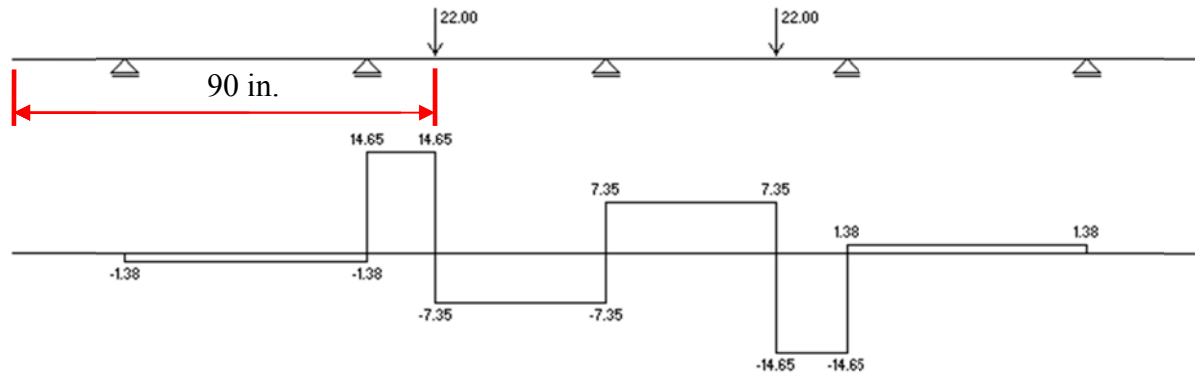


(II) Bending moment

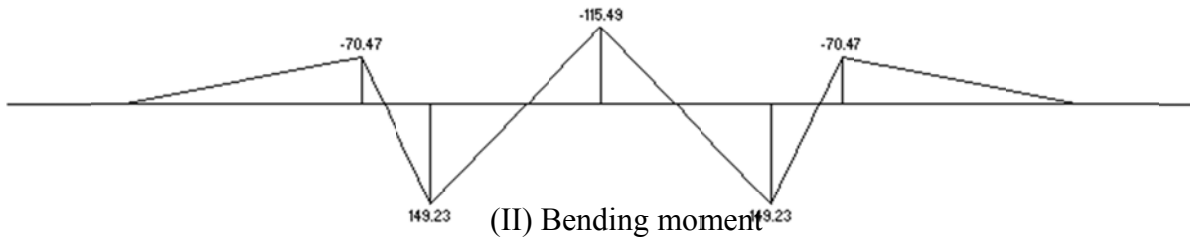


(III) Deflection

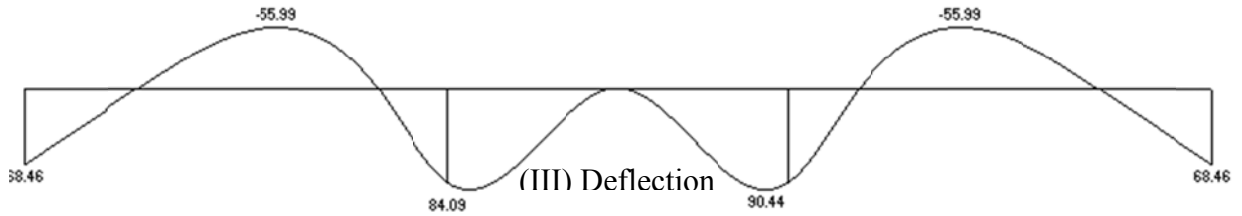
(b) Load case 2 with one truck



(I) Shear force

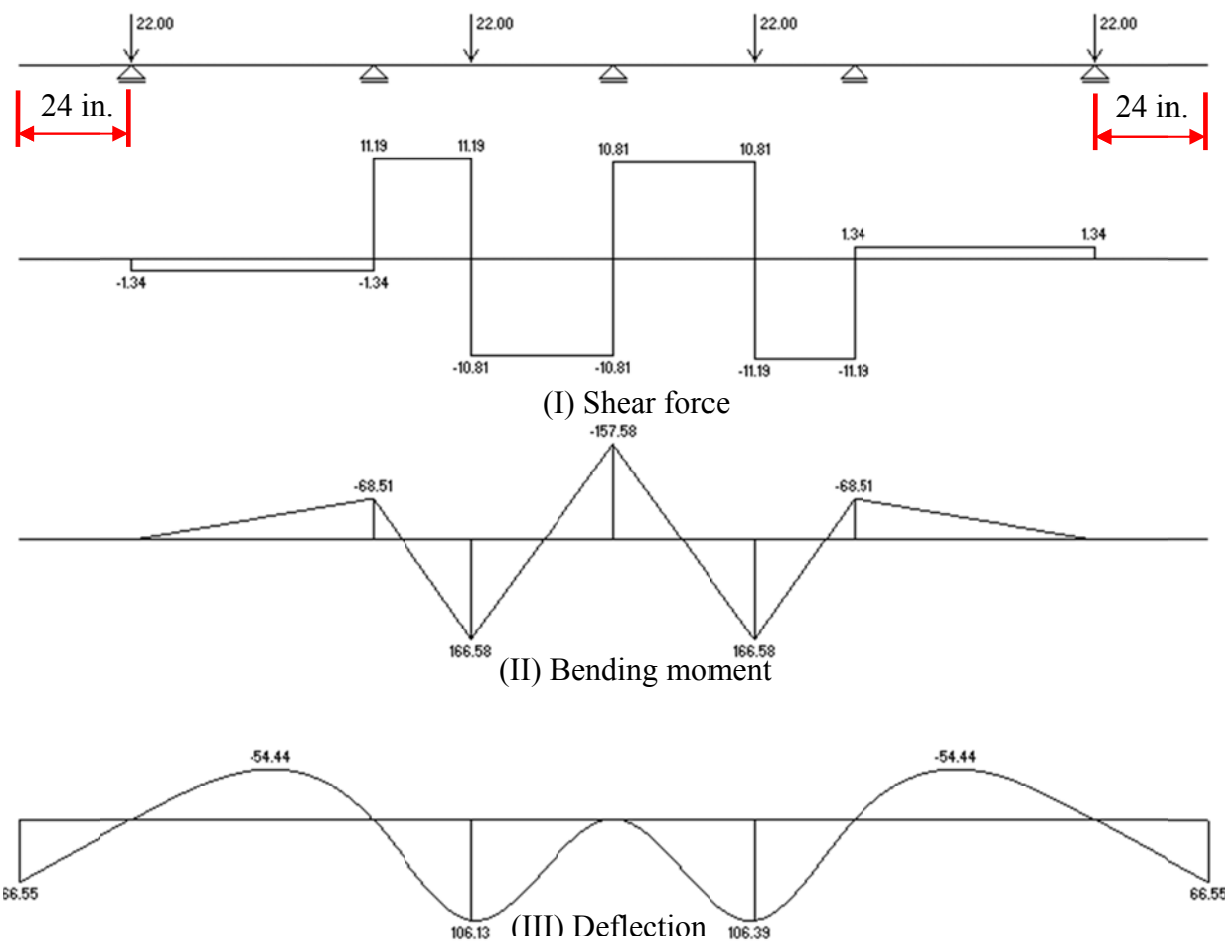


(II) Bending moment

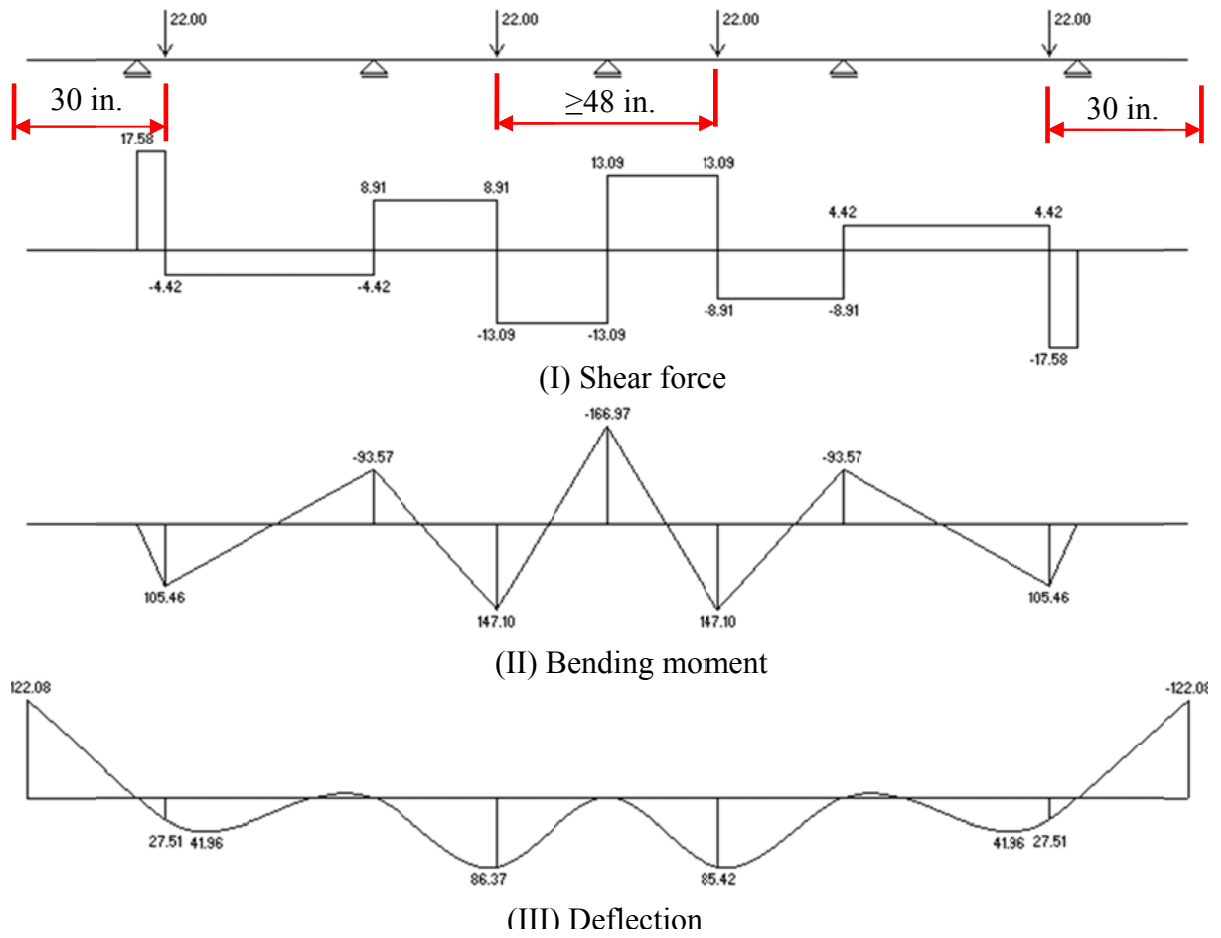


(III) Deflection

(c) Load case 3 with one truck

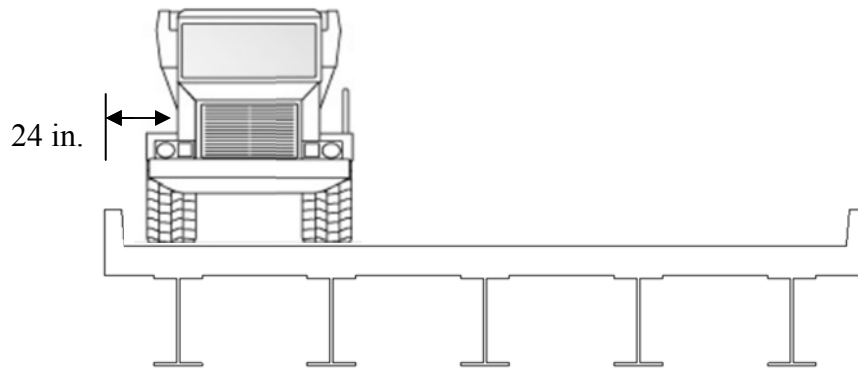


(d) Load case 4 with two trucks

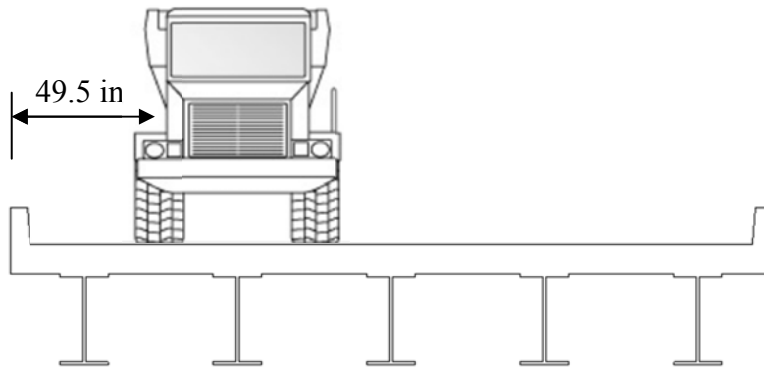


(e) Load case 5 with two trucks

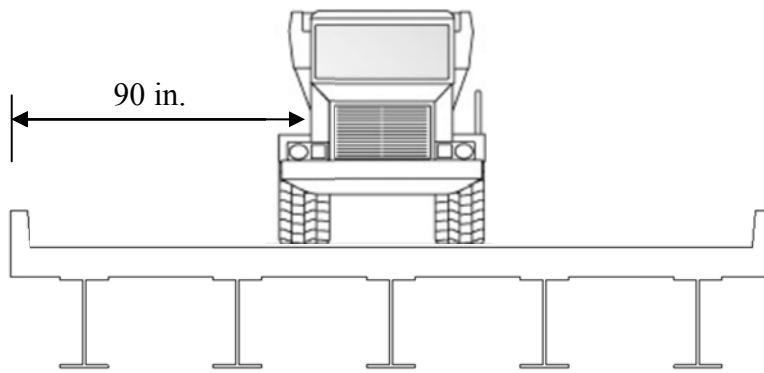
Figure 6.5: Determination of truck location (pass) in transverse direction for field tests



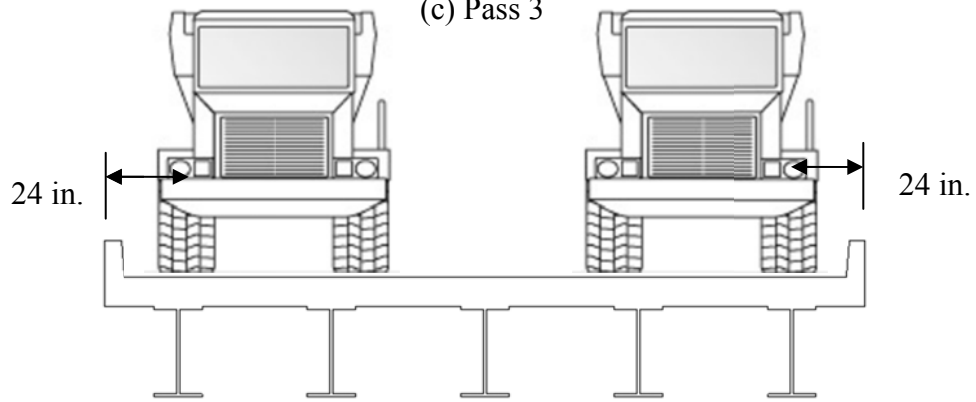
(a) Pass 1



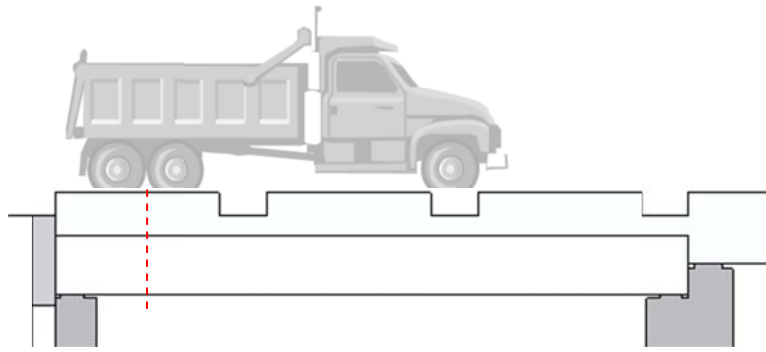
(b) Pass 2



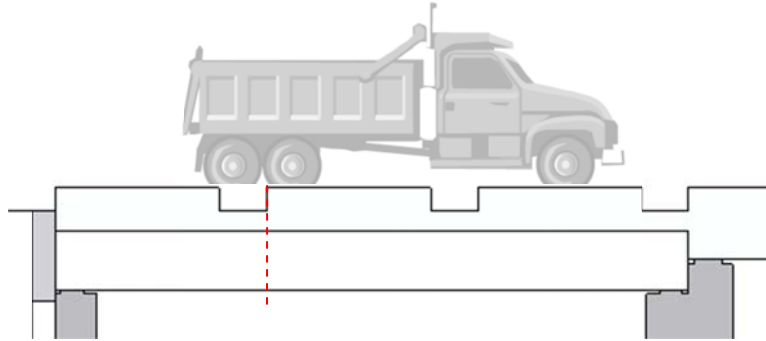
(c) Pass 3



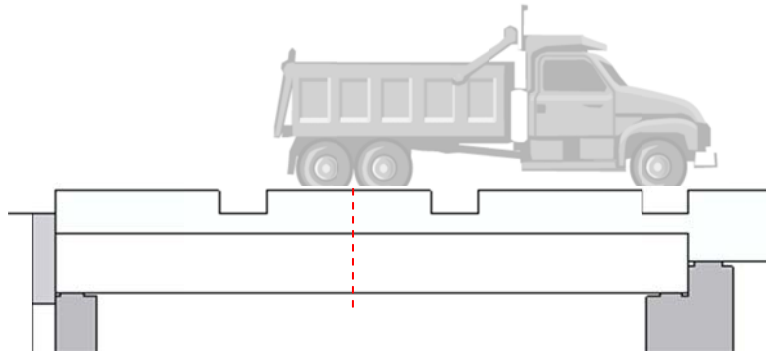
(d) Pass 4 (two trucks)



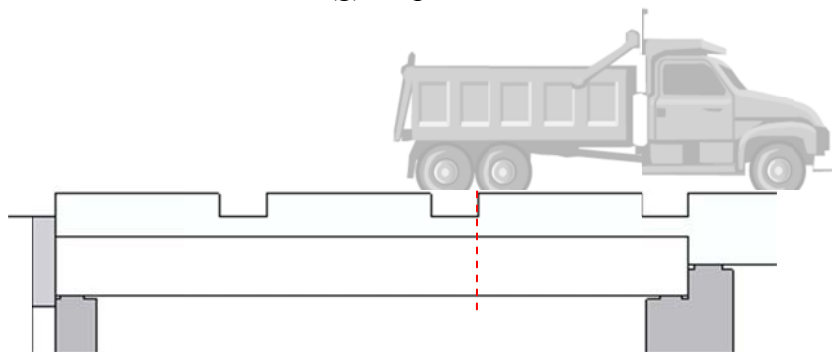
(e) Stop 1



(f) Stop 2



(g) Stop 3

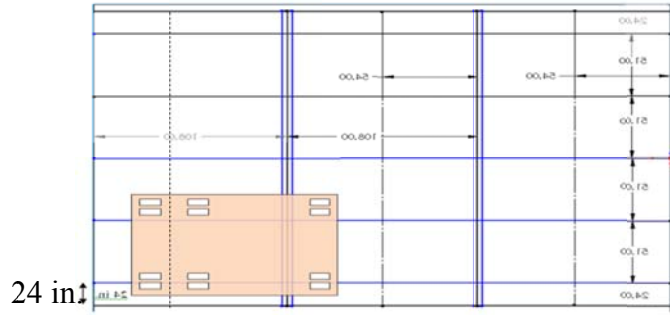


(h) Stop 4

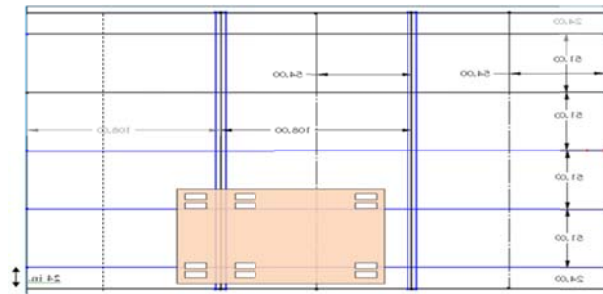
Figure 6.6: Schematics of locations of truck passes and stops



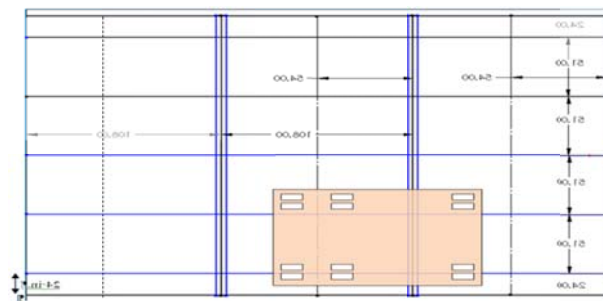
Figure 6.7: Illustrated four steps of one truck over each span



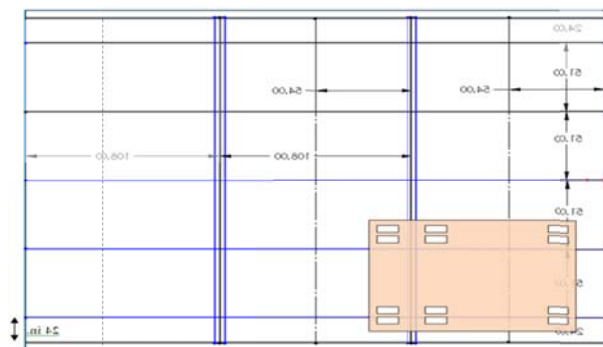
(a) SSLC 011(one truck, static)



(b) SSLC 012(one truck, static)

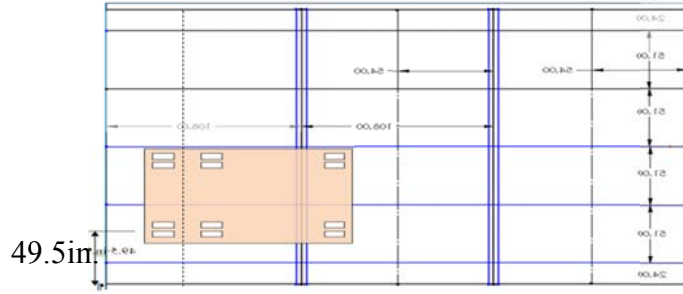


(c) SSLC 013(one truck, static)

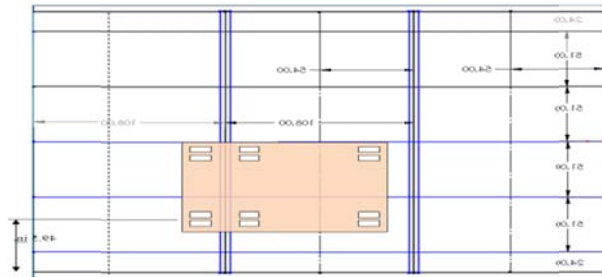


(d) SSLC 014 (one truck, static)

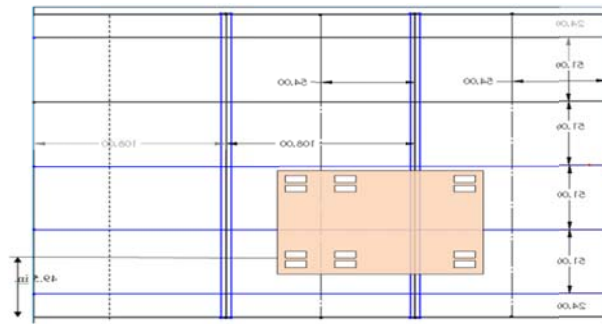
Figure 6.8: Load cases SSLC 011 to SSLC 014



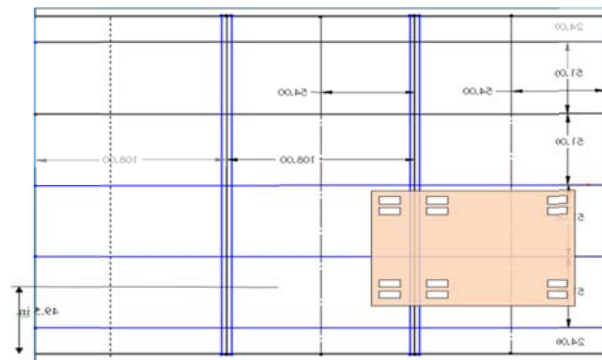
(a) SSLC 021(one truck, static)



(b) SSLC 022(one truck, static)

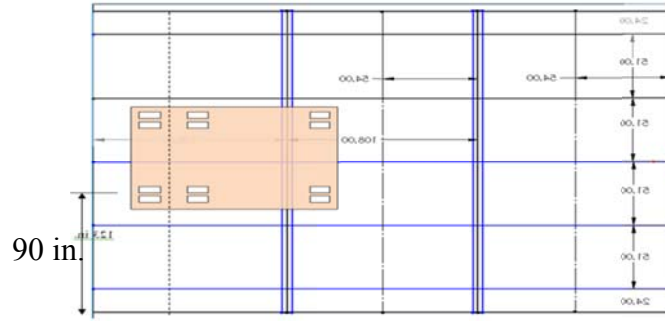


(c) SSLC 023(one truck, static)

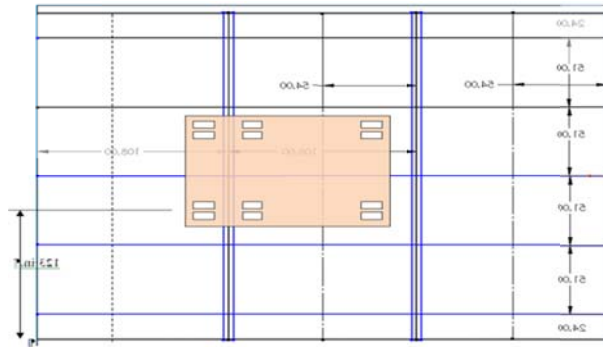


(d) SSLC 024 (one truck, static)

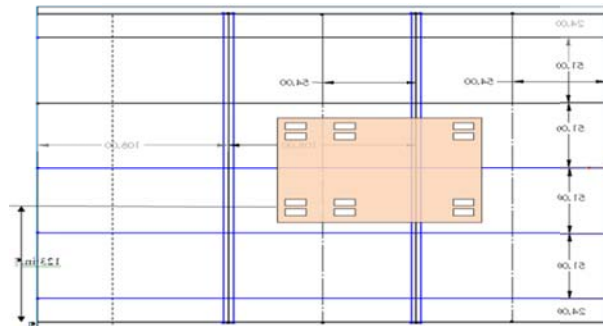
Figure 6.9: Load cases SSLC 021 to SSLC 024



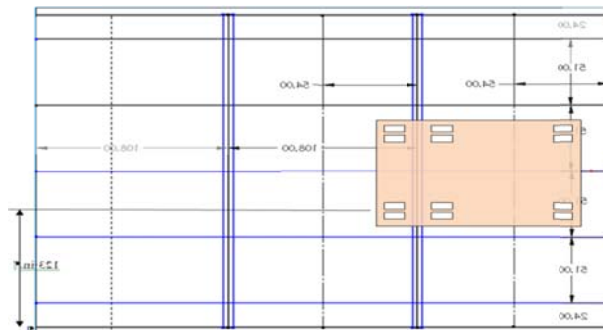
(a) SSLC 031(one truck, static)



(b) SSLC 032(one truck, static)

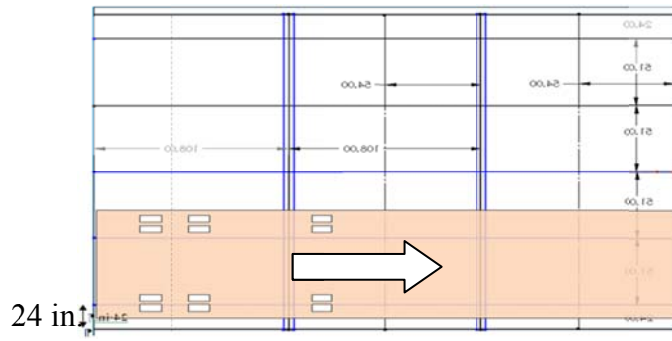


(c) SSLC 033(one truck, static)

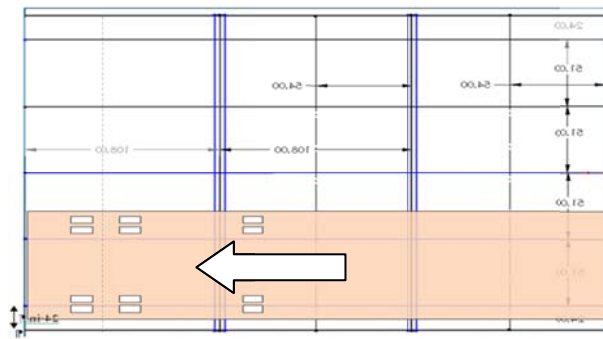


(d) SSLC 034 (one truck, static)

Figure 6.10: Load cases SSLC 031 to SSLC 034

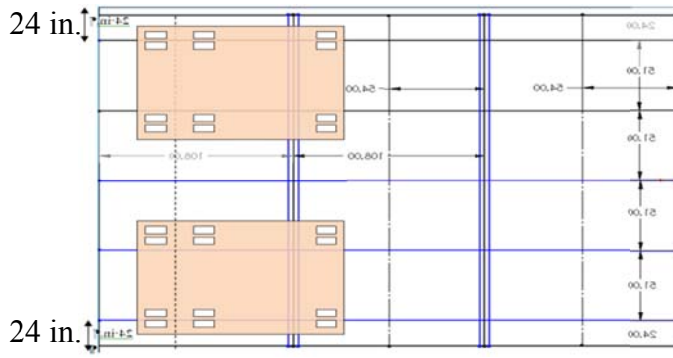


(a) SDLC 041

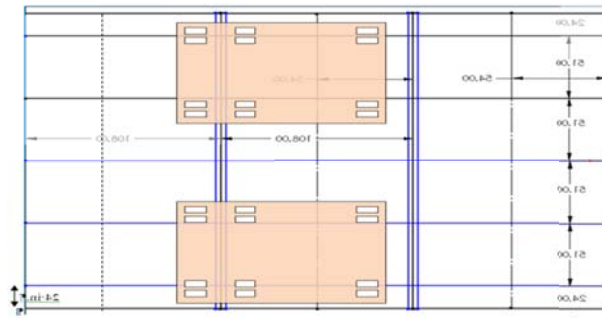


(b) SDLC 042

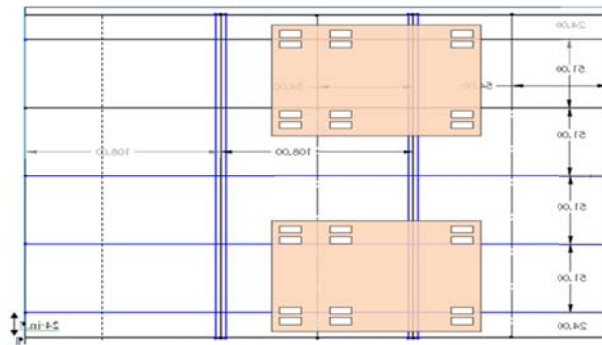
Figure 6.11: Load cases SDLC 041 and SDLC 042 (one truck, dynamic with $v=35$ mph)



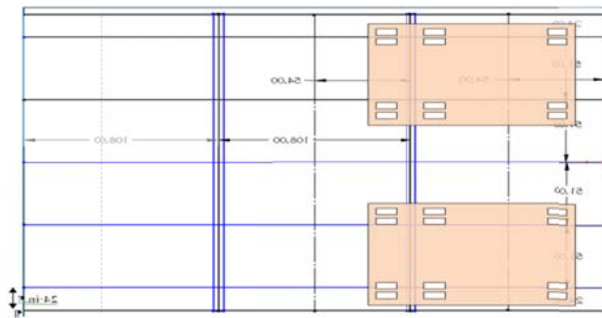
(a) DSLC 051



(b) DSLC 052

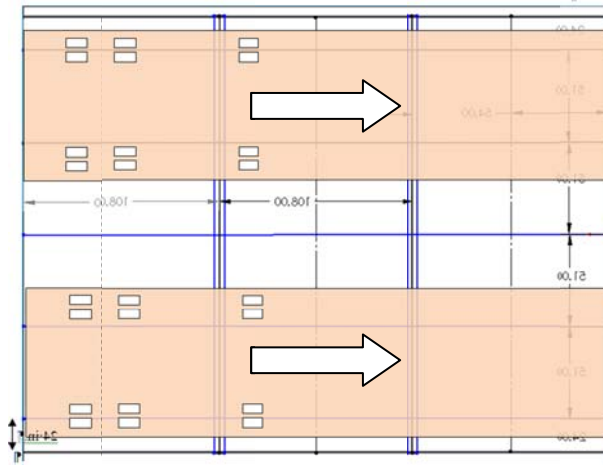


(c) DSLC 053

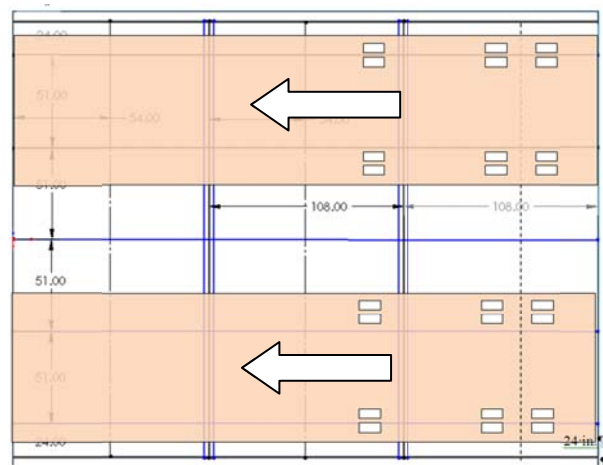


(d) DSLC 054

Figure 6.12: Load cases DSLC 051 to DSLC 054 (two trucks, static)



(a) DDLC 061



(b) DDLC 062

Figure 6.13: Load cases DDLC 061 and DDLC 062 (two trucks, dynamic with $v=15$ mph)



(a) Truck stop (back view on signs on pavement)

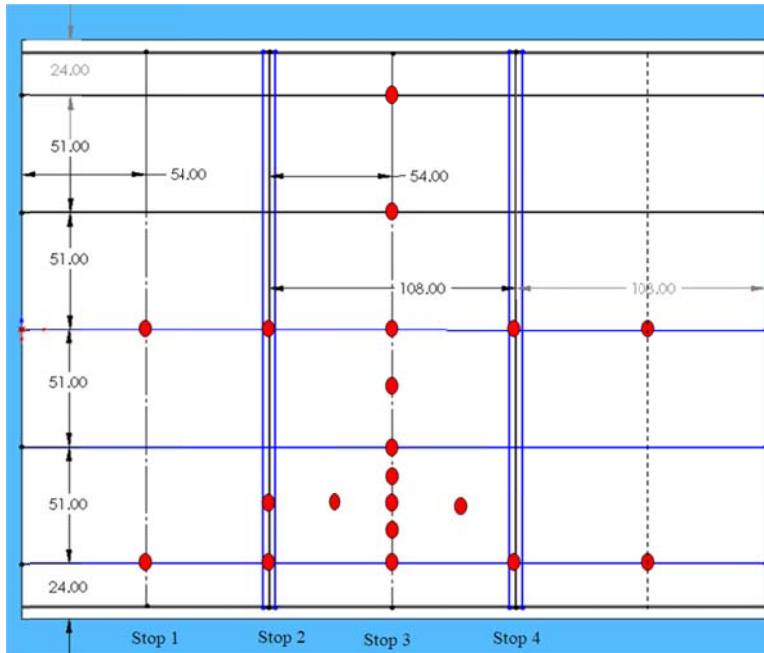


(b) Truck stop (side view on signs on pavement)

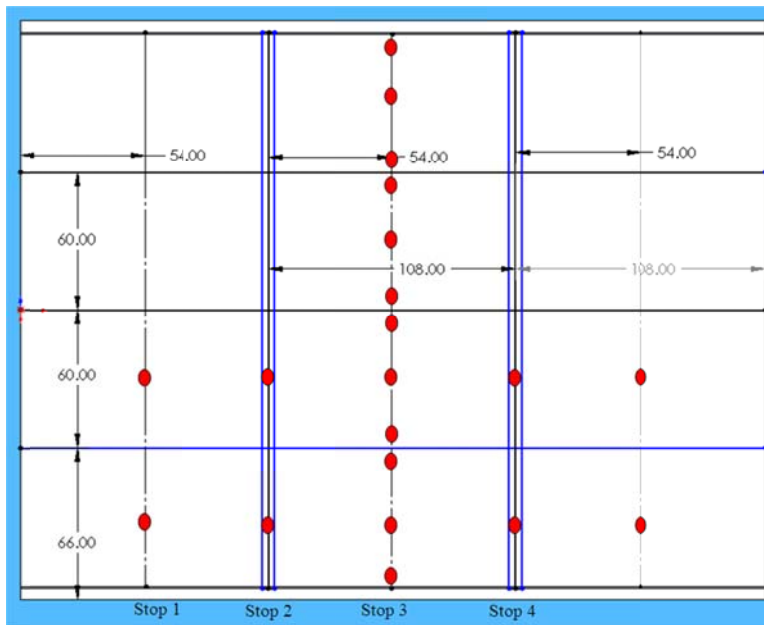


(c) Traffic control at both approach roadways

Figure 6.14: Stop signs and traffic control

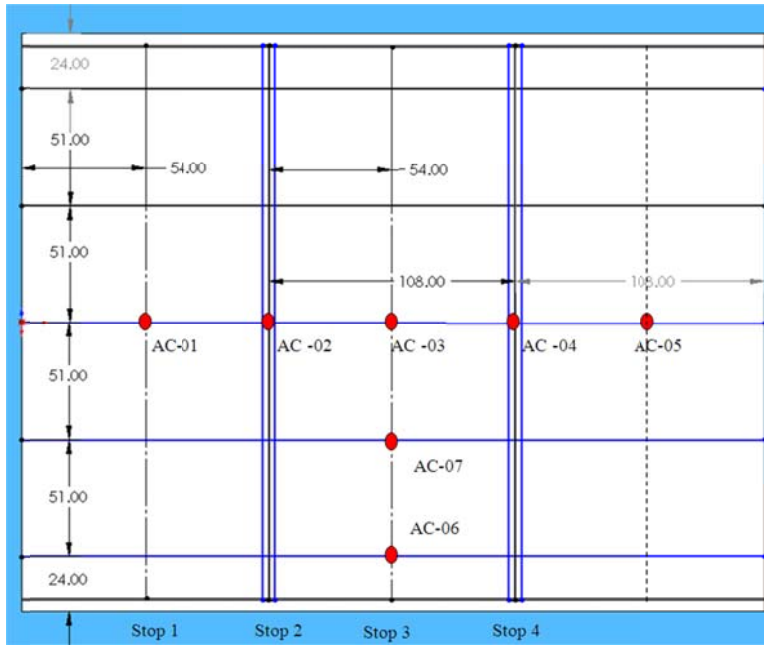


(a) Concrete/steel girder supported deck slabs in the first and third spans

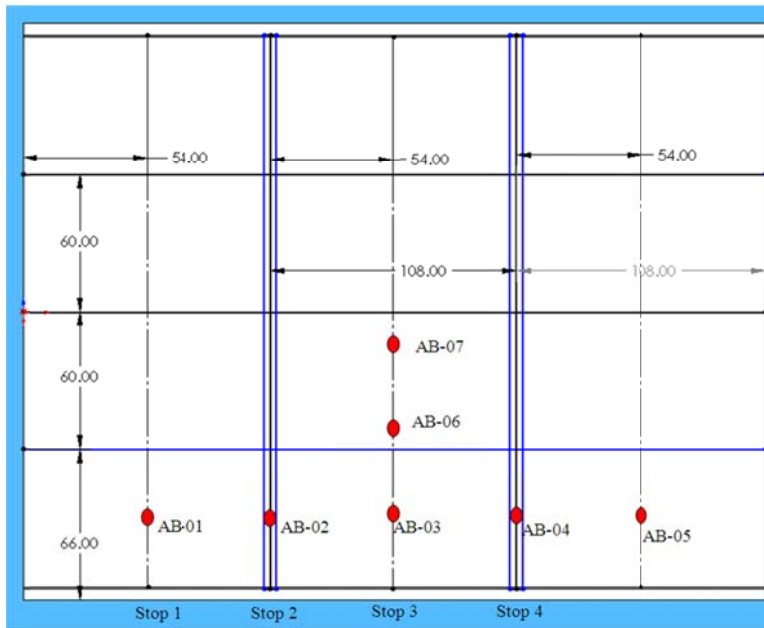


(b) Concrete box girders in the middle span

Figure 6.15: DC-LVDT transducers layout (red dots)

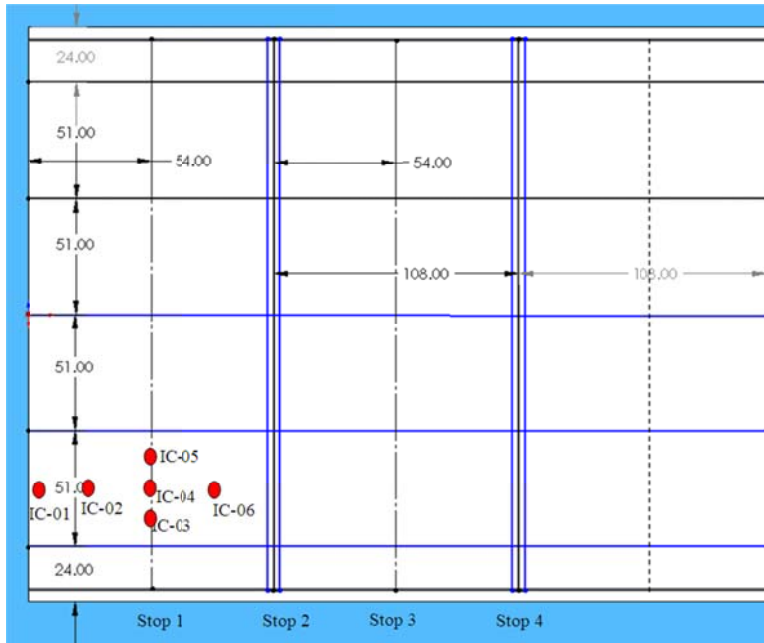


(a) Concrete/steel girder supported deck slabs in the first and third spans

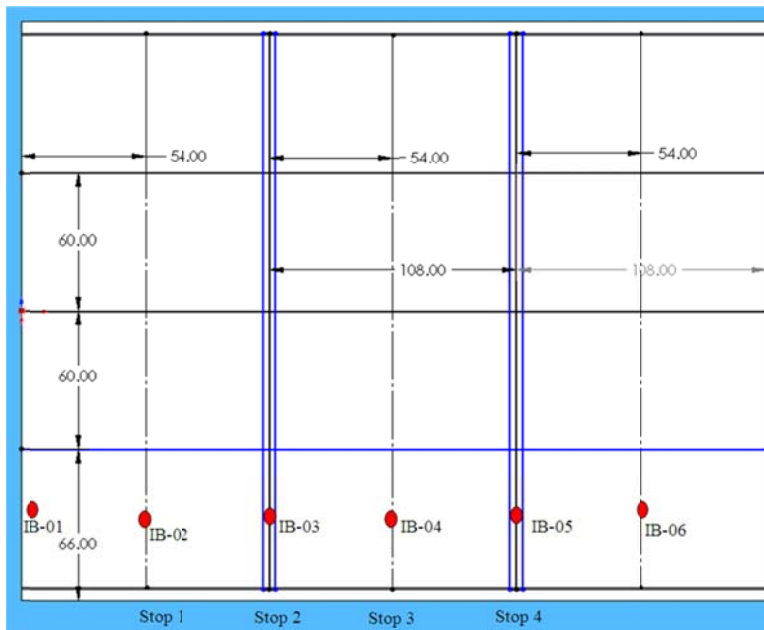


(b) Concrete box girders in the middle span

Figure 6.16: Accelerometer layout (red dots)



(a) Concrete/steel girder supported deck slabs in the first and third spans



(b) Concrete girders in the middle span

Figure 6.17: Inclinometer layout (red dots)



Figure 6.18: Installation process of representative sensors



(a) Data collection



(b) Data acquisition system

Figure 6.19: Data collection and acquisition system used in field testing

Chapter 7. Performance of GFRP-bar Reinforced Concrete Slabs

7.1 Introduction

In this chapter, the mechanical behavior of GFRP-bar reinforced concrete deck slabs was evaluated with laboratory and field tests. The overall test program was discussed in Chapter 6. Here the test program, setup, instrumentation, results and discussion are detailed.

7.2 Laboratory test program

7.2.1 Test schemes

The design and precast of GFRP-bar reinforced concrete deck slabs were outlined in Chapter 3. In comparison with traditional steel-reinforced concrete structures that are mainly designed for the ductile failure of steel, the GFRP-bar reinforced concrete slabs were designed to ensure that the concrete crushing in compression zone occurs prior to rupture of the GFRP bars since GFRP bars are basically elastic till fracture, a brittle behavior that must be prevented from happening in actual structures. The relatively lower flexural stiffness and significantly higher rupture strength of GFRP bars allow the GFRP-bar reinforced concrete structures to experience larger displacements than the steel-reinforced structures. By limiting the allowable deflection in design, the significant reserved deformability could potentially provide users of the GFRP-bar reinforced concrete structures with the needed margin of safety and the required reliability to prevent catastrophic failure.

Each deck slab (10 in. or 25.4 mm thick) is supported on five steel/concrete girders, each panel being 9 ft (2.74 m) long and 4.25 ft (1.30 m) wide. The width-thickness ratio is 5.1, which

indicates that both shear and flexural behaviors of the slabs are likely significant in their application condition on the new bridge.

With the intent of verifying the design of precast GFRP-bar reinforced concrete slabs, one representative full-size slab specimen was cast by the same precast company in Springfield, MO. The specimen was identical to those used in the construction of Washington County Bridge except for the curbs at both ends. It was tested with two different span lengths: 20 ft (6.10 m) and 8.5 ft (2.59 m) as illustrated in Figures 7.1a and 7.1b for flexural and shear behaviors.

7.2.2 Test setups

The full-size slab specimen was simply-supported and subjected to three-point bending to evaluate its load-deflection behavior. The first load case with 20 ft (6.10 m) in span length was detailed as illustrated in Figures 7.1a and 7.1c. The second load case with 8.5 ft (2.59 m) in span length was illustrated in Figure 7.1b and 7.1c. The second test with a relatively higher shear effect than the first test was conducted after the completion of the first test on the same specimen. Since little damage was caused in the quarter span during the first load case, the effect of the first load case on the second load case is likely small. In either case, a load applied through a hydraulic jack was uniformly distributed in transverse direction at mid-span of the deck slab. The distributed line loading simulated the traffic load along the traffic direction. Note that a patch loading which is often used to simulate the loading effect of single/double tires on the bridge deck was not used. It was mainly because the global flexural and shear behaviors were of primary interest for the laboratory tests.

The schematic and photographic views of the test setup, including loading frame and hydraulic jack placements, are illustrated in Figures 7.1a through 7.1c and Figures 7.2a through 7.2c for two load cases, respectively. In either case, a steel spread beam was firmly attached to

the top surface of the slab specimen at mid-span and distributed the load produced by the 400-kip (1779-kN) hydraulic jack (Model AN84130) that was reacted against a reaction load frame. The reaction frame included a steel beam spanning over the slab and two pairs of tie-down rods with 2 in. (50 mm) in diameter mounted to the strong floor on two sides of the slab. No-shrink grout and polystyrene were used between the spreader beam and the slab to eliminate potential stress concentration due to an uneven load transfer from the hydraulic jack to the slab, as indicated in Figure 7.3a.

As shown in Figs. 7.1a through 7.1c, the concrete slab rested on two stiffened I-girders at its ends. At each end, a 2-in. diameter bearing rod was placed between the I-girder and the slab, allowing the slab to move horizontally and rotate in the longitudinal plane as shown in Figures 7.1a and 7.2b. In addition, a 2 in. wide and 0.5 in. thick elastomeric pad was provided between the bearing rod and the slab to prevent the potential contact of the excessively deformed slab on the supporting I-girders and prevent concrete crushing due to stress concentration. The details of this support treatment are shown in Figure 7.3b. Such boundary conditions were identical to the actual support conditions of the new bridge as described in Chapter 5.

7.2.3 Instrumentation Plan

The concrete slab was instrumented with DC-LVDT transducers, string pots, and strain gauges. The data acquisition system used to collect test data is illustrated in Figure 7.4. Actual DC-LVDT transducers and their calibration are shown in Figures 7.5 and 7.6. The instrumentation plan is schematically shown in Figures 7.7a through 7.7c. Half of the symmetric specimen was instrumented with DC-LVDT transducers and string pots; only a quarter of the specimen was monitored with strain gauges. A load cell was installed in series with the load cell to record the applied load in each test.

As shown in Figure 7.7a, six electrical resistance strain gauges with a gauge factor of 2.08 were installed on the longitudinal GFRP bars of the slab prior to casting of the specimen and designated as SG-01 to SG-06. Strain gauges were located on several tension and compression reinforcing bars at mid-, and quarter spans, respectively. These strain gauges were used to capture the stress distribution developed in the concrete slab.

The deflections of the deck slab at mid-span and the quarter span, indicated in Figure 7.7b and 7.7c, were measured with four string pots symmetrically deployed at both sides of the slab. The deflections at the one-eighth span were recorded with two DC-LVDT transducers as indicated in Figures 7.7b and 7.7c. These displacement transducers were designated as D1 to D6.

A NI Compact Rio Data acquisition system was used to collect data from all sensors and the force output from the load cell. A sampling frequency of 10 Hz was used in all tests, corresponding to a load rate of 200 lb/min (890 N/min). The collected data was automatically filtered in the NI Compact Rio program.

7.2.4 Load protocols

According to ACI 318-08, the theoretical crack moment of the cross section of the GFRP-bar reinforced slab with 20 ft (6.10 m) span length corresponded to 13 kips (58 kN) in the first load case. Therefore, a half-reversed cyclic load of increasing amplitude at 10 kip (45 kN) interval was applied by the hydraulic jack in force control. Specifically, Figure 7.8 shows the cyclic load protocol for Load Case 1 with load steps at +10, +20, +30, +40, +50, +60, and +70 kips (45, 89, 134, 178, 223, 267, and 312 kN). After 70 kips (312 kN), the specimen was loaded monotonically till failure.

Similarly, the load protocol for Load Case 2 was determined based on the concrete crack moment as shown in Figure 7.9. The cyclic load steps were +70, +90, +110, and +130 kips (312,

401, 490, and 578 kN), respectively. After 130 kips (578 kN), the slab was loaded monotonically till failure. At the end of each load step, the applied load was hold for one to ten minutes for crack marking and measurement on the concrete surface.

7.3 Laboratory test results and discussion

7.3.1 Flexural behavior

Concrete cracks as shown in Figure 7.10 were initially observed at a load level of 10 kips. They all remained vertical, indicating an overall flexural behavior. Due to varying moments, the cracks near the end quarter span were shorter and narrower than those near the mid-span. A series of photos as shown in Figures 7.11a through 7.11d demonstrated the propagation of cracks till the concrete crushing near the top surface of the slab. It is also observed from Figure 7.11 that the slab was displayed excessively prior to failure. Consequently, the horizontal splitting cracks resulting from the concrete crushing and GFRP debonding appeared as detailed in Figures 7.12a and 7.12b when the slab was loaded to 90 kips. The crack patterns in Figures 7.12a and 7.12b demonstrated that the concrete crushing failure initiated around the perimeter of the load spread beam likely due to potential constraining of the spread beam on the top concrete. The slab experienced up to 12 in. deformation before its top concrete cover was completely crushed at compression zone. The large deformability of GFRP-bar reinforced concrete members quite differed from the sudden brittle failure associated with traditional over-reinforced concrete members. Therefore, the slab reinforced with GFRP bars can potentially show a warning sign of flexural failure by exhibiting excessive deformation when properly designed. The test results verified the design of the GFRP-bar reinforced concrete slab.

The load-deflection curves at mid-span, quarter span and one-eighth span were plotted in Figures 7.13a through 7.13c, respectively. All load-deflection curves showed the bi-linear behavior if the loading envelopes were constructed by connecting all the maximum points in various loading cycles. They are similar to those reported in the literature review (Deitz et al., 1999; El-Sayed et al., 2005). Such consistent trends were confirmed in the load-strain curves presented in Figure 7.14. The first straight line ended at the onset of cracking corresponding to the cracking moment of the slab cross section. After the initial cracks, the cracked slab stiffness was reduced to approximately 1/3 of the uncracked slab stiffness as observed from the slope of the second straight line in Figure 7.13a. The slope of the unloading curves at various cycles continued to decrease with the loading level and it lied in between those of the first straight line for the uncracked slab and the second straight line for the cracked slab. Since the GFRP bars in the slab remained elastic till fracture (at over 90 kips), the residual deformation after unloading was less than 2 in. (50.8 mm) at 90 kips loading prior to concrete crushing, though the maximum deflection of the slab was approximately 12 in. (305 mm). The final residual deformation was 3 in. even after crushing of the concrete. The residual deformation was likely caused by the bonding slip between the GFRP bars and concrete matrix. As such, the wrapped and sand-coated GFRP bars contributed to better bonding may actually lead to less residual deformation.

To further explain the flexural behavior of the slab, the bending stresses at the top and bottom GFRP bars were evaluated according to the ACI 440 Guidelines (2006):

$$\sigma = \frac{M}{jA_f d} = \frac{PL}{4jA_f d} \quad (7.1)$$

where P and L denote the applied load and span length of the slab, respectively, b_w and d refer to the slab width and the effective depth of the slab measured from the compression extreme fiber

of concrete to the centroid of the tension GFRP bars, and A_f represents the cross sectional area of tension GFRP bars. In addition,

$$\begin{aligned}
 j &= 1 - k/3 \\
 k &= \sqrt{2\rho_f n + \rho_f^2 n^2} - \rho_f n \\
 n &= E_f / E_c \\
 E_c &= 0.043 w_c^{1.5} \sqrt{f'_c} \\
 \rho_f &= \frac{A_f}{b_w d}
 \end{aligned} \tag{7.2}$$

where E_f and E_c denote the Young's modulus of GFRP reinforcement and concrete, respectively, ρ_f is the GFRP reinforcement ratio, w_c and f'_c denote the weight and compressive strength of the concrete. The above equations were derived when the tensile strength of concrete was set to zero.

With the calculated bending stress from Eq. 7.1 and the measured strain, the stress-strain curves at various locations of the span were plotted shown in Figures 7.14 through 7.16. Similar observations can be made about the bi-linear behavior as clearly shown in the close-up view of Figure 7.16. As indicated in Figure 7.14, the stress in the tensile GFRP reinforcement increases bi-linearly with strain till failure at approximately 0.01 strain and 62 ksi (428 MPa) bending stress. The strain level measured at failure is approximately 62.5 % of the ultimate strain of the GFRP bars (0.016 in Table 5.1). From the Modulus of Elasticity, the theoretical stress of the tension reinforcement corresponding to 0.01 strain can be estimated to be 59.4 ksi (409 MPa), which is in good agreement with the calculated value from Eq. 7.1. Figure 7.15 compared the strains measured at mid-span and quarter span in longitudinal direction between the two supports as well as at mid-span in transverse direction. Here, SG-01 and SG-03 represent the two longitudinal strain gauges located at mid- and quarter spans, respectively; SG-05 represents the transverse gauge at mid-span. The same bi-linear behavior as seen from the mid-span strain

measurement was observed at the quarter span. The transverse strain at SG-05 was nearly zero so that the slab can be analyzed as one-dimensional beam. That was because the test specimen was a one-way slab and the load was transferred to the slab by the spread beam at mid span over the entire width.

7.3.2 Shear behavior

After the flexural test was over, better half of the tested slab was simply supported with a clear span of 8 ft 6 in. (2.59 m) and re-tested for shear behavior of the slab as shown in Figure 7.17. The shear test was referred to as Load Case 2. Note that the end quarter span of the specimen was not significantly cracked and the middle quarter span was severely cracked during flexural tests in Load Case 1. Also note that the span length of the slab in Load Case 2 is twice as much as the girder spacing in field construction. On each side of the slab, one spring pot was installed at quarter span underneath the hydraulic jack and two DC-LVDT transducers were installed at one-eighth and three-eighth spans, respectively, as detailed in Figure 7.17c.

Unlike the flexural test of the specimen with significant deformation up to 2-3 in. (50.8 to 76.2 mm), the shear test did not exhibit any appreciable deflection even near failure. Such an observation was confirmed by a series of photos in Figures 7.18a through 7.18d that were retrieved from a video clip as the slab approached a sudden failure in shear at approximately 180 kips (800 kN). The diagonal shear crack was not visible till the sudden failure as indicated in Figures 7.18b through 7.18d. The widening of the diagonal shear crack and the formation of splitting cracks along the top and bottom reinforcing bars due to interfacial debonding broke the concrete slab into two pieces in Load Case 2 as detailed in Figures 7.19a and 7.19b. A closer inspection on the failure area as shown in Figures 7.20a and 7.20b indicated that the top GFRP bars were neither fractured nor buckled when the slab suddenly failed. Similarly, the bottom

GFRP bars were confirmed to be not fractured. Figure 7.21 shows an overview of the collapsed slab after the flexural and shear tests. The final residual deflection in Load Case 2 was not obvious during the shear tests, and was later confirmed to be less than 0.2 in. (5.1 mm) at quarter span from the load-deflection curves as shown in Figures 7.22a through 7.22c.

The load-deflection curves at quarter span, one-eighth span and three-eighth span in Figures 7.22a through 7.22c clearly indicated no obvious bilinear behavior as observed during the flexural tests. In other words, during the shear tests in Load Case 2, the slab remained nearly linear till the sudden failure. The difference in flexural and shear behaviors was confirmed by the fact that no additional flexural cracks occurred throughout the shear tests. Even so, the flexural cracks occurred in Load Case 1 may partially lead to no first linear segment in Load Case 2. However, the mechanism for diagonal shear cracks totally differs from that for flexural cracks (Zararis, 2003 and Zakaria et al., 2009). Therefore, the shear failure mode of the slab as indicated in Figure 7.19a was unlikely affected by the existing flexural cracks.

With the obtained material properties from laboratory tests and the ACI 440 Guidelines (2006) for GFRP-bar reinforced concrete, the concrete contribution to the shear capacity is approximated by

$$V_c = \underbrace{\left(\frac{5k}{2}\right)}_{\text{Modified factor}} \underbrace{2\sqrt{f'_c}b_w d}_{\text{normal concrete shear resistance}} \quad (7.3)$$

where k is defined shown in Eq. 7.2. Eq. 7.3 would give 39.5 kips (175.7 kN) shear capacity of the tested slab. This shear capacity corresponded to an applied load of 79 kips (351.4 kN) that is approximately 0.45 times the failure load of the slab, 174 kips (774 kN). The over-conservatism in ACI 440 guidelines may be attributed to the modified factor used in Eq. 7.3 that can dramatically reduce the concrete contribution to the shear capacity of GFRP-bars reinforced

concrete. Similar conclusions have been drawn by Nystrom et al. (2002) where GFRP-bar reinforced beams had a 3.83 times higher shear capacity than those predicted by the ACI 440 Guidelines.

The load-strain curve at quarter span is presented at Figure 7.23. The reloading and unloading curves in Figure 7.23 almost overlapped to each other with nearly zero residual deformation. Such a behavior further confirmed that, unlike the flexural tests that resulted in significant residual deformation due to GFRP bar debonding from the concrete, the shear tests did not cause any GFRP bar slippage and thus the arch effect remained to be the main force transfer mechanism throughout the shear tests even though the strain in GFRP bars reached to 0.007 or a similar strain level achieved during the flexural tests.

7.4 Field test program

The main objectives for the field testing of the newly erected bridge were to determine the load distribution among various girders (in particular exterior versus interior girders), determine the load distribution within each deck slab, and examine the overall performance of the bridge based on the in-situ testing of the bridge.

7.4.1 Instrumentation Plan

The general instrumentation plan was included in Chapter 4 for 192 embedded strain gauges in precast bridge elements and Chapter 6 for DC-LVDT transducers, inclinometers and accelerometers. The representative installation processes of DC-LVDT transducers, inclinometers, and accelerometers underneath the deck slabs and box girders are illustrated in Figures 7.24 through 7.26, respectively.

As previously mentioned in Chapter 6, twenty DC-LVDT transducers as shown in Figures 6.14 and 7.24 were located underneath the bridge decks to monitor vertical deflection of the bridge deck and girders as truck(s) passed through the bridge. Due to limited vertical clearance for DC-LVDT stands below the concrete girder bridge span, angles were mounted on the side of concrete girders as supports for DC-LVDT transducers to monitor the vertical deflection of each girder at various longitudinal positions of interest. In addition, six inclinometers and seven accelerometers were installed on each span as shown in Figures 7.25 and 7.26, respectively.

7.4.2 Load protocols for field testing

The test matrix for various truck passes and positions as schematically illustrated in Figures 6.6 through 6.13 was given in Table 6.2. A total of twenty-one load cases were performed including both static and dynamic tests with each span. The test results and discussion were presented below.

7.5 Field test results and discussion

7.5.1 Longitudinal distribution of vertical deflections

The distribution of vertical deflections along the longitudinal direction (traffic flow) from various truck stops and passes is presented in Figures 7.27 and 7.28 for the north exterior and the center steel girders, respectively. All the deflection curves appeared very smooth. Among all six load groups, Stop 3 induced the maximum deflection as expected from Fig. 6.4. Stop 1 and Stop 4 represented the truck(s) located near both ends of the bridge so that both stops attributed to little deflections but such information was invaluable for the evaluation of the maximum shear. A comparison of all static responses at the exterior girder demonstrated that Pass 1 was the

worse-case loading scenario. For Pass 1, the truck passed on top of the exterior girder and induced the maximum deflection along the exterior girder. The same trend was observed in those deflection curves. It can also be observed from Figures 7.27a through 7.27d that, as the truck moved from Pass 1 to Pass 3, the maximum deflection of the bridge decreased due to the engagement of more supporting girders. For example, the maximum deflection of the bridge obtained during Pass 3 is only 31% of that during Pass 1. Obviously, Pass 4 with two trucks caused the largest deflection of all passes as indicated in Figure 7.27d.

The distribution of vertical deflections along the center girder is presented in Figures 7.28a through 7.28d. Like the exterior girder, the center girder experienced the maximum deflection in all load cases when a truck parked at Stop 3. Unlike the exterior girder, however, as the truck moved from Pass 1 to Pass 3, the maximum deflection of the bridge increased since more loads were supported by the center girder. A closer look at the deflection curves revealed that the maximum deflection of the center girder during Pass 3 was approximately 132% of that during Pass 1. Again, Pass 4 with two trucks induced the largest deflection of all passes as indicated in Figure 7.28d.

7.5.2 Transverse distribution of vertical deflections

The distribution of vertical deflections among various steel girders at mid-span is presented in Figures 7.29a through 7.29d. As the truck moved from Pass 1 to Pass 3, the transverse distribution of the mid-span deflections changed from a linear in Pass 1 to a symmetric parabolic curve in Pass 3, which indicated that the symmetric behavior of the bridge under a symmetric load about the bridge centerline has been preserved. In comparison with Figure 7.29a for Pass 1 with one truck, Figure 7.29d indicated that the deflection for Pass 4 with two trucks is approximately equal to a summation of the deflection in Figure 7.29a and its

mirror-image about the center girder. This linear relation verified the integrity of the new steel-girder span.

The maximum mid-span deflection of the bridge reached up to 0.083 in. (2.1 mm) when two parallel trucks (about 88 kips for Pass 4) parked at mid-span (Stop 3). The measured deflection is only 18% of the maximum allowable deflection specified by ACI 318 and AASHTO (2008), which is equal to $L/800 = 0.405$ in. (10.3 mm). Therefore, the bridge design was very conservative in terms of the stiffness requirement.

7.5.3 Dynamic deflection and impact factor for live load

One point of interest was the live load impact factor due to the dynamic effect of vehicles on the bridge response. Figures 7.30a and 7.30b showed the representative deflection time histories at mid-span for Load Group 4 with one truck and Load Group 6 with two trucks passing through the bridge at certain predetermined speed, respectively. Obviously, more fluctuations are observed in the deflection time history at higher speed due to more significant dynamic effects. The impact factor for the live load was investigated by comparing the test data due to similar truck passes at a speed of zero (static deflection), approximately 15 mph (24 kph) with two parallel trucks in Pass 4, and approximately 35 mph (56 kph) with one truck in Pass 1. The live load impact factor (IF) was evaluated as the ratio of the dynamic deflection obtained at 35 mph (56 kph) and 15 mph (24 kph) to the static deflection obtained from Stop 1 to Stop 4. Considering the fact that the truck may not accurately follow Pass 1 or Pass 4, the static deflections obtained during Pass 1 and Pass 2 were both used as references.

Figures 7.31a and 7.31b compared the static and dynamic deflection envelopes of the north exterior steel girder for one truck at 35 mph (56 kph) and two trucks at 15 mph (24 kph), respectively. Similarly, Figures 7.31c and 7.31d compared the static and dynamic deflection

envelopes of the center steel girder at the two speeds, respectively. Figures 7.31e and 7.31f compared the mid-span static and dynamic deflection envelopes at the two speeds. Note that Figures 7.31a to 7.31f includes three runs with one truck and two runs with two trucks. Due to the risk involved in driving two trucks on the narrow roadway, decision was made to take two data points to show repeatability of the test data. A comparison of dynamic response of the exterior girder to that in static cases in Figs. 7.31a and 7.31d showed that dynamic deflection regardless of one or two trucks at each point of interest was slightly higher than those under statics. Out of 110 cases, 57 cases gave positive impact factors as depicted in Fig. 7.31g. The positive impact factors were used to obtain an average live load impact factor of 0.16 based on curve fitting. Compared to the empirical AASHTO live load impact factor for the bridges of 0.33, the AASHTO guidelines appear to be conservative. The impact factor that was nearly zero indicated that the deflections are nearly identical to the deflections while the impact factor that was higher than zero in Fig. 7.31e was mainly because it was the most safe-case to account for when truck(s) follow Pass 1.

7.6 Summary

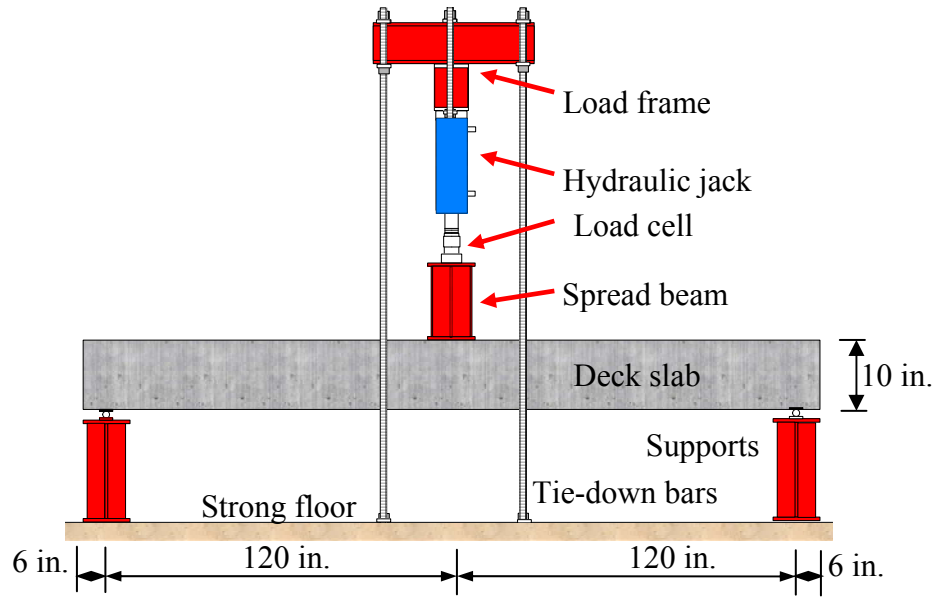
In this chapter, the structural behavior of a full-size GFRP-bar reinforced concrete slab was investigated with laboratory tests to failure and the field performance of a simply-supported bridge with three precast GFRP reinforced concrete slabs supported on five steel girders was investigated with in-situ testing under design truck loads. Based on the experimental results and analyses, the bridge design with GFRP-bar reinforced concrete slabs was demonstrated to be satisfactory in terms of both strength and deflection requirements.

The full-size concrete slab was simply-supported with 20 ft (6.10 m) span length and tested to a flexural failure. The flexural behavior can be described by a bi-linear stress-strain

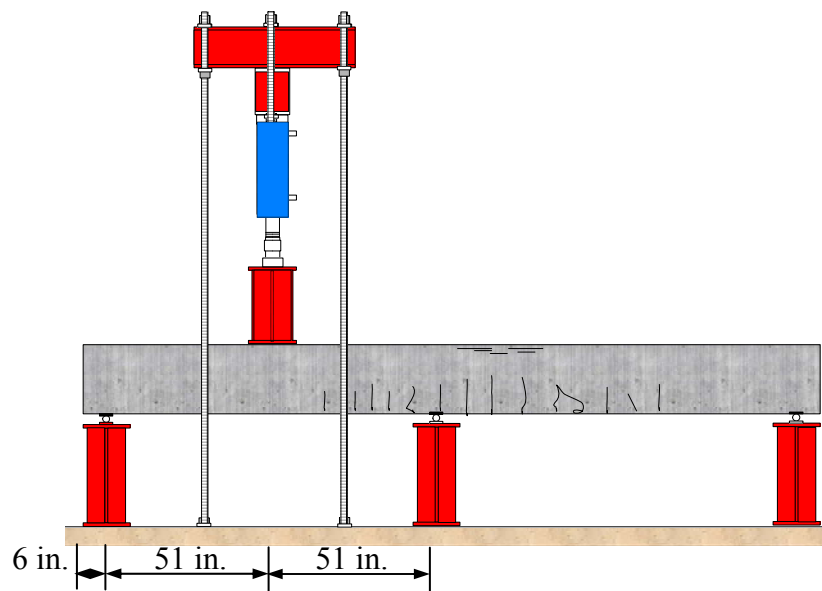
curve with the stiffness of the cracked section reduced by approximately 2/3 from that of the uncracked section. The flexural failure of the slab resulted from the concrete crushing as expected and occurred at approximately 0.01 strain and 62 ksi (428 MPa) bending stress, leaving approximately 3 in. (76.2 mm) residual deformation after unloading. The excessive deformation of the properly-designed GFRP reinforced bridge deck may serve as a “warning” sign of a potential bridge failure. At failure of the GFRP-bar reinforced concrete slab, the strain in GFRP bars was approximately 62.5% of the manufacturer-specified ultimate strain.

The full-size concrete slab was then simply-supported with 8.5 ft (2.59 m) span length and re-tested to a shear failure. The shear behavior of the slab can be described by a linear stress-strain curve with shear capacity 2.2 times as much as the ACI 440 Guidelines predicted. The residual deflection due to the shear failure was less than 0.2 in. (5.1 mm). The load capacity of the tested slab in shear failure was approximately 180 kips (800 kN). This level of load capacity (concentrated at one point) substantially exceeded the maximum load effect that two fully-loaded HS20 trucks can possibly induce on the simply-supported bridge with a clear span length of 25 ft. (7.62 m). Consider the 4.25 ft (1.30 m) spacing of steel girders that support the concrete slab. The total load of two real wheels of a HS20 truck that can fit into the girder spacing is only 64 kips (285 kN).

In-situ bridge load testing conducted on the newly erected bridge demonstrated that the bridge behaved in the elastic range under design truck loads. The measured bridge deflection was only 18% of the allowable deflection, indicating that the bridge is sufficiently stiff. Based on the 57 live load test cases, the average live load impact factor was 0.16, which is significantly smaller than that given in the AASHTO Specifications (2010).



(a) Schematic test setup for Load Case 1 with a predicted flexural failure (elevation view)



(b) Schematic test setup for Load Case 2 with a predicted shear failure (elevation view)

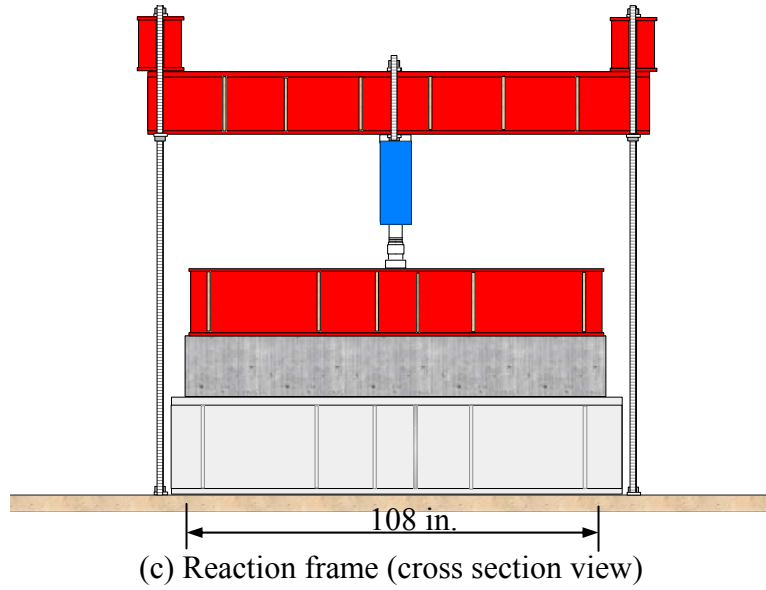


Figure 7.1: Laboratory test schemes for a full-size concrete slab



(a) Reaction frame (detail)

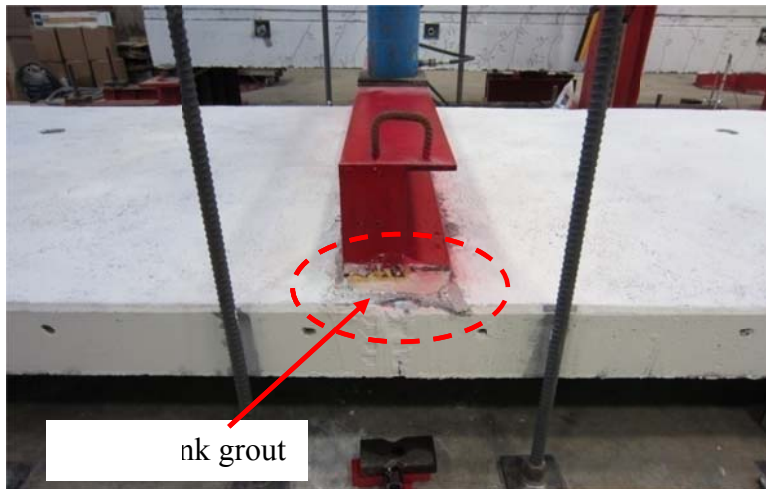


(b) Cross sectional view of the specimen and loading system

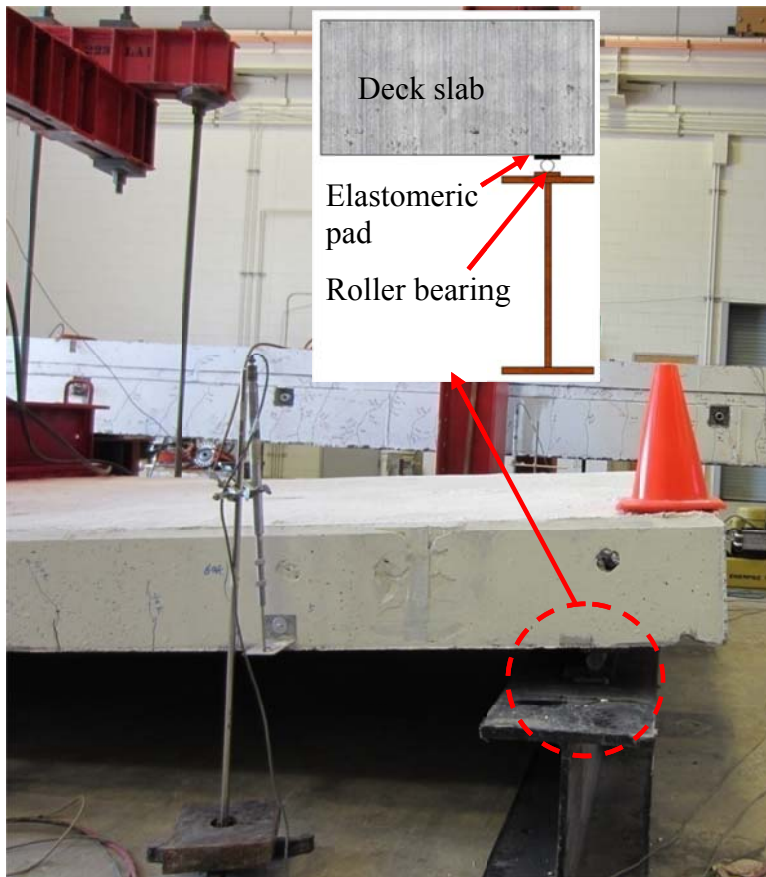


(c) Overview of the loading system

Figure 7.2: Photos of the laboratory setup for concrete slab testing



(a) Attachment of spread beam to the concrete slab



(b) End support of the concrete slab

Figure 7.3: Details of slab test setup

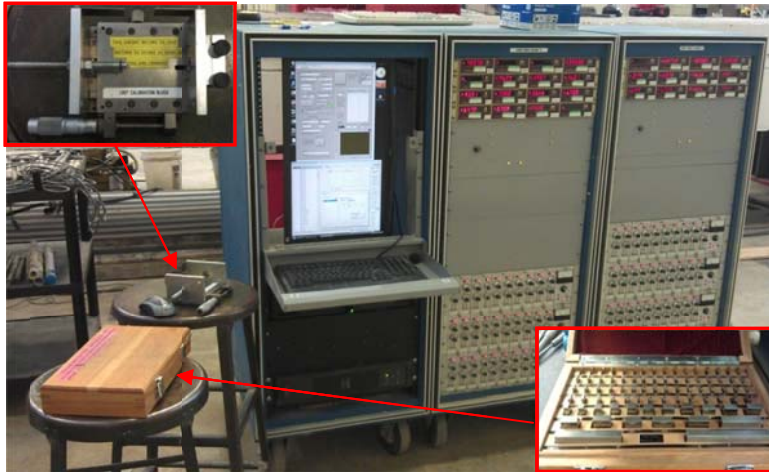


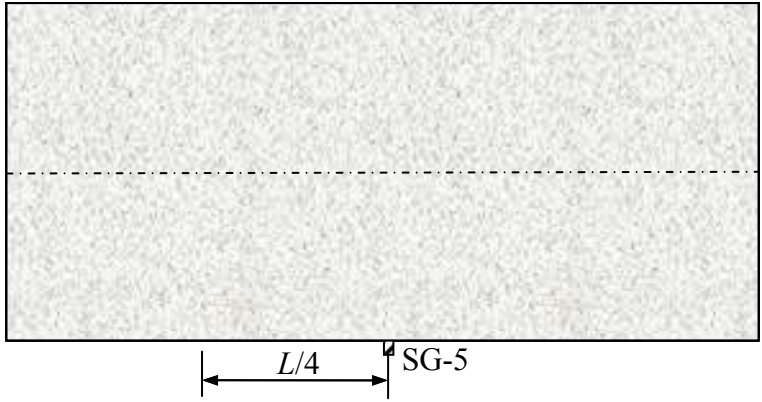
Figure 7.4: Data acquisition and calibration devices



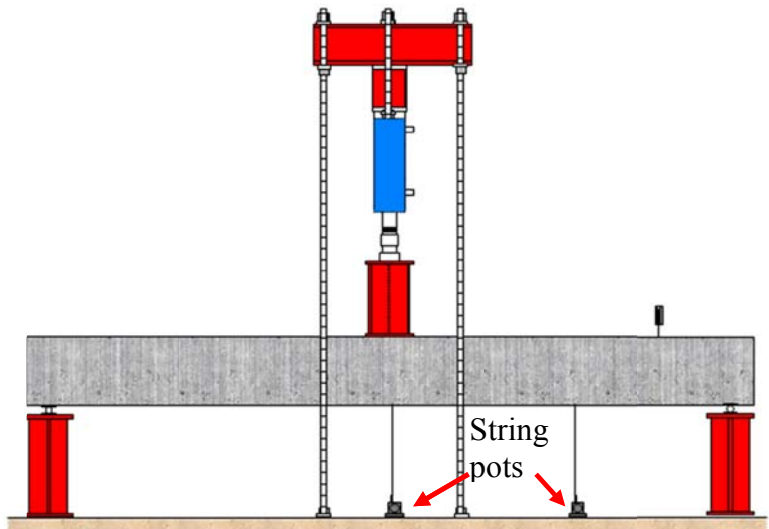
Figure 7.5: DC-LVDTs for box girder tests



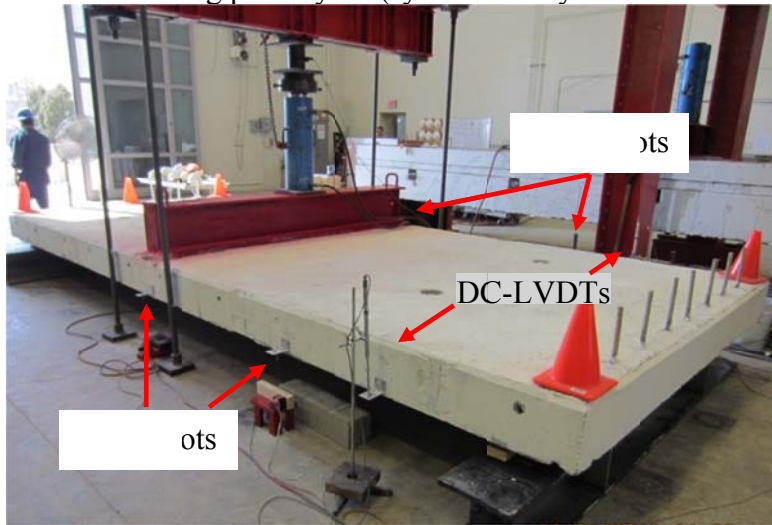
Figure 7.6: Calibration of a DC-LVDT with calibration block



(a) Strain gauges layout (plan view)



(b) DC-LVDTs and string pots layout (symmetrically distributed at two sides)



(c) Overview of sensor layout

Figure 7.7: Instrumentation layout for Load Case 1

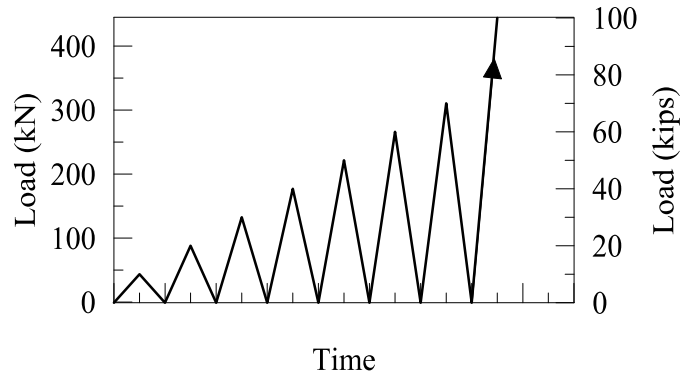


Figure 7.8: Load protocol for flexural tests (Load Case 1)

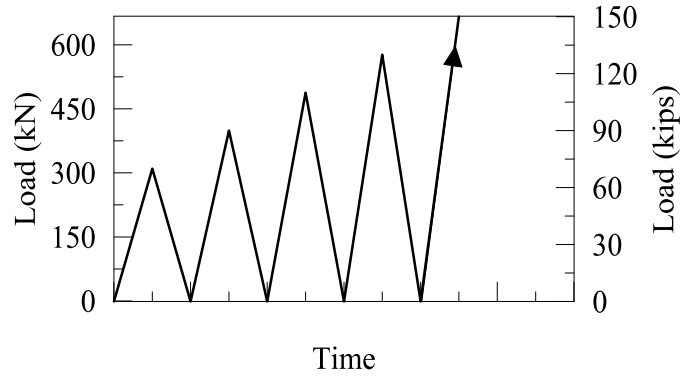


Figure 7.9: Load protocol for shear tests (Load Case 2)



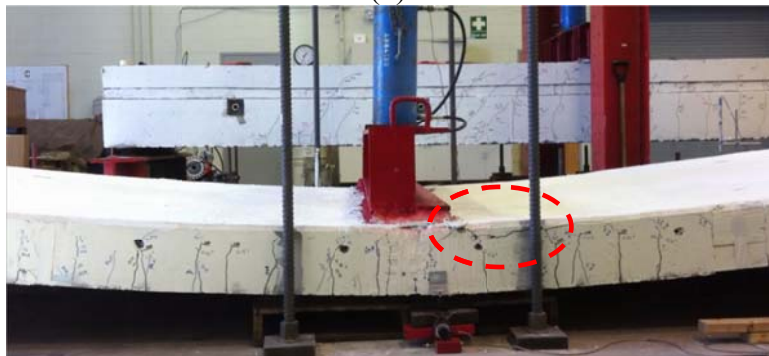
Figure 7.10: Crack pattern during the slab test with initial cracks observed at 10 kips



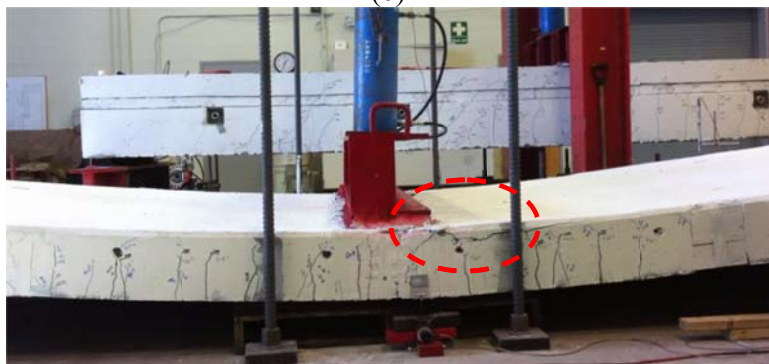
(a)



(b)

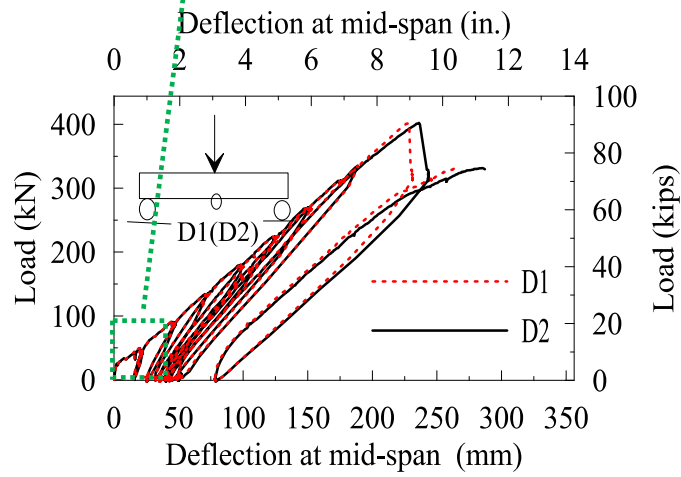
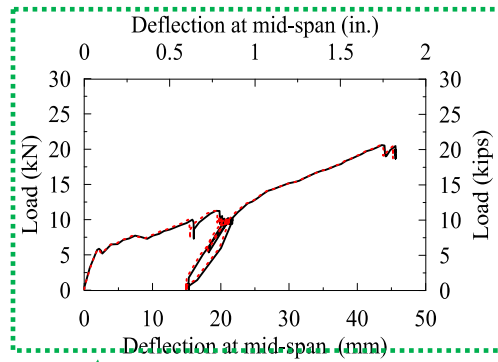


(c)

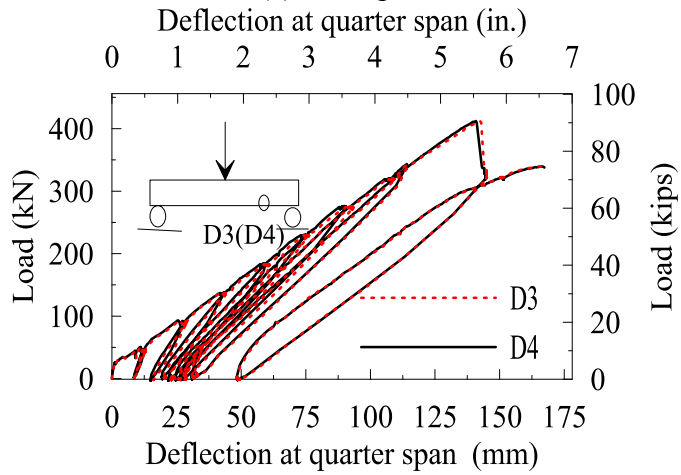


(d)

Figure 7.11: Flexural failure process



(a) Mid-span



(b) Quarter span

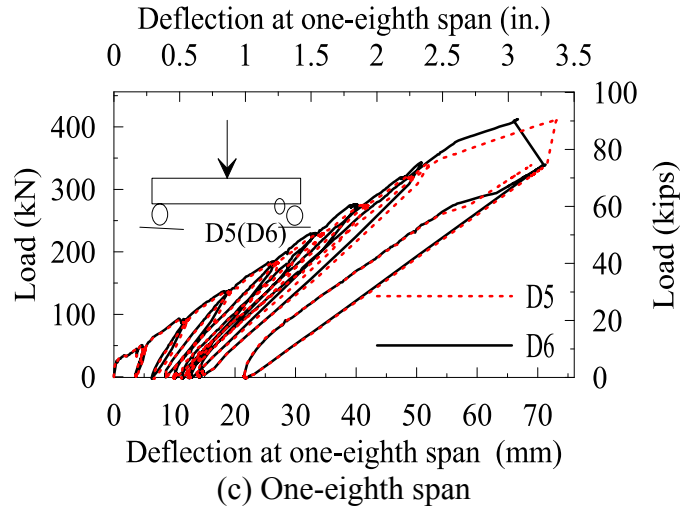


Figure 7.13: Load-deflection curves at various locations

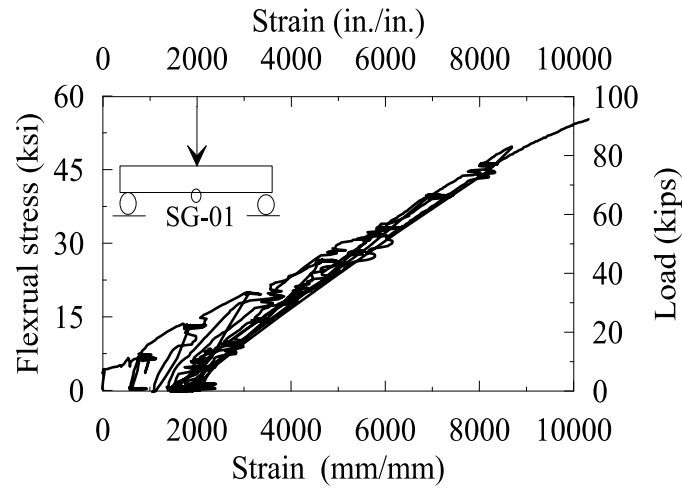


Figure 7.14: Stress-strain curve at mid-span bottom GFRP bar

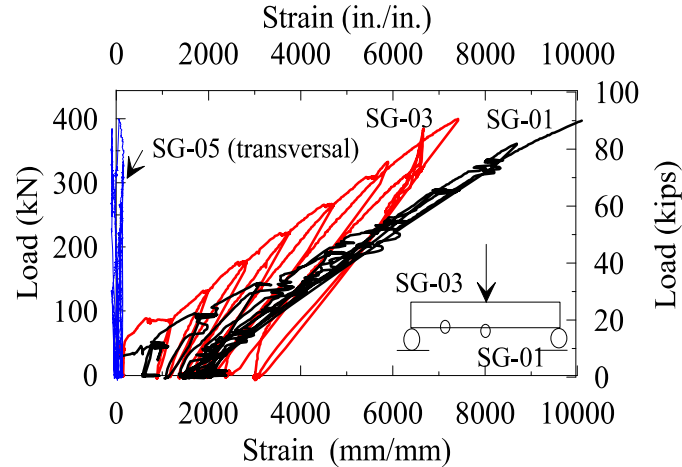


Figure 7.15: Load-strain curves of GFRP bars at various locations

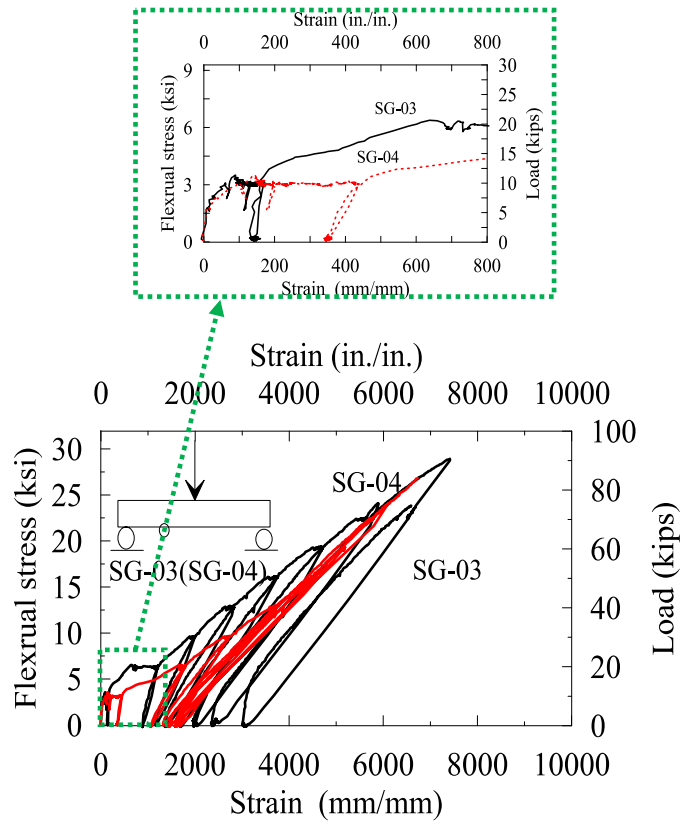
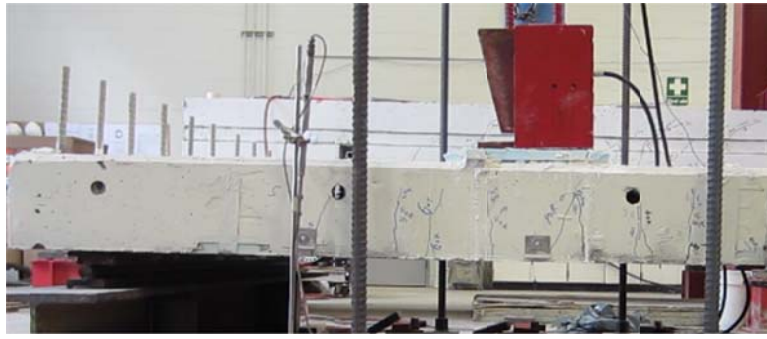


Figure 7.16: Stress-strain curves for quarter span bottom GFRP bar (Load Case 1)



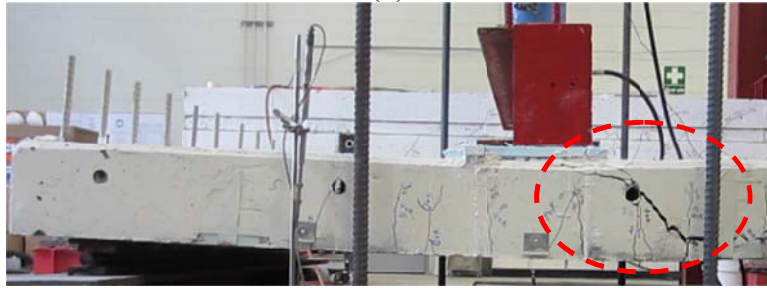
Figure 7.17: Setup for shear test in Load Case 2



(a)



(b)

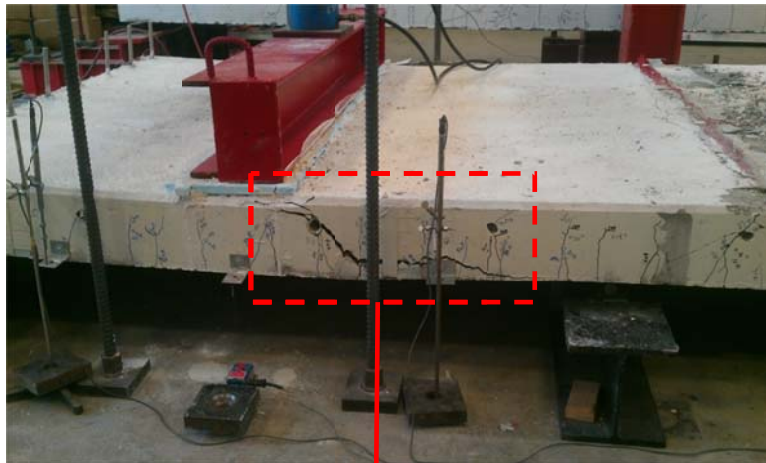


(c)



(d)

Figure 7.18: Shear failure process and cracking propagation



a)



(b)

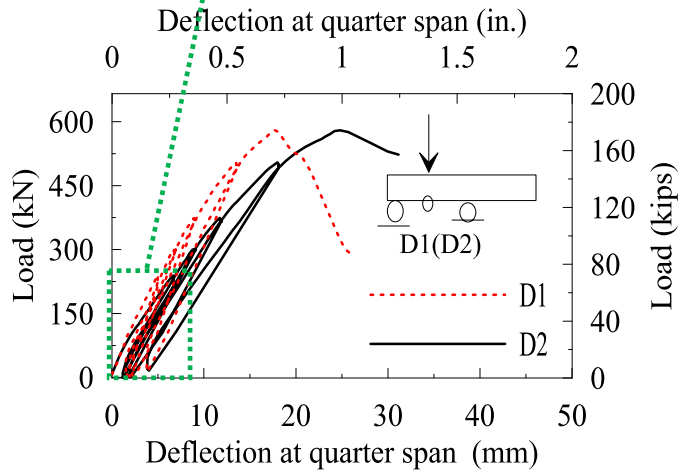
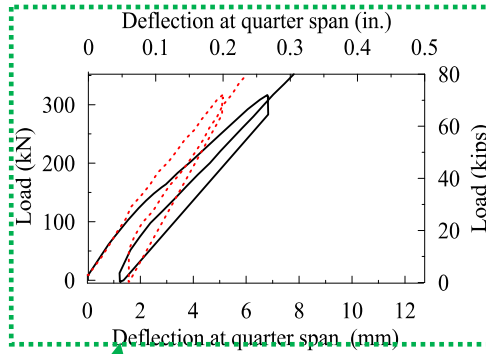
Figure 7.19: Slab failure by shear



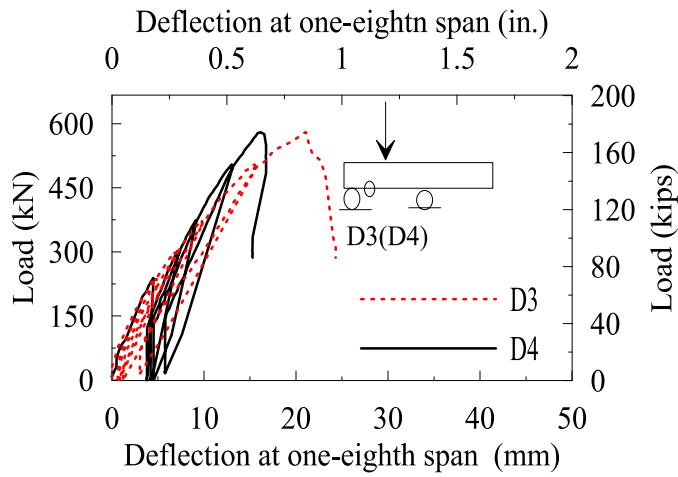
Figure 7.20: GFRP bar condition at shear failure



Figure 7.21: Overview of the collapsed slab after two load cases



(a) Quarter span



(b) One-eighth span

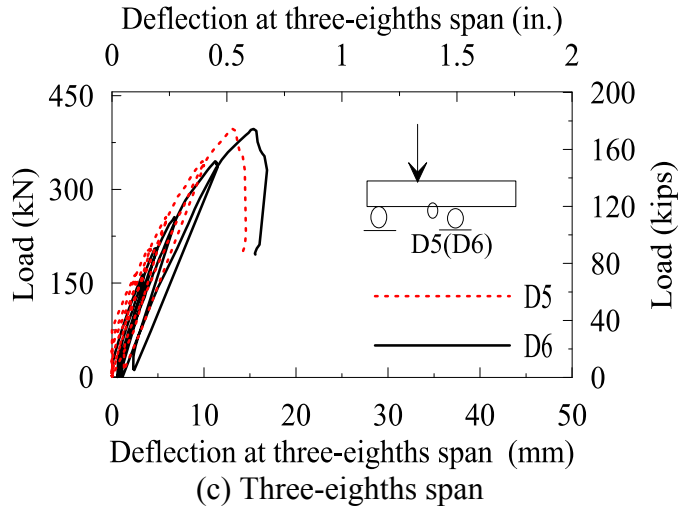


Figure 7.22: Load-deflection curves at various locations

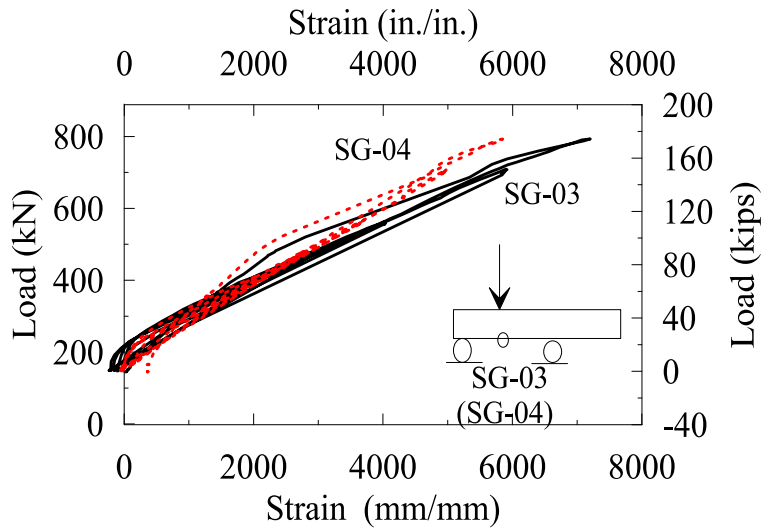


Figure 7.23: Load-strain curves for quarter span GFRP bar (Load Case 2)



(a) Steel-girder span (20 DC-LVDTs)



(b) Box-girder span (20 DC-LVDTs)



(c) Concrete-girder span (20 DC-LVDTs)

Figure 7.24: DC-LVDTs layout on each span in field test



(a) Steel-girder span (6 inclinometers)



(b) Box-girder span (6 inclinometers)



(c) Concrete-girder span (6 inclinometers)

Figure 7.25: Inclinometer layout on each span in field tests



(a) Steel-girder span (7 accelerometers)

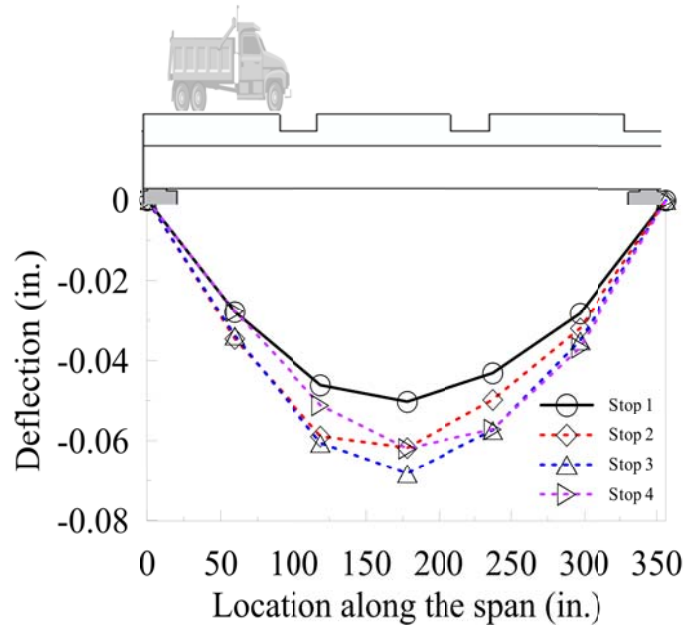


(b) Box girder span (7 accelerometers)

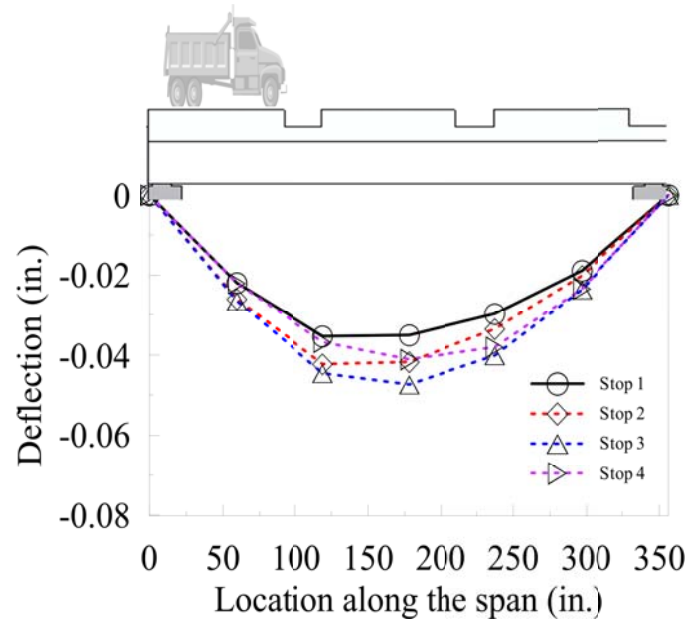


(c) Concrete-girder span (7 accelerometers)

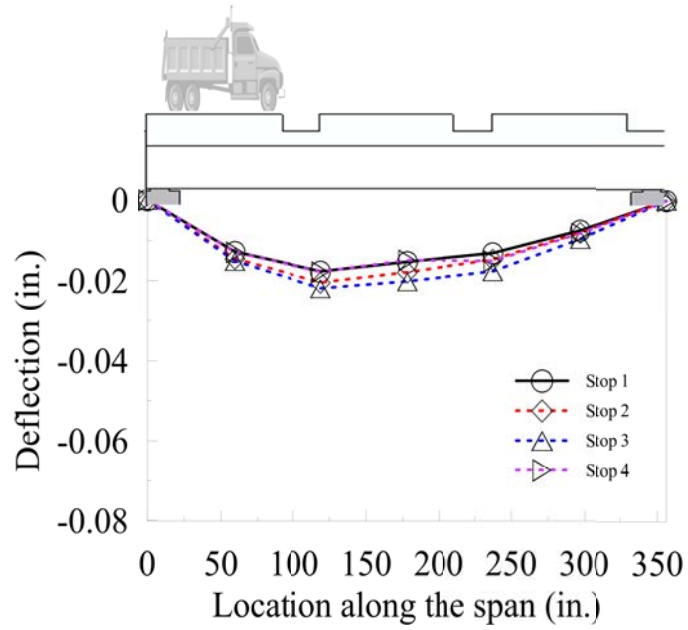
Figure 7.26: Accelerometer layout on each span in field tests



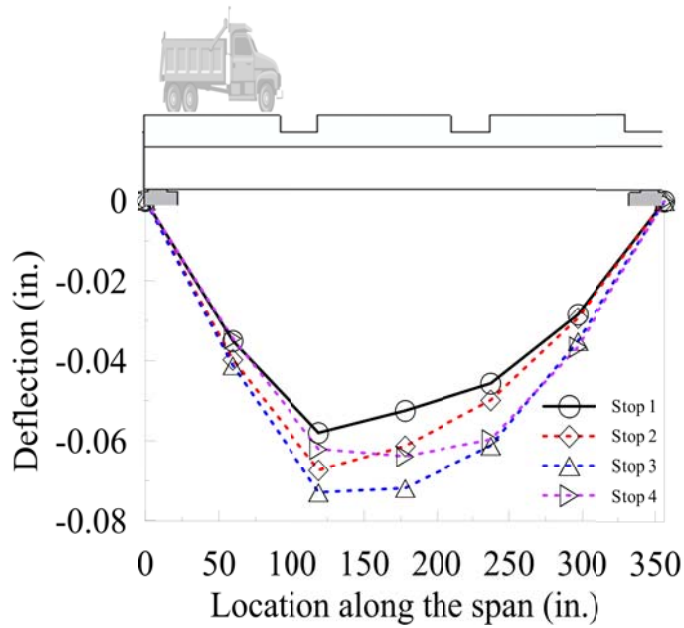
(a) SSLC 11-14 (Load group 1: Pass 1)



(b) SSLC 21-24, SDLC 41 and DDLC 61 (Load group 2, 4, and 6: Pass 2)

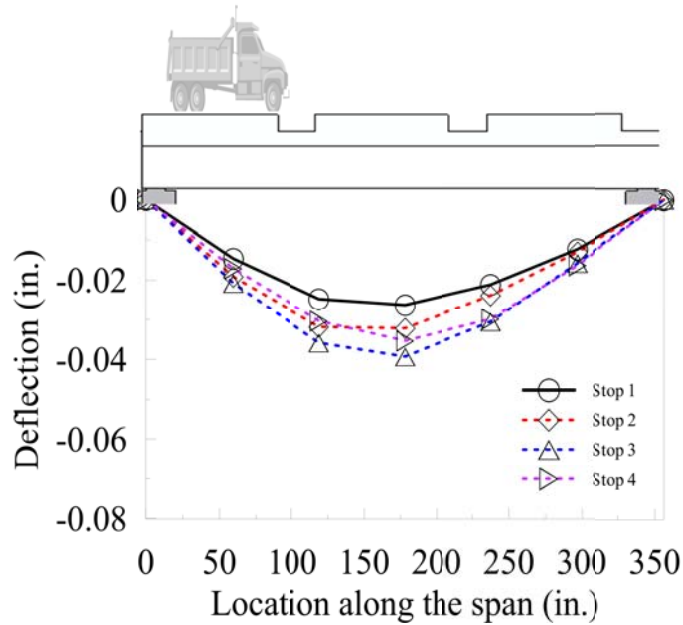


(c) SSLC 31-34 (Load group 3: Pass 3)

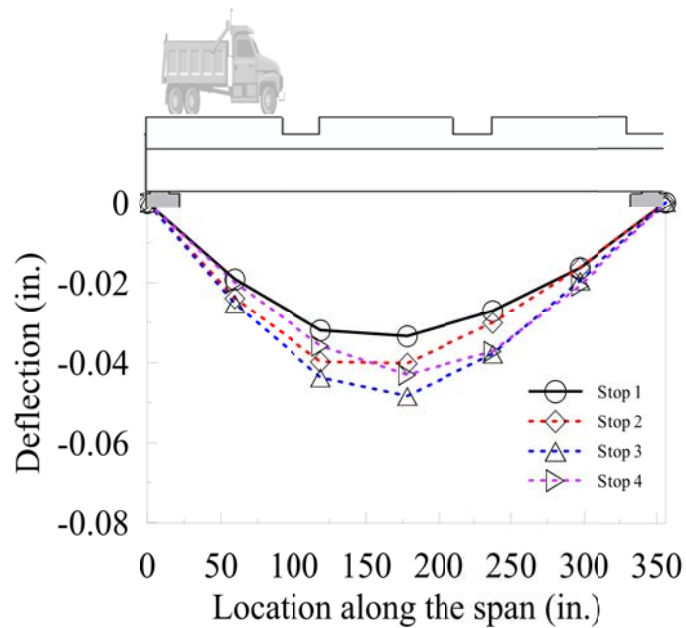


(d) DSLC 51-54 (Load group 5: Pass 4)

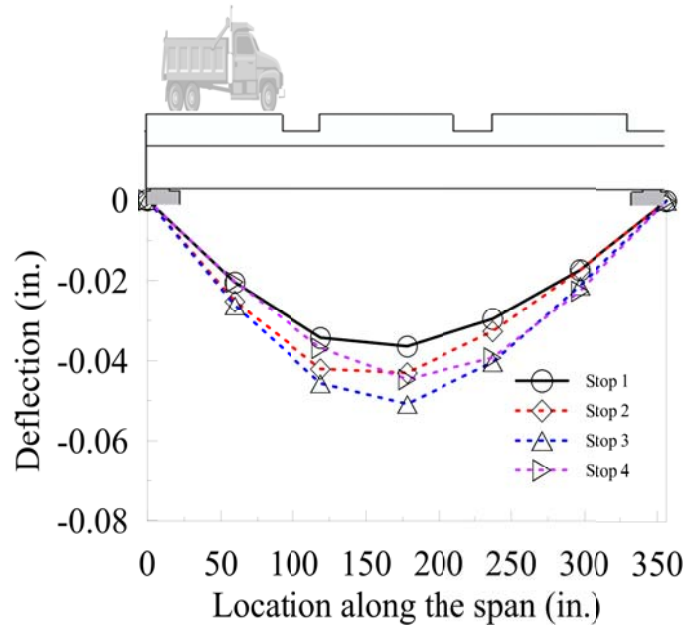
Figure 7.27: Deflection distribution along north exterior steel girder under various load cases



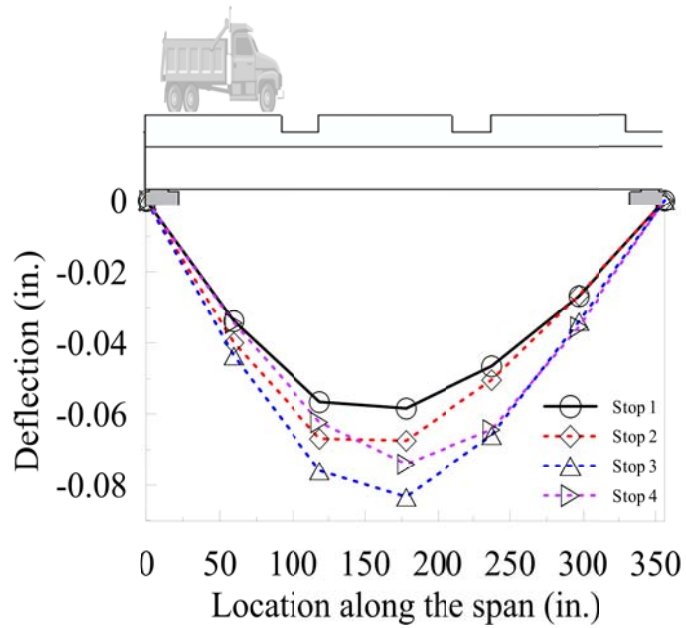
(a) SSLC 11-14 (Load group 1: Pass 1)



(b) SSLC 21-24 (Load group 2: Pass 2)

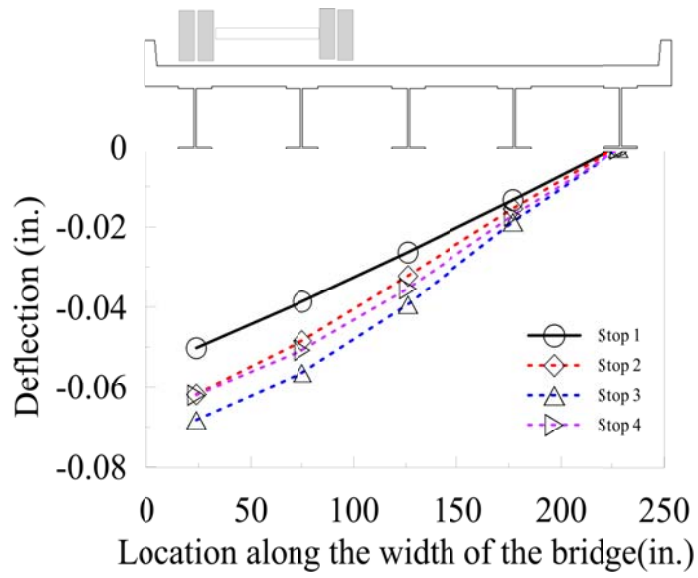


(c) SSLC 31-34 (Load group 3: Pass 3)

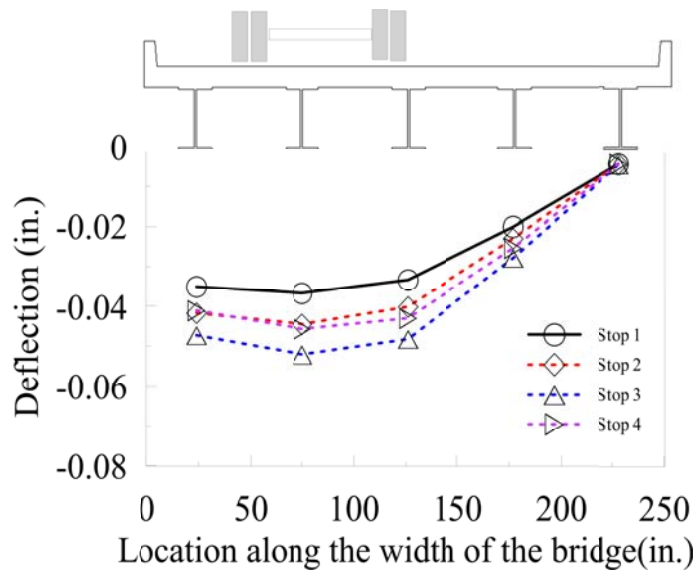


(d) DSLC 51-54 (Load group 5: Pass 4)

Figure 7.28: Deflection distribution along center steel girder under various load cases



(a) SSLC 11-14 (Load group 1: Pass 1)



(b) SSLC 21-24 (Load group 2: Pass 2)

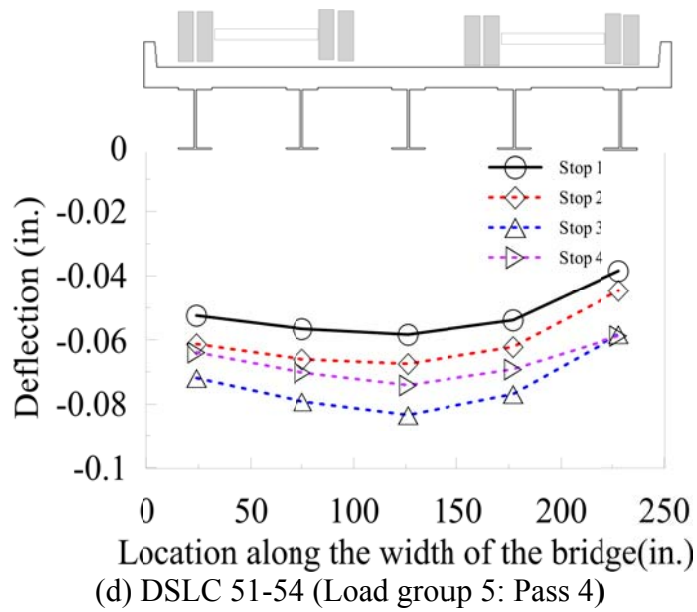
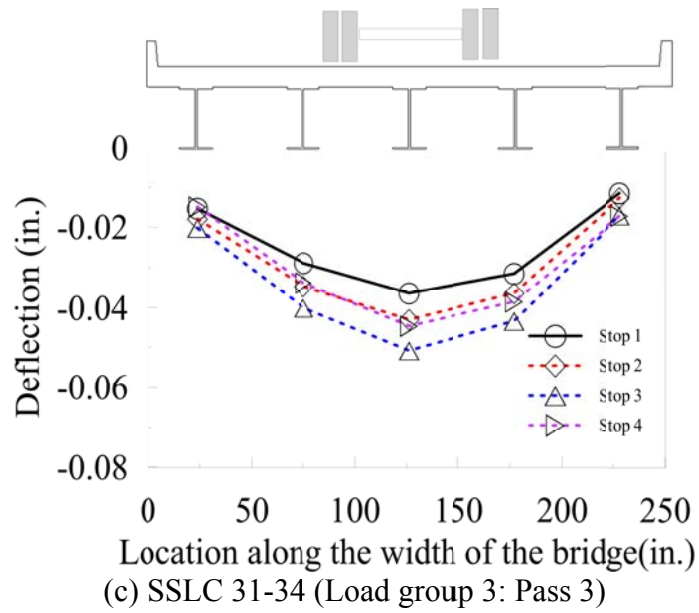
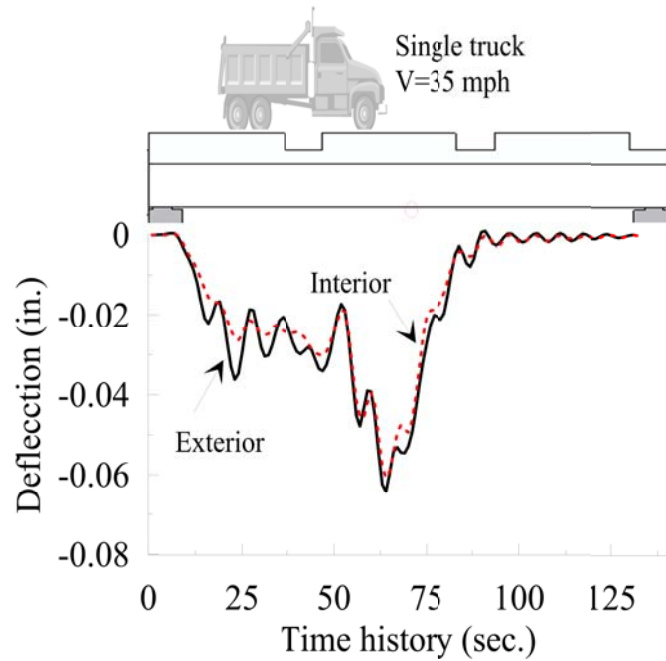
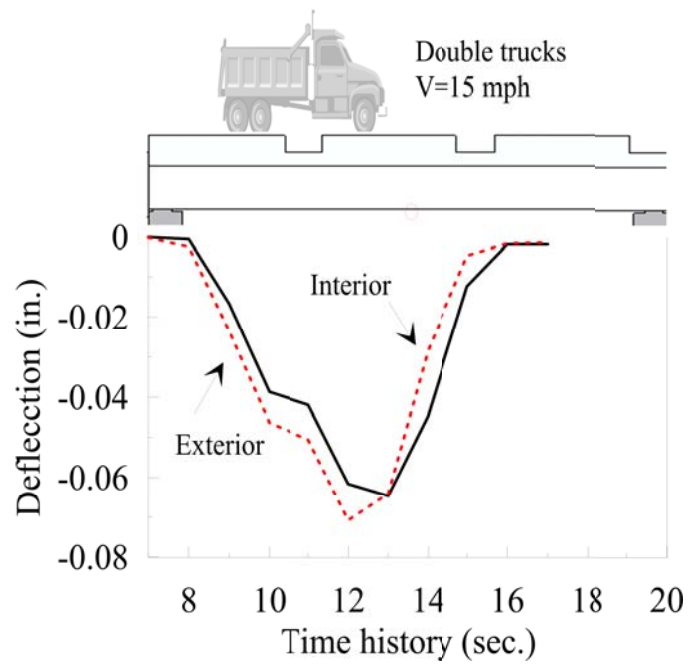


Figure 7.29: Transverse distribution of deflections of the steel-girder span under various load cases

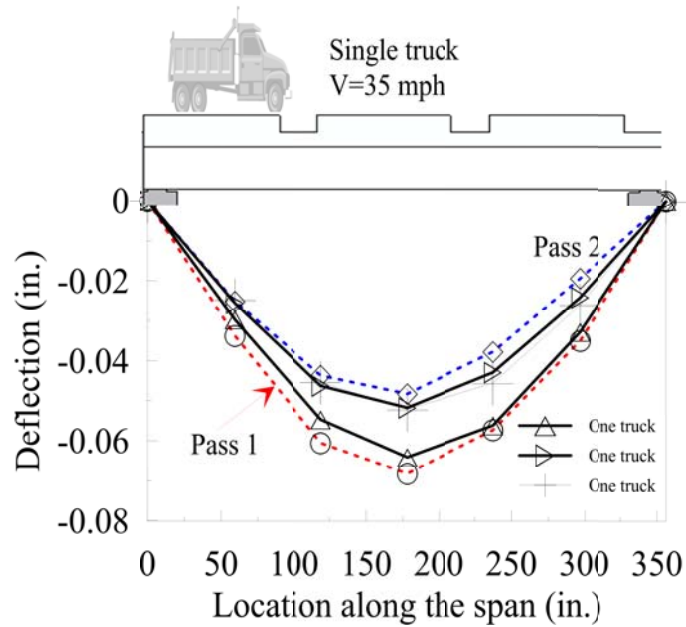


(a) SDLC 41 (Load group 4: Pass 2 with one truck)

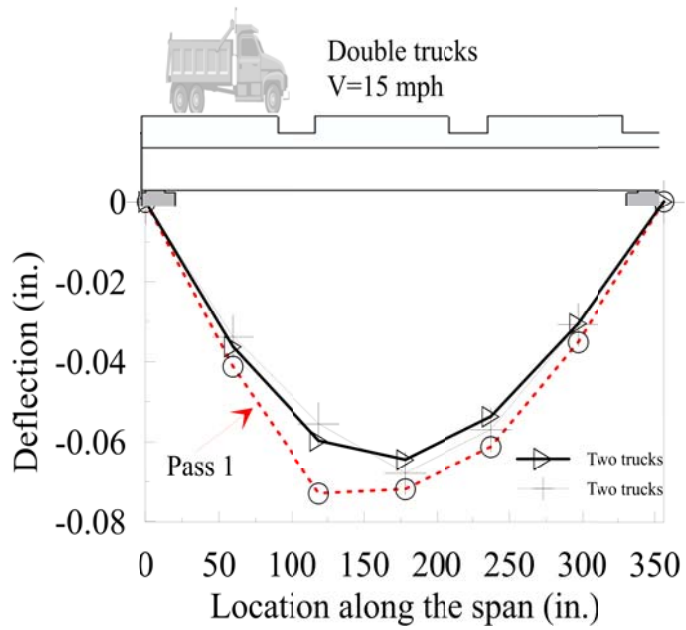


(b) DDLC 61 (Load group 6: Pass 4 with two trucks)

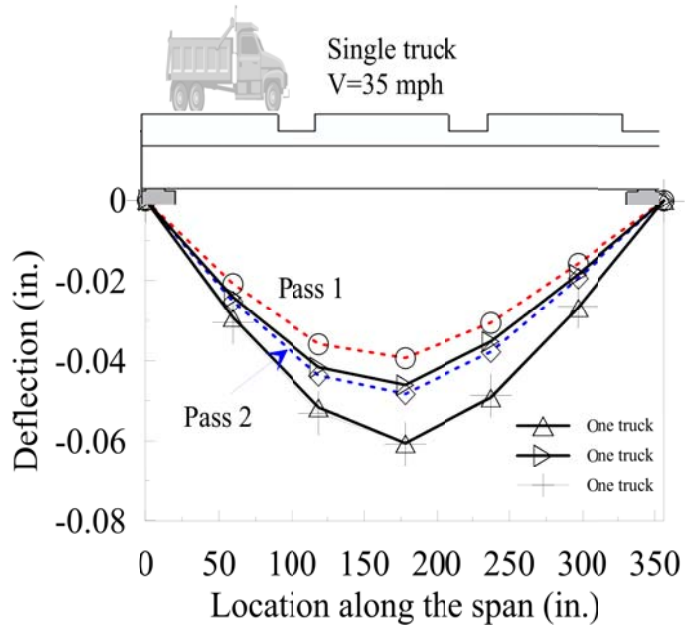
Figure 7.30: Mid-span deflection time history



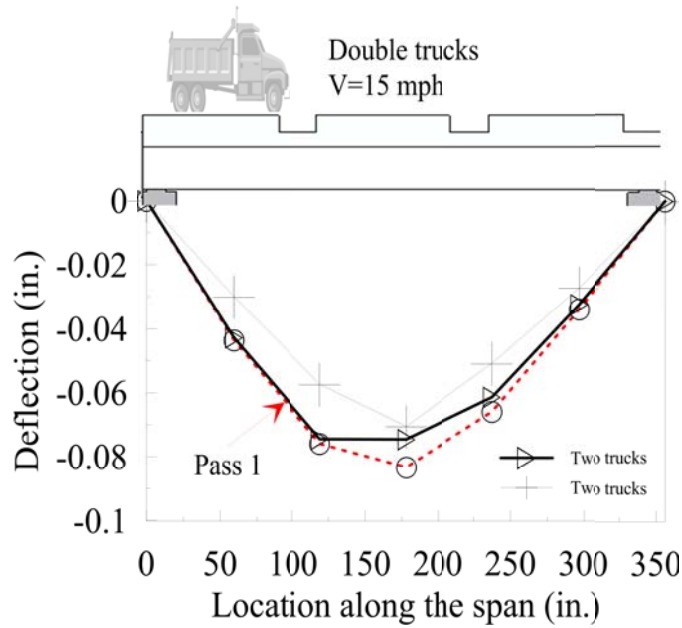
(a) Dynamic deflection at the exterior girder due to one truck live load



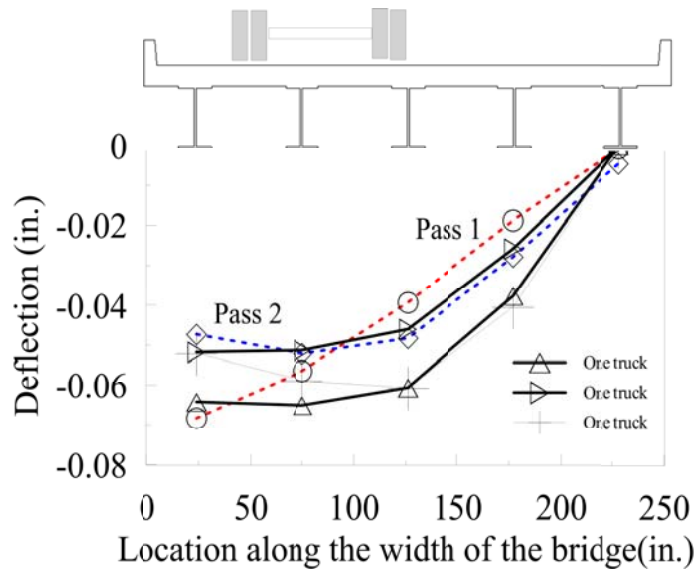
(b) Dynamic deflection at the exterior girder due to two trucks live load



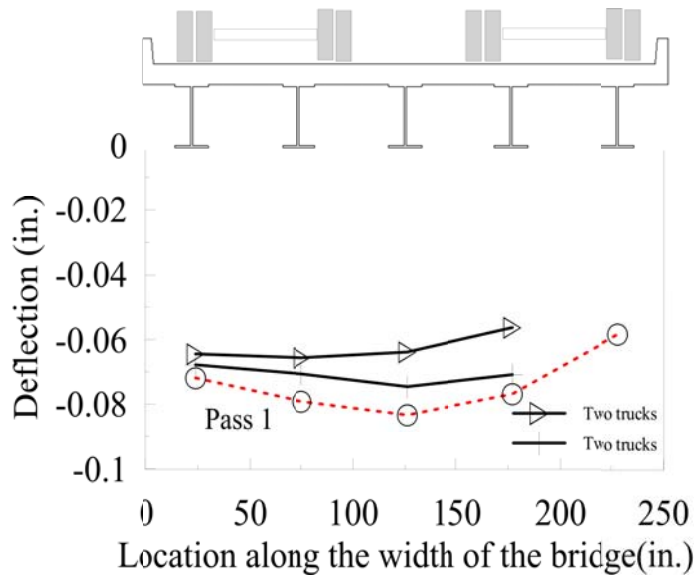
(c) Dynamic deflection at the center girder due to one truck live load



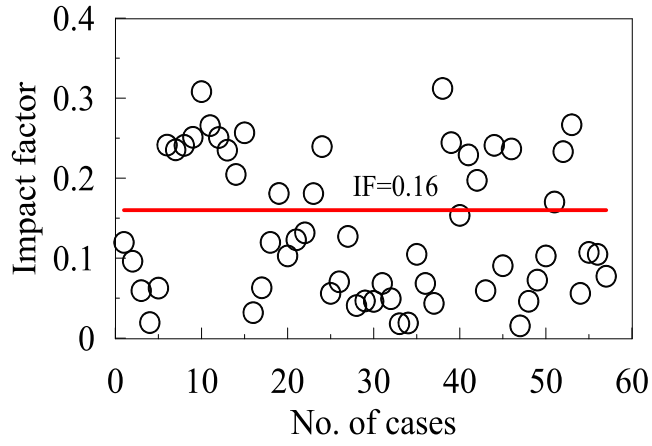
(d) Dynamic deflection at the center girder due to two trucks live load



(e) Dynamic deflection at the mid-span due to one truck live load



(f) Dynamic deflection at the mid-span due to two trucks live load



(g) Impact factor for live load

Figure 7.31: Dynamic effects and impact factor for live load due to truck(s)

Chapter 8. Performance of GFRP-bar Reinforced Box Girders

8.1 Introduction

In this chapter, the behavior and performance of GFRP-bar reinforced box girders are investigated with laboratory and field tests. The box girders represent one type of infrequent applications of GFRP bars in concrete structures. The laboratory test to failure and the field test in service condition provided a unique opportunity to study the behavior of box girders from operation to failure conditions. In addition, the experimental results obtained can validate the design of box girders. Specifically, this chapter provides the detailed instrumentation layout, test setups, test results and discussion of box girders.

8.2 Laboratory test program

8.2.1 Test schemes

In Chapter 7, both flexural and shear failure modes of a GFRP-bar reinforced concrete slab was investigated with two sets of tests where the slab was loaded at middle point of a long span and quarter point of a short span, respectively. The flexural and shear tests were conducted since the slab was actually supported on five girders in field construction and the girder spacing is sufficiently short to warrant a potential shear failure.

The GFRP-bar reinforced concrete box girder was simply supported on two intermediate wall piers in field construction as discussed in Chapter 3. The length-to-height aspect ratio of each box girder is $27/2.17 = 12.4$. Therefore, the overall (global) behavior of the box girder is typically governed by flexural behavior if the girder had a solid cross section. Due to its hollow section, the girder likely involves a mixed flexural and shear behavior. In addition, local shear

failure may potentially occur near the simple supports under a heavy wheel load. However, to simulate the local shear failure of a full-size box girder requires a significant loading capacity since the box girder is deep and reinforced with GFRP stirrups. The theoretical shear capacity of the girder was estimated to be over 400 kips (1779 kN), which requires a load of over 800 kips (3558 kN) in a three-point loading setup and thus exceeds the allowable reaction capacity of the strong floor in the structures laboratory. Therefore, the box girder was tested for global behavior as it were in field applications. Figures 8.1a and 8.1b show the elevation and end views of the schematic test setup of the full-size box girder.

The laboratory test specimen was representative to the box girders designed and constructed for the Washington County Bridge as discussed in Chapters 3 and 5. The specimen was 27 ft (8.2 m) long, 5 ft 3 in. (1.6 m) wide, and 26 in (0.66 m) deep. As indicated in Figures 8.1a and 8.1b, the box girder was simply supported with a span length of 25 ft (7.62 m) and loaded by a load at mid-span.

8.2.2 Test setups

The photos in Figures 8.2a and 8.2b showed the actual test setup of the box girder, including the loading frame and hydraulic jack. The specimen was simply supported on two I-shaped stiffened steel beams that were laterally restrained by two anchored-down small beams to prevent potential instability during the tests. At mid-span of the box girder, a spread beam was firmly attached to the top concrete surface for a uniform distribution of the load applied by a hydraulic jack by reacting against a stiff reaction frame. The reaction frame consisted of a double channel cross beam and two wide flange supporting columns that are placed on two sides of the specimen and both anchored to the strong floor. A 500-kip (2224-kN) hydraulic jack (Model

AN10137) as shown in Figures 8.2a and 8.2b was used in series with a load cell for load measurement.

No-shrink grout and polystyrene as illustrated in Figure 8.3a were used between the spread beam and the concrete surface of the box girder to achieve a uniform distribution of the applied load. Like the concrete slab tests discussed in Chapter 7, a 2-in. diameter bearing rod was placed between the I-shaped beam support and the box girder to allow free movement and rotation of the box girder. In addition, a 2 in. (50 mm) wide and 0.5 in. (12.7 mm) thick elastomeric pad was placed between the concrete and the top steel plate of the roller support as shown in Figure 8.3b to allow the girder to rotate freely without crushing concrete due to stress concentration.

8.2.3 Instrumentation plan

The box girder was instrumented with DC-LVDT transducers, string pots, and strain gauges. The instrumentation layout was illustrated in Figures 8.4a to 8.4c for three types of sensors. Due to geometrical symmetry, only half of the girder was instrumented. Specifically, six electrical resistance strain gauges were deployed as illustrated in Figure 8.4a on the longitudinal GFRP bars. They were designated as SG-01 to SG-06. The strain gauges were located on several tension and compression reinforcement bars at mid-, and quarter spans, respectively. These strain gauges were used to quantify the stress distribution developed in the concrete box girder.

The vertical deflections of the box girder at mid-span and quarter span, schematically shown in Figure 8.4b, were measured with two pairs of four string pots symmetrically distributed on both sides of the box girder. In addition, two DC-LVDT transducers as shown in Figures 8.4b and 8.4c were installed at one-eighth span. These six displacement transducers were designated as D1 to D6.

The NI Compact Rio Data acquisition system, Figure 8.4c, was used to collect data from all sensors and the force output from the load cell. The sampling frequency used was 10 Hz for all tests. The collected data was automatically filtered in the NI Compact Rio program.

8.2.4 Load protocols

The hydraulic jack was used to apply a half-reversed cyclic load of increasing amplitude with a constant load rate of 200 lb/min (890 N/min) in force control. To develop a load protocol, the crack moment M_{cr} was first evaluated according to ACI 318-08:

$$M_{cr} = \frac{f_r I_g}{\bar{y}}, \quad f_r = 7.5 \sqrt{f'_c} \quad (8.1)$$

For a simply-supported beam, the crack moment in Eq. 8.1 corresponds to an applied point load at mid-span P_{cr} :

$$P_{cr} = \frac{4 f_r I_g}{L \bar{y}} \quad (8.2)$$

in which f_r and f'_c represent the rupture modulus and compressive strength of concrete, respectively; I_g and \bar{y} are the moment of inertia and the distance from the extreme compression fiber to the neutral axis of the cross section; and L is the span length of the box girder. Specifically for the test specimen $f'_c = 7.8$ ksi, the load corresponding to the crack moment was estimated to be 40 kips (178 kN). The cyclic load steps were set to +20, +30, +40, +50, +70, +90, +110, +130, +150, +180, +240, and +270 kips. After those cycles, the specimen was loaded monotonically till failure, as indicated in Figure 8.5. At the beginning, smaller steps were considered to ensure that the initial cracks were captured. Due to the expected bi-linear behavior as observed from the testing of the concrete slab in Chapter 7, the load steps were increased after

concrete cracking. To allow time for crack marking and measurement, tests halted for one to ten minutes at the peak of each loading cycle.

8.3 Laboratory test results and discussion

The 27-ft (8.2-m) specimen with a clear span of 25 ft (7.6 m) was subjected to three-point bending by an applied load at mid-span. The thickness of the box girder was 26 in. (660 mm). The box girder was designed with over reinforcement to achieve crushing of the concrete at compressive zone under unexpected loads.

At a load level of approximately 30 kips (134 kN), initial flexural cracks were observed near mid-span as shown in Figure 8.6a. When the girder was loaded at 50-70 kips (222-311 kN), more flexural cracks developed from the mid-span to the end supports as indicated in Figure 8.6b. However, the cracks near the quarter span are narrower than those in mid-span up to 70 kips (311 kN). Due to shear action, diagonal cracks began to occur near the mid-span at a load of about 90 kips (400 kN) as indicated in Figures 8.6c, 8.7 and 8.8. Approaching the failure, the box girder experienced horizontal splitting cracks near the top GFRP reinforcement due to concrete crushing. At 270 kips, the splitting cracks were then connected with the previous diagonal cracks as shown in Figure 8.9. Like the concrete slab discussed in Chapter 7, the concrete crushing started from the perimeter of the spread beam, which is slightly away from the mid-span as indicated in Figures 8.7 and 8.8. This is likely attributed to the constraint effect provided by the spread beam. Due to a significantly smaller length-to-height ratio, the box girder has a relatively higher shear effect than the concrete slab discussed in Chapter 7, resulting in a less significant deflection, approximately 4.25 in (108 mm), before the concrete cover was completely crushed in compression zone.

The load-deflection curves at mid-span, quarter span and one-eighth span were plotted in Figures 8.10a to 8.10c, respectively. All load-deflection curves showed the bi-linear behavior if the envelopes of the hysteretic loops were constructed by connecting the peak loads from all loading cycles. The first line segment was up to initial flexural cracking. After that, the stiffness of the second line segment, as observed in close-up view in Figure 8.10a, was approximately 1/3 of that of the uncracked box girder. The slopes of unloading curves from each targeted loading level lay between those of uncracked and cracked box girder. Since the GFRP bars remained elastic during the tests, the residual deformation in the box girder was less than 1 in. (2.54 mm) when the girder was loaded to 320 kips. The final residual deformation was only 1 in. (2.54 mm) even after crushing of the concrete. The residual deformation was likely caused by bonding slippage between the GFRP bars and concrete matrix.

The bending stress of tensile GFRP bars in the box girder can be calculated from Eqs. 7.1 and 7.2 according to ACI 440 Guidelines (2006). Figure 8.11 presents the stress-strain relations of the girder at mid-span, based on the calculated stress and the measured strain. Once again, bi-linear behavior was observed from the stress-strain curves as clearly seen in the close-up view in Figure 8.11. The box girder failed when the tensile GFRP reinforcement was strained to approximately 0.005, corresponding to 25 ksi (172 MPa). The maximum strain at the failure of the girder was significantly less than the manufacturer's specified ultimate strain of No.10 (#32) GFRP bars (0.01182) corresponding to an ultimate strength of 70 ksi (483 MPa) as listed in Table 5.1. Therefore, the maximum strain in the GFRP reinforcement at mid-span of the girder was approximately 42 % of the ultimate strain. The stress level proportional to the maximum strain was approximately 29.6 ksi (204 MPa), which is comparable with 25 ksi (172 MPa)

predicted by Eq. 7.1 and confirms that the girder design by ACI 440.1R-06 Guidelines was conservative.

8.4 Field test program

After the laboratory validation, the box girders were cast and brought to the bridge site for rapid erection. The field test of the box-girder span aimed to understand the overall performance of the bridge system including the precast box girders, investigate the relative movement between precast box girder elements, and determine the load distribution within a precast box girder.

8.4.1 Instrumentation plan

The instrumentation plan of DC-LVDT transducers, inclinometers, and accelerometers was schematically shown in Figures 6.15 and 6.17. The typical installation process of the three types of sensors can be found in Figures 7.24 to 7.26, respectively. Specifically, twenty DC-LVDT transducers, shown in Figures 6.14 and 7.24, were deployed on the bottom surface of the box girders to monitor their vertical deflection as truck(s) was driven through the bridge. In addition, seven accelerometers as shown in Figure 7.25 were installed on the interior girder for acceleration measurement when truck(s) passed the bridge at pre-determined speed.

8.4.2 Load protocols for field testing

The test matrix of truck passes and stops on the bridge was given in Table 6.2 and presented in Figures 6.6 to 6.13. A total of twenty-one load cases were performed for bridge assessment under static and dynamic loads. The test results and discussion were presented below.

8.5 Field test results and discussion

8.5.1 Longitudinal distribution of deflections

The longitudinal distributions of vertical deflections for various truck passes and stops are presented in Figures 8.12 and 8.13 for north exterior and north interior girders, respectively. Similar to the steel girder in the steel-girder span in Chapter 7, the north exterior girder experienced the maximum deflection among all load cases (six load groups) when the truck parked at Stop 3 near mid-span of the bridge span. In comparison with Stop 3, Stops 1 and 4 signified the truck(s) located near the two ends of the bridge so that both stops generated smaller deflections but greater shear forces. The static deflections of the north exterior girder in all load cases demonstrated that Pass 1 represented the worse-case load condition for the north exterior girder since the truck passed the bridge right over the girder. A closer examination at Figures 8.12a and 8.12b indicated that, as the truck shifted from Pass 1 to Pass 2, the longitudinal distribution and the maximum value of vertical deflections decreased slightly. This was because, unlike the concrete slab supported on five steel girders that are in turn simply supported at two ends, all four box girders directly rested on the two end supports and half of the truck load remained on any girder in all cases. Note that the test data from Pass 3 was unavailable due to temporary malfunction of the acquisition system during tests. Obviously, two trucks along Pass 4 induced larger deflections in the exterior girder as clearly indicated in Figure 8.12c.

The vertical deflections of the north interior box girder as shown in Figures 8.13a to 8.13c indicated the similar trend to the north exterior girder as far as the effect of various truck stops is concerned. Specifically, Stop 3 generated the larger deflection than Stops 1 and 2 in all load cases. Unlike the exterior girder, however, as the truck shifted from Pass 1 to Pass 3, the deflection of the north interior girder slightly increased due to the fact that the box girders are directly supported at two ends and nearly half of the truck load remained on any single girder. In

fact, the maximum deflection of the interior girder during Pass 3 was 5 % larger than that during Pass 1. Once again, the two trucks loading as shown in Figure 8.13d induced larger deflections than those by a single truck shown in Figures 8.13a to 8.13c.

8.5.2 Transverse distribution of deflections

The mid-span deflections of the four girders are presented in Figures 8.14a to 8.14d for truck Passes 1 to 4, respectively. As the truck shifted from Pass 1 to Pass 3, the transverse distribution of the girder deflections changed from nearly linear to parabolic symmetric about the bridge centerline. Overall, the transverse distribution of the girder deflections was smooth, indicating little relative movement between box girders and a system behavior of the bridge with four box girders. The maximum relative movement between the north exterior and interior girders during Pass 1 as shown in Figure 8.14a was less than 0.005 in. or 15 % change.

The maximum deflection of the box-girder span under all load cases was 0.0264 in. (0.67 mm) at mid-span of the bridge when loaded with two parallel trucks (88 kips or 392 kN). This level of deflection is significantly less than 0.083 in. (2.1 mm) of the steel-girder span discussed in Chapter 7. Therefore, the box girder span is considerably stiffer than the steel-girder span. The mid-span deflection of the box-girder span in all load cases was only 7% of the allowable deflection specified by ACI 318-11 (2011) and AASHTO (2010), which is $L/800 = 0.405$ in. (10.3 mm).

8.5.3 Dynamic deflection and live load impact factor

As previously done for the steel-girder span in Chapter 7, for the box-girder span the impact factor for live load due to the dynamic effect of vehicles was investigated using Load groups 4 and 6 when one truck and two trucks passed through the bridge at approximately 35

mph (56 kph) for Pass 2 and 15 mph (24 kph) for Pass 4, respectively. Figures 8.15a and 8.15b present the mid-span deflection time histories induced by truck Pass 2 and Pass 4. In comparison with Figures 7.30a and 7.30b, the deflection time histories of the box-girder span are smoother and the ration between the effects of two trucks in Pass 4 and one truck in Pass 2 is considerably higher. Both observations indicated that the dynamic effect of the vehicles on the box-girder span is significantly less.

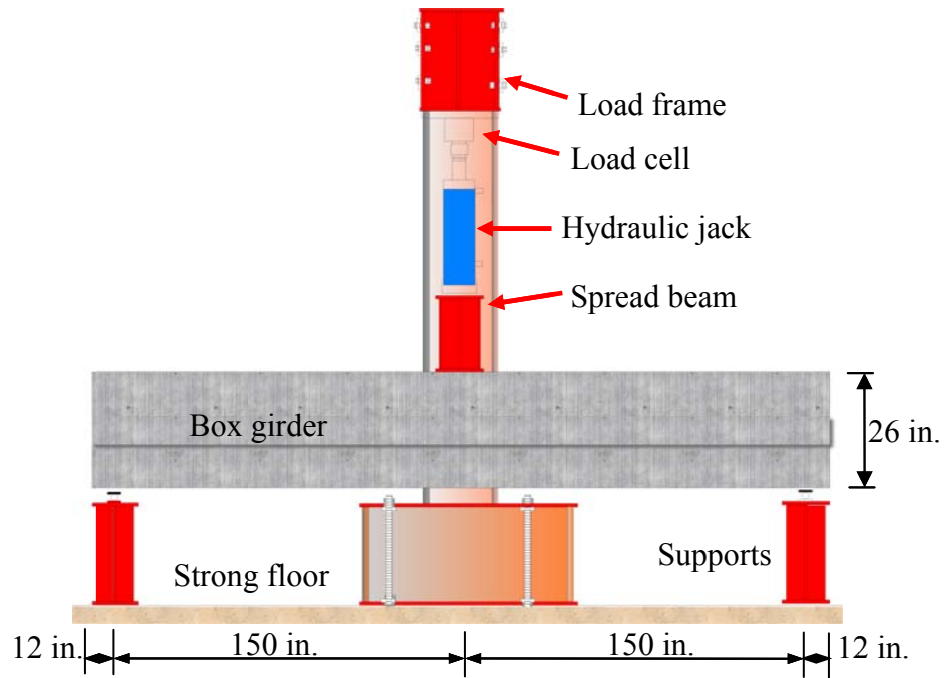
The dynamic deflections are compared with the corresponding static deflections in Figures 8.16a and 8.16b for the north exterior girder, Figures 8.16c and 8.16d for the north interior girder, and Figures 8.16e and 8.16f for mid-span of all girders. The impact factor (IF) for live load was computed as the ratio of the dynamic deflection obtained at 35 mph (56 kph) and 15 mph (24 kph) to the static deflection obtained from Stop 1 to Stop 4. Note that the two trucks may not exactly follow Pass 4 during dynamic tests and thus both static deflections from Pass 1 and Pass 2 were used as references in Figure 8.16. Out of 110 loading cases, 53 give positive impact factors as depicted in Figure 8.16g. The positive impact factors were used to calculate the average live load impact factor of 0.12. This factor is considerably less than the prescribed dynamic load allowance (impact) for a 27 ft (8.23 m) long bridge, which is 0.33 according to AASHTO Specifications (2010).

8.6 Summary

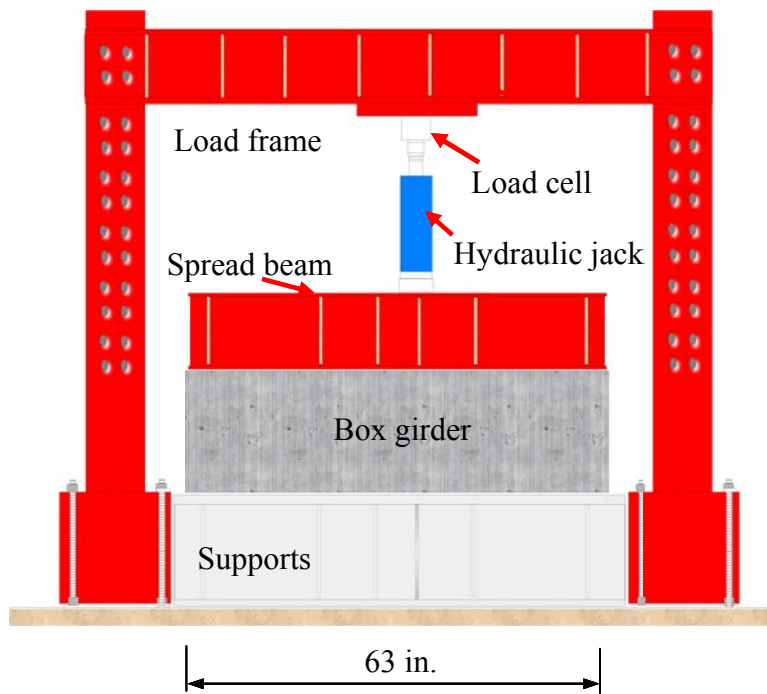
In this chapter, the structural behavior of a box girder was investigated with laboratory tests to failure and the box-girder bridge performance was investigated with in-situ load tests under design truck loads. Based on the experimental results and analyses, the box-girder bridge design was demonstrated to be satisfactory in terms of both strength and deflection requirements.

Corresponding to concrete crushing of the tested box girder, the mid-span strain of GFRP reinforcing bars was approximately 42 % of the ultimate strain specified by the GFRP manufacturer. The stress level proportional to the maximum strain was approximately 29.6 ksi (204 MPa), which is comparable with 25 ksi (172 MPa) predicted by ACI 440.1R-06 Guidelines. Since only 42 % of the specified ultimate tensile strength of GFRP bars was used when the GFRP reinforced box girder failed in concrete crushing, the girder design provided sufficient reserved capacity to prevent GFRP bars from rupture in unexpected circumstances. In addition, the maximum load that the box girder can take prior to concrete crushing as designed was approximately 270 kips (1200 kN). This level of load capacity (concentrated at mid-span) is substantially larger than the maximum load effect that two fully-loaded HS20 trucks in application can possibly induce on a simply-supported bridge with a clear span of 25-ft (7.62 m). For example, the total load of two rear axles of two HS20 trucks is only 128 kips (570 kN).

The bridge built with four simply-supported box girders worked mainly as a structural system under design truck loads. The maximum relative movement between adjacent box girders under all load cases was 0.005 in. (0.13 mm). The maximum deflection at mid-span of the box-girder bridge under all load cases was 0.0264 in. (0.67 mm) when two fully-loaded trucks (88 kips or 390 kN) passed in parallel through the bridge. The mid-span deflection of the box-girder span in all load cases was less than 7% of the allowable deflection specified by ACI 318-11 (2011) and AASHTO (2010). It was significantly less than that of the steel-girder span discussed in Chapter 7. Therefore, the box girder span is considerably stiffer than the steel-girder span. In addition, the deflections in various truck passes meet the superposition principle, indicating that the bridge system remained elastic under the design loads.



(a) Elevation view with a point load at mid-span



(b) End view

Figure 8.1: Schematic of laboratory test setup for concrete box girder

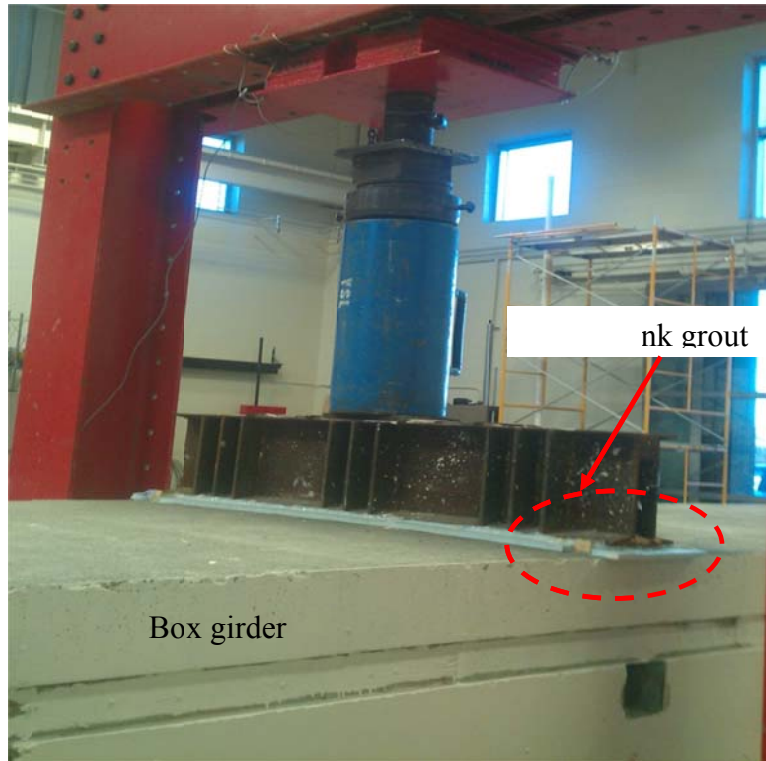


(a) Load frame

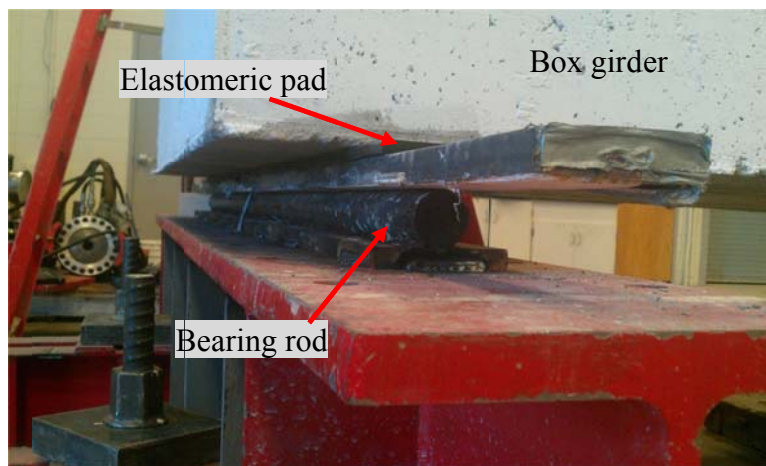


(b) Overview of test setup

Figure 8.2: Photos of laboratory test setup for concrete box girder

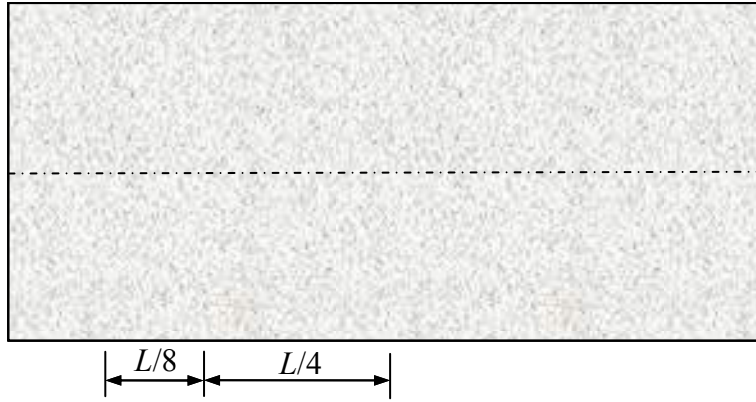


(a) Spread beam attachment on top surface of the box girder

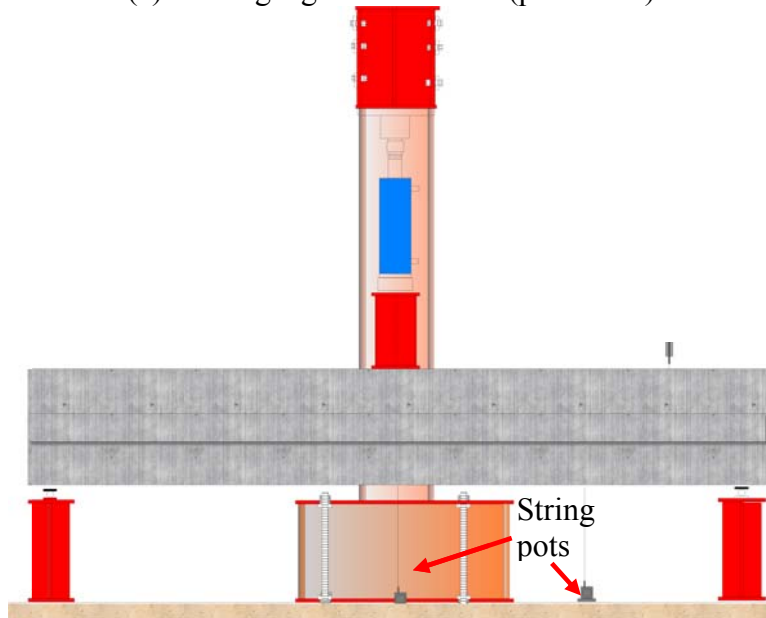


(b) Support details of the box girder

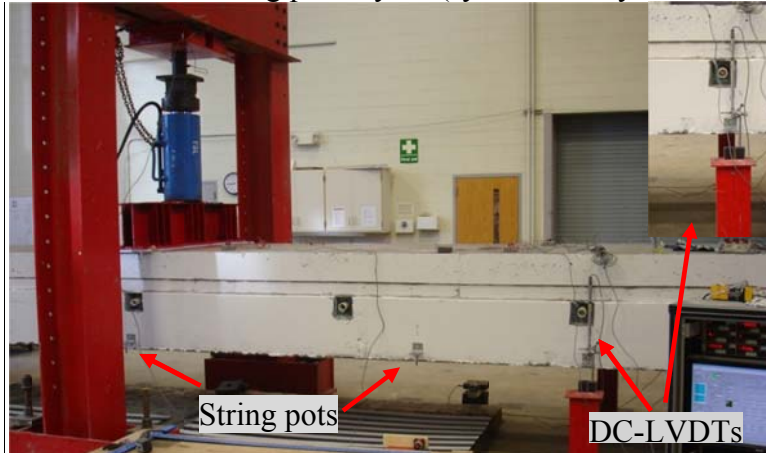
Figure 8.3: Attachment details at supports and loading mechanism



(a) Strain gauges distribution (plan view)



(b) Schematics of DCVTs and string pots layout (symmetrically distribution at both sides)



(c) Overview of sensor layout

Figure 8.4: Instrumentation layout

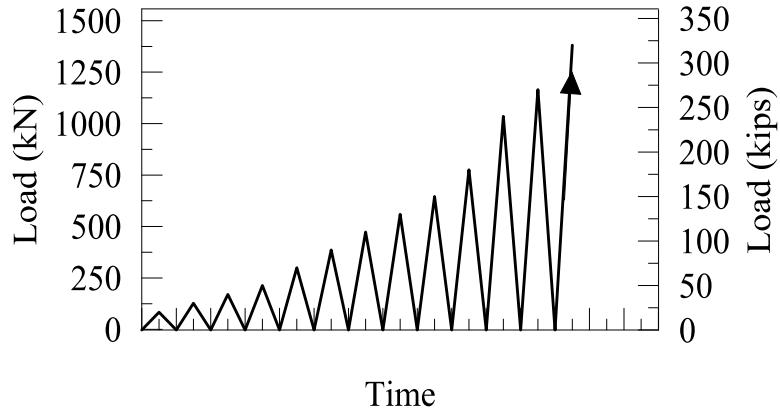
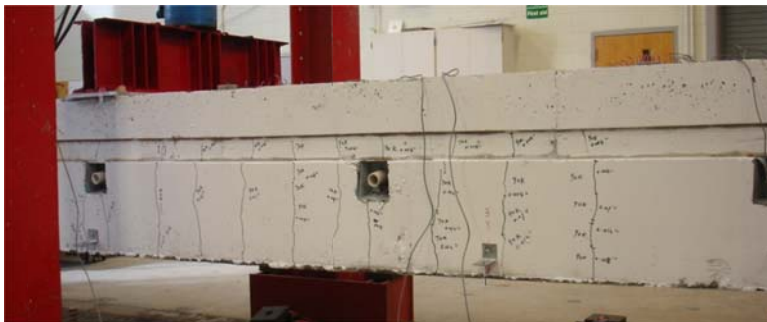


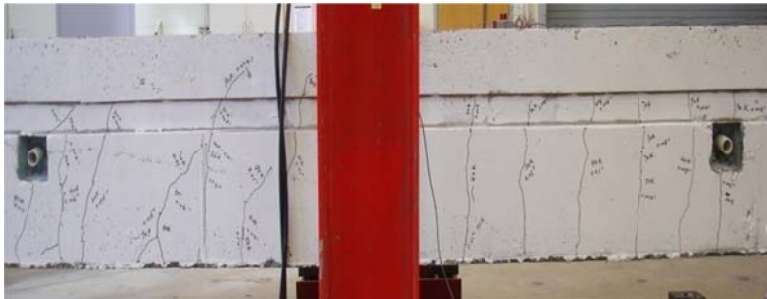
Figure 8.5: Load protocol of the box girder



(a) Initial flexural cracks



(b) Further cracks developed over the span



(c) Diagonal cracks developed away from the mid-span
Figure 8.6: Crack development and propagation



(a) Overview of the crack pattern



(b) Concrete crushing and horizontal splitting cracks

Figure 8.7: Box girder failure by concrete crushing in compression zone

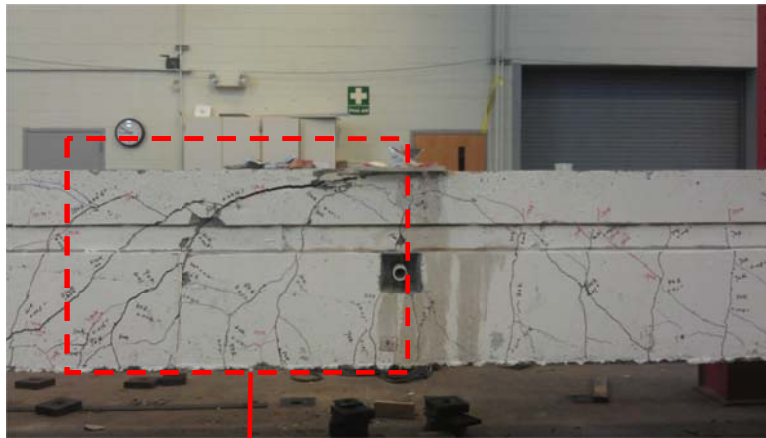


(a) Left half span

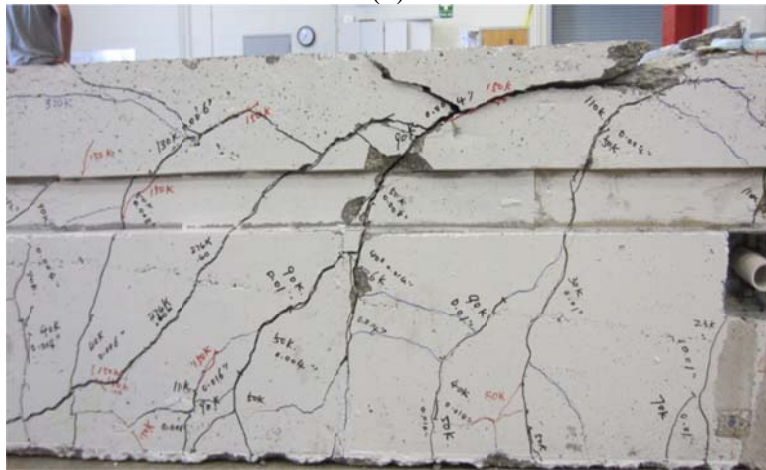


(b) Right half span

Figure 8.8: Crack pattern across the span

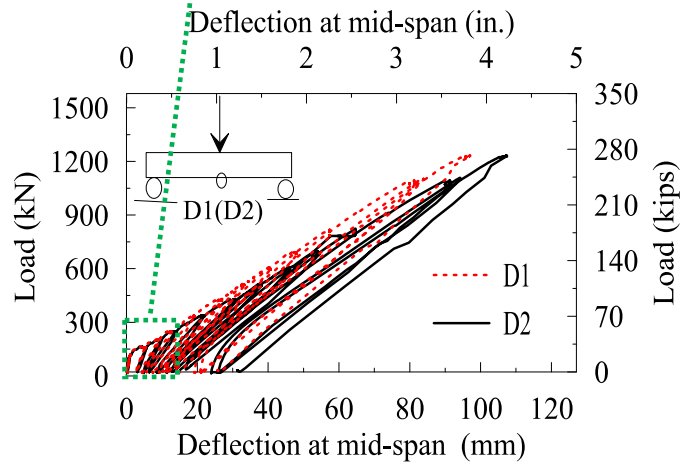
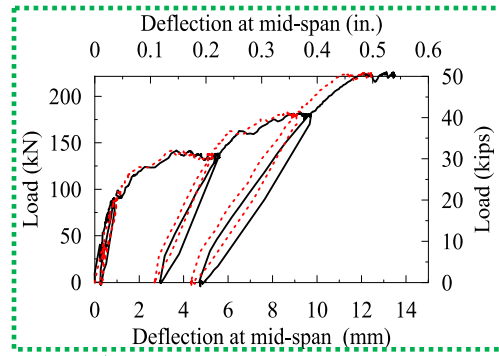


(a)

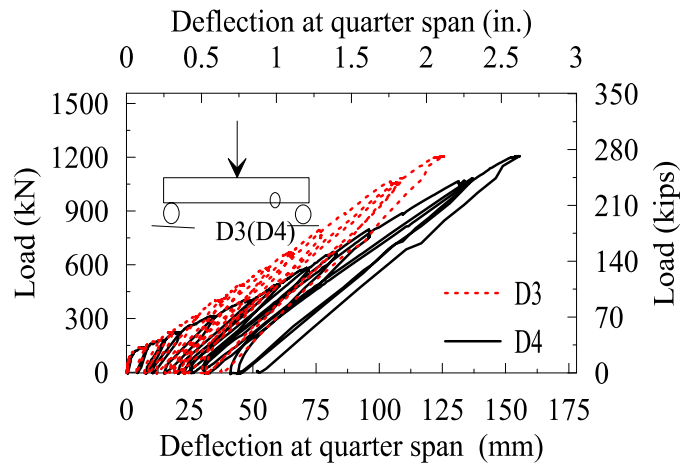


(b)

Figure 8.9: Shear failure details



(a) Mid-span



(b) Quarter span

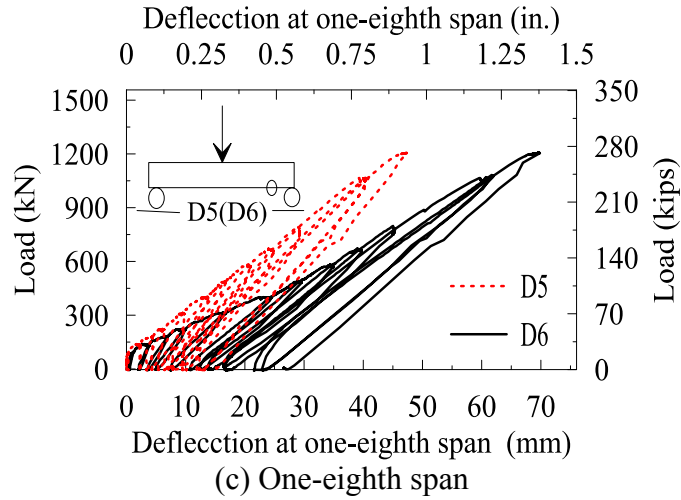


Figure 8.10: Load-displacement curves at various locations

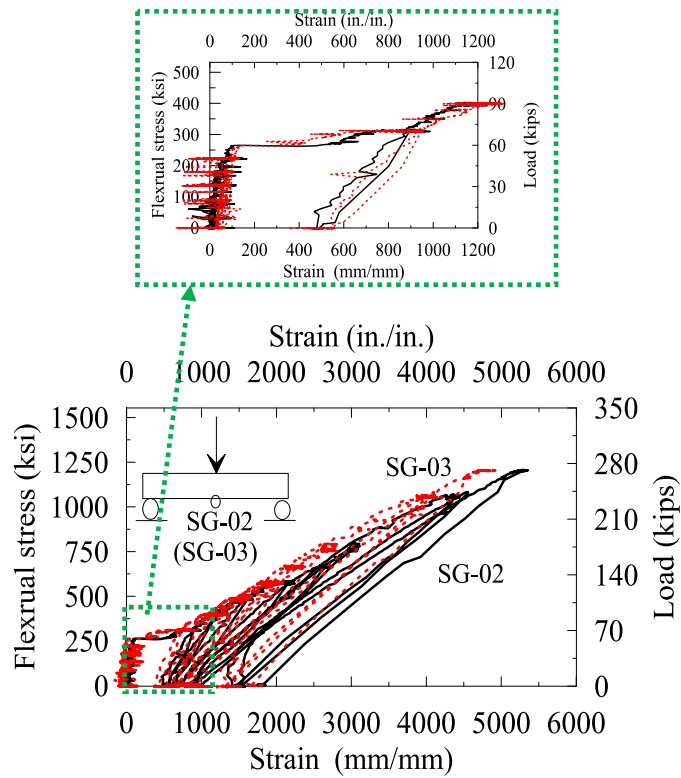
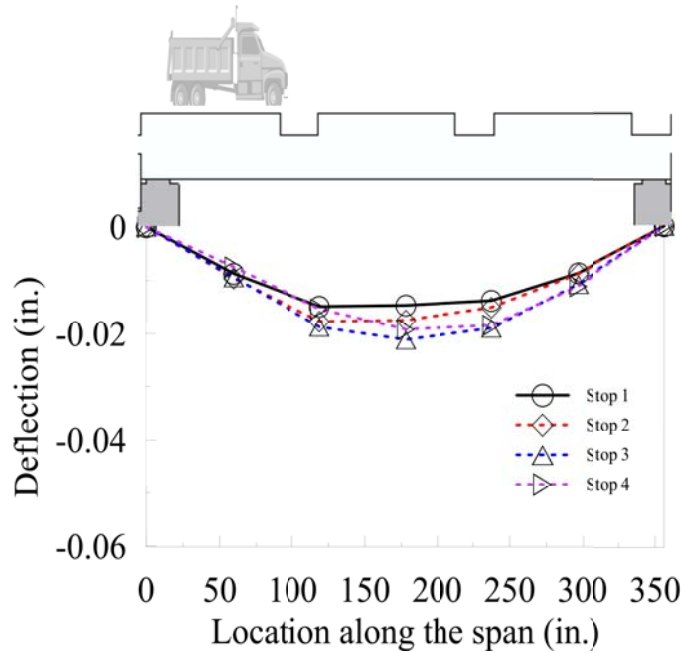
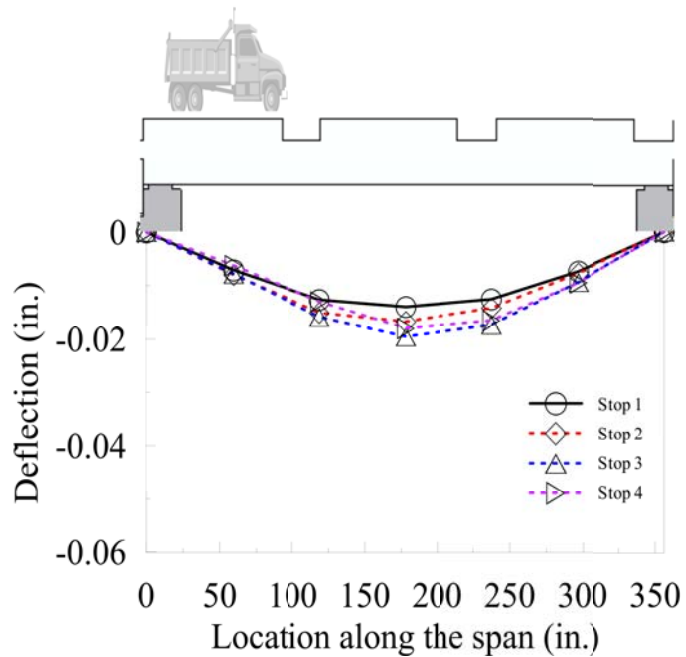


Figure 8.11: Stress-strain curves of GFRP bars at mid-span



(a) SSLC 11-14 (Load group 1: Pass 1)



(b) SSLC 21-24, SDLC 41 and DDLC 61 (Load group 2, 4, and 6: Pass 2)

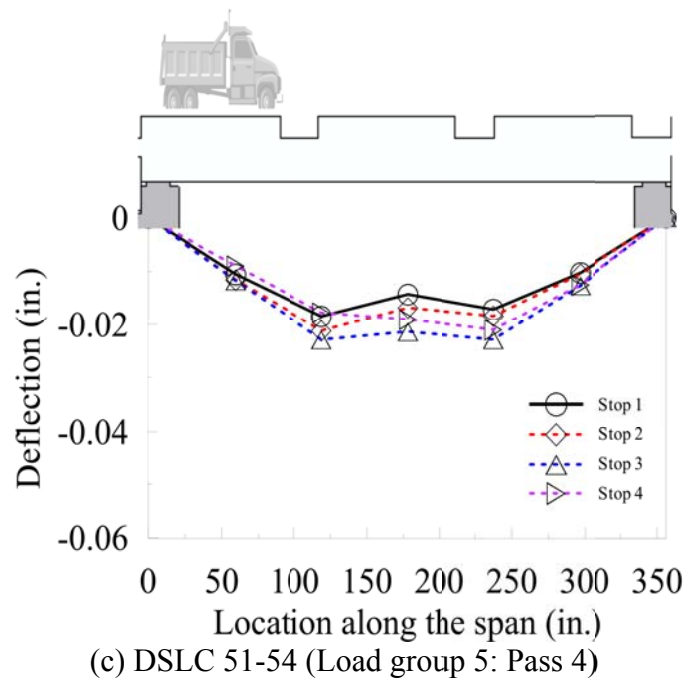
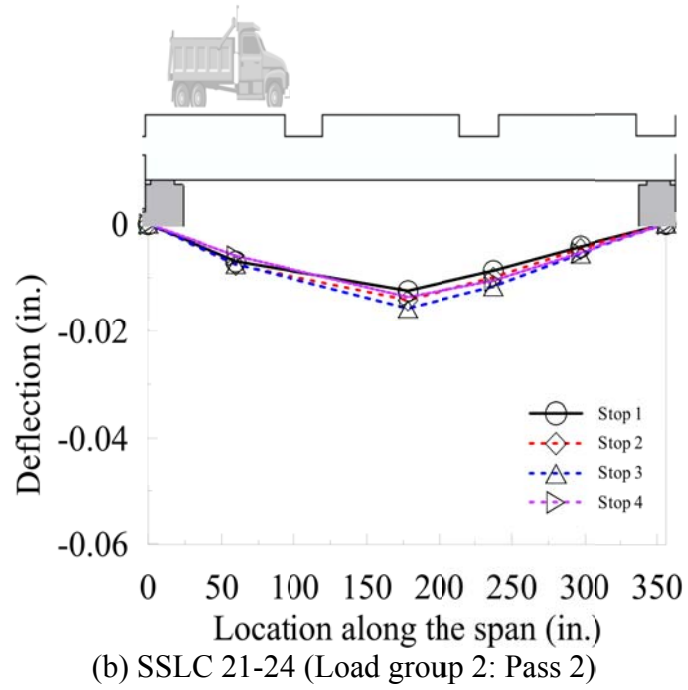
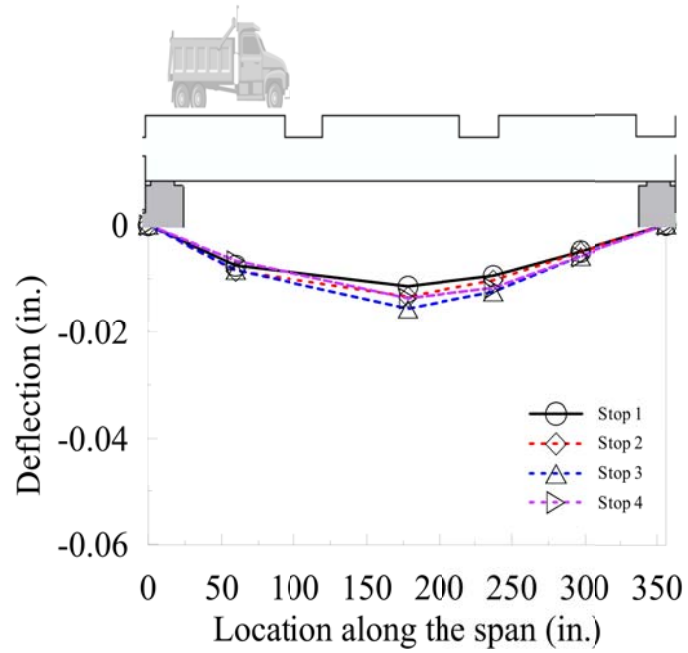
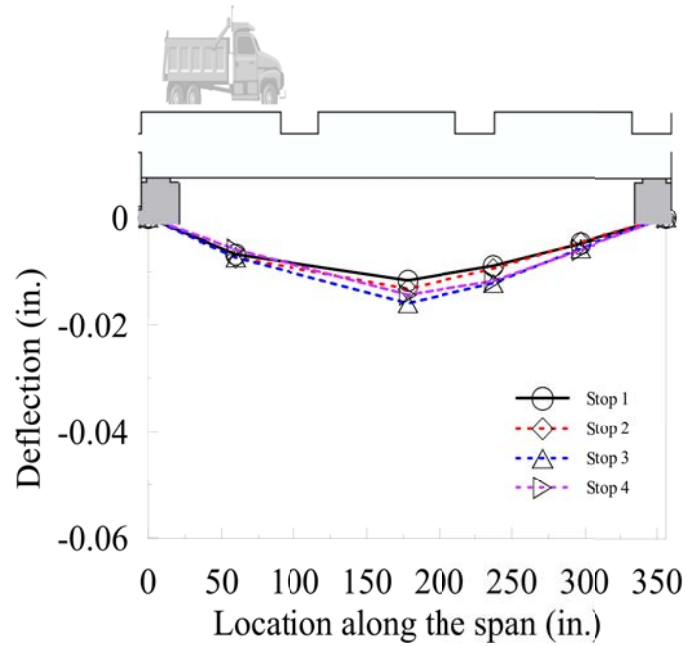
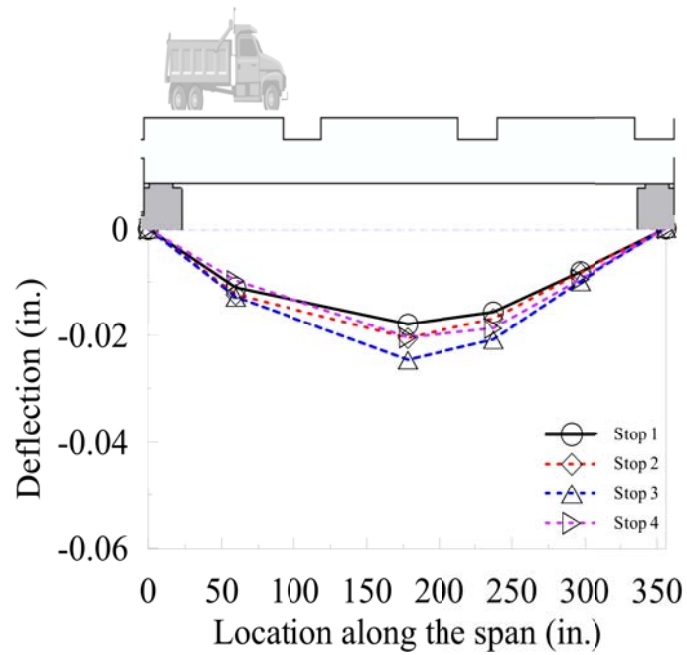


Figure 8.12: Static deflections of north exterior box girder under various load cases



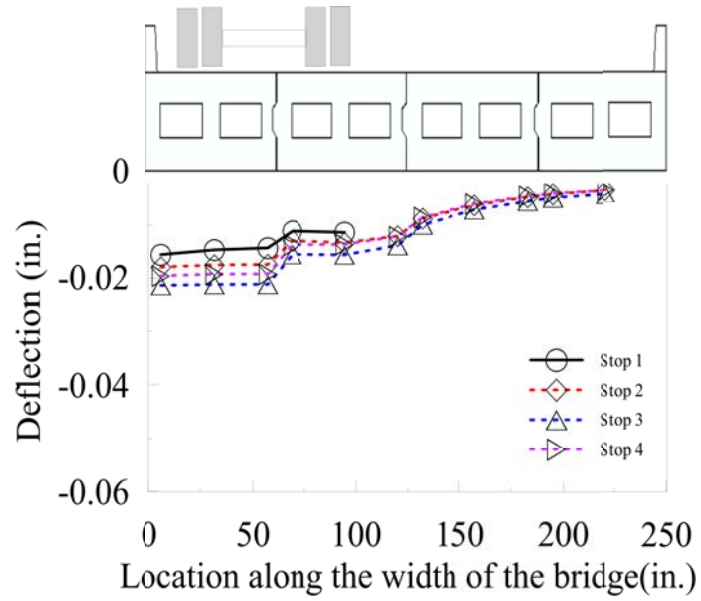


(c) SSLC 31-34 (Load group 3: Pass 3)

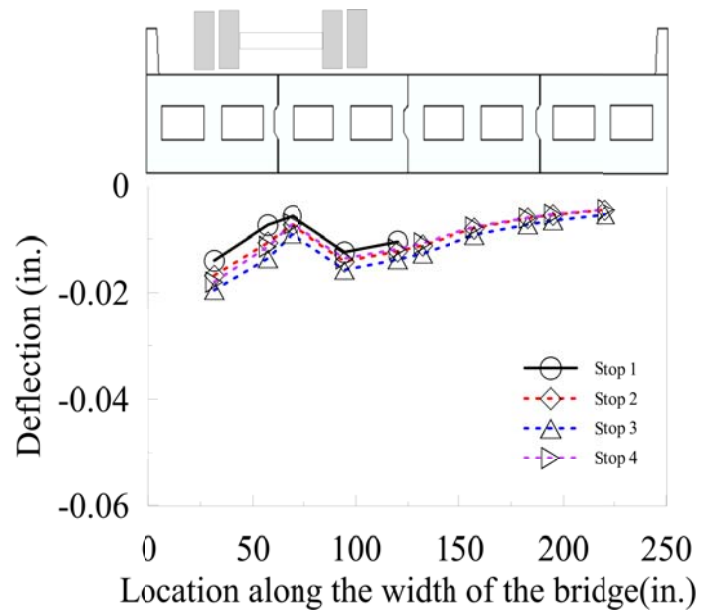


(d) DSLC 51-54 (Load group 5: Pass 4)

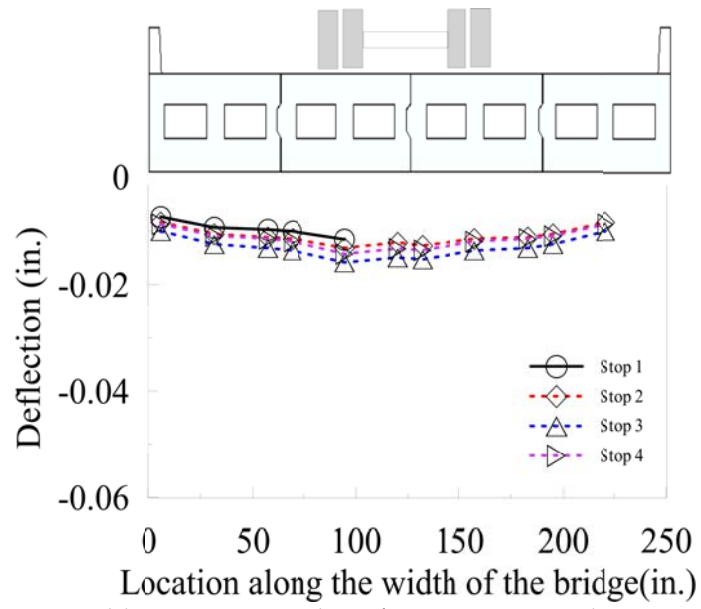
Figure 8.13: Static deflections of north interior box girder under various load cases



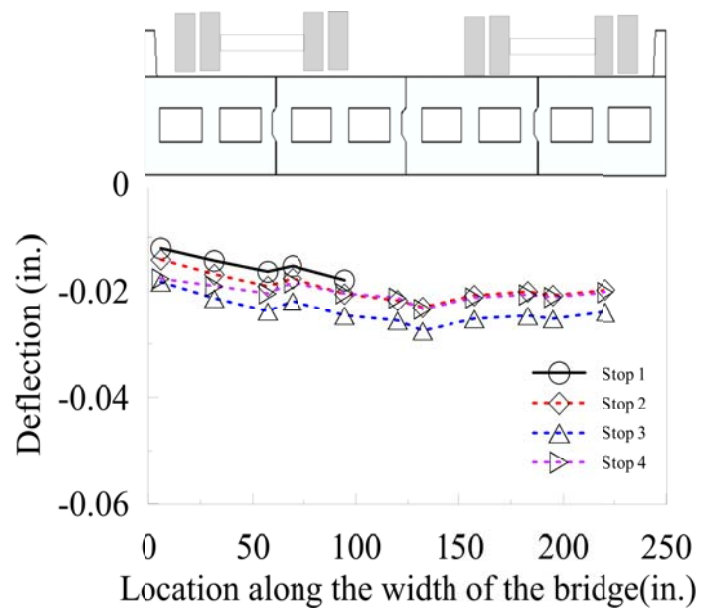
(a) SSLC 11-14 (Load group 1: Pass 1)



(b) SSLC 21-24 (Load group 2: Pass 2)

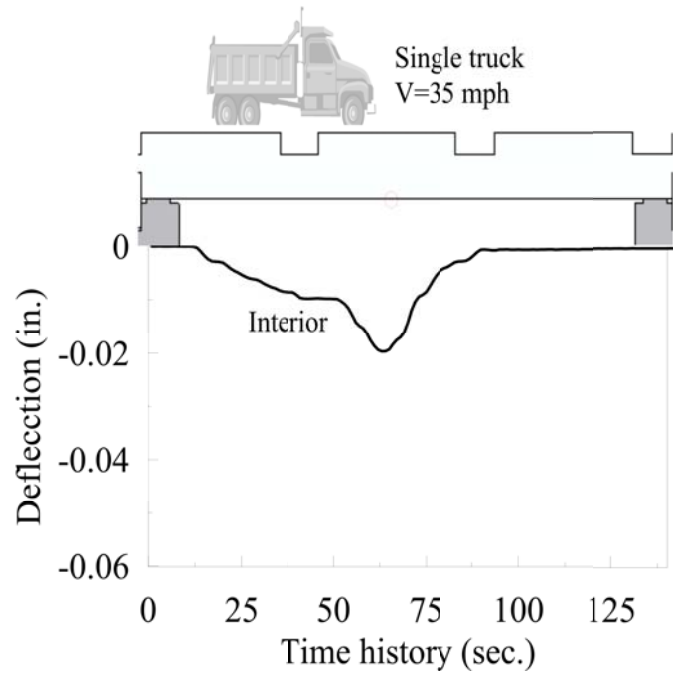


(c) SSLC 31-34 (Load group 3: Pass 3)

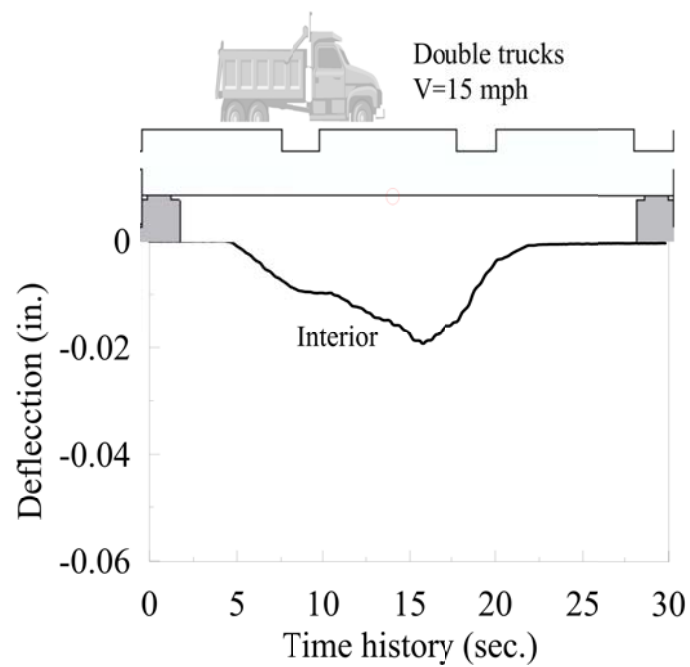


(d) DSLC 51-54 (Load group 5: Pass 4)

Figure 8.14: Static deflections at mid-span of multiple box girders under various load cases

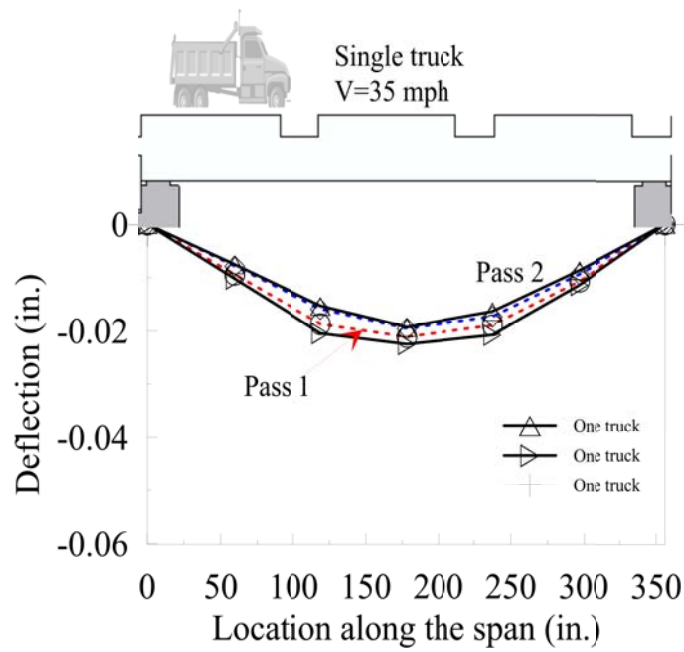


(a) SDLC 41 (Load group 4: Pass 2 with one truck)

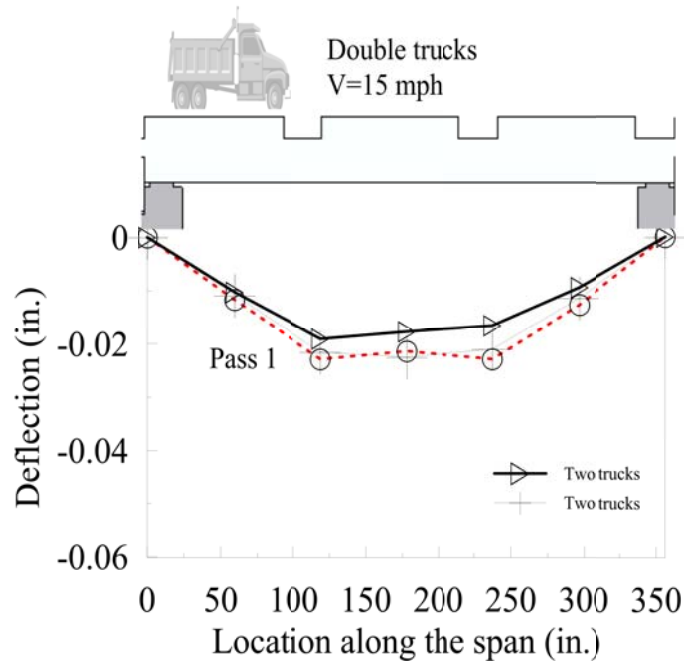


(b) DDLC 61 (Load group 6: Pass 4 with two trucks)

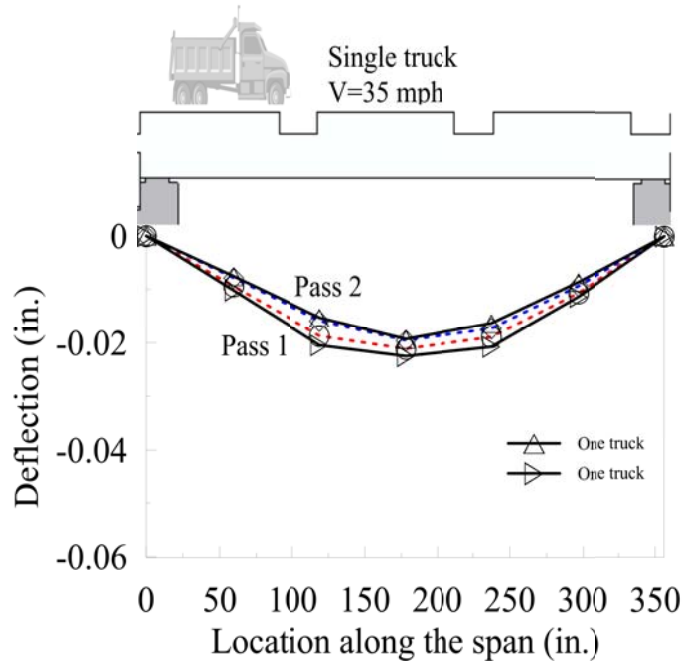
Figure 8.15: Deflection time histories at mid-span



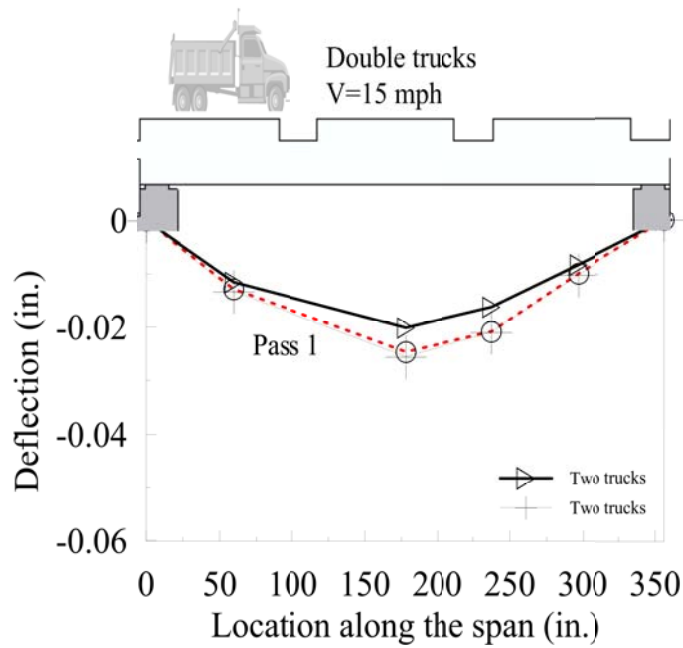
(a) Dynamic vs. static deflections of the north exterior box girder due to one truck live load



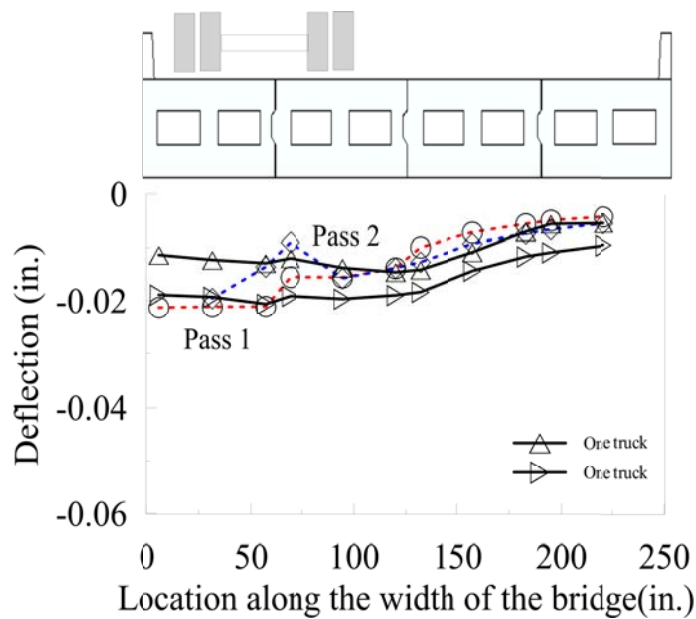
(b) Dynamic vs. static deflections of the north exterior box girder due to two trucks live load



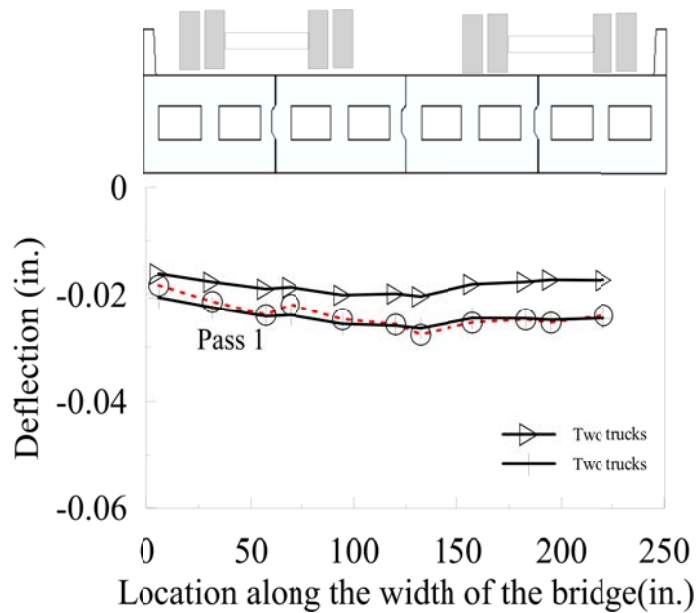
(c) Dynamic vs. static deflections of the north interior box girder due to one truck live load



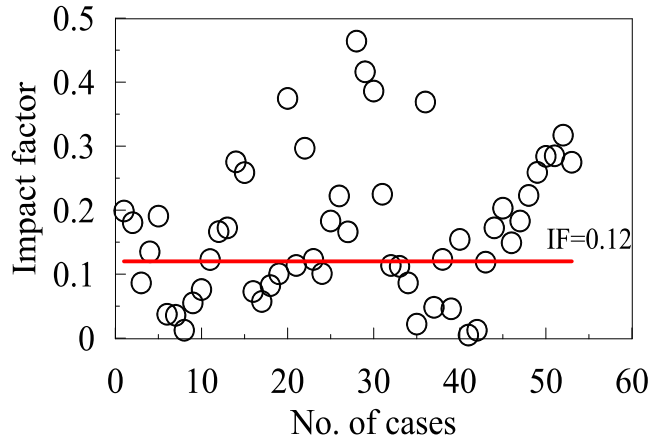
(d) Dynamic vs. static deflections of the north interior box girder due to two trucks live load



(e) Dynamic vs. static deflections at mid-span of multiple girders due to one truck live load



(f) Dynamic vs. static deflections at mid-span of multiple girders due to two trucks live load



(g) Impact factor for live load

Figure 8.16: Dynamic effects and impact factor for live load due to truck(s)

Chapter 9. Conclusions and Recommendations

9.1 Project Summary

The existing culvert was located on Pat Daly Road over Arnault Branch Creek, Washington County, MO. It was structurally inadequate and functionally obsolete, and thus posed a safety threat. In collaboration with Great River Associates, Springfield, MO, Missouri University of Science and Technology (Missouri S&T) proposed to replace the existing culvert with a rapidly constructed three-span bridge with precast GFRP-bar reinforced concrete decks and girders and cast-in-place cladding steel reinforced concrete walls and abutments for high corrosion resistance and durability of the bridge system. The bridge deck was finished with an approximately 3 in. (76 mm) asphalt overlay wearing surface. The entire bridge was constructed by crews from Washington County, MO, with a total engineering and construction cost of approximately \$340,000. The post-tensioning of CFRP bars was completed by Missouri S&T.

The overall objective of this research project was to conduct a comprehensive performance evaluation (design, construction, laboratory and field testing) of the three-span bridge so that the experience gained can provide a unique corrosion-free case modular construction case study for future superstructure and deck replacement of short-span girder bridges. The first and third spans were composed of three precast and longitudinally post-tensioned GFRP reinforced concrete slabs that were supported on five steel/concrete girders, respectively. The idea of using GFRP bars as flexural and shear reinforcement would be implemented with relevant implications from the structure and constructability points of view. The middle span had four precast box girders, each reinforced with GFRP bars and simply supported on wall piers at both ends. The box girders were transversely post-tensioned at the

bridge site to close the longitudinal joints between them. This span was a new application of GFRP bars in the design of precast box girders, requiring no additional deck and accelerating the construction process.

Prior to field construction, a full-size, 27 ft (8.23 m) long and 5.25 ft (1.60 m) wide concrete box girder reinforced with GFRP bars was simply supported and tested to failure under three-point loading in the Highbay Structures Laboratory at Missouri S&T to ensure that the innovative design behaved as expected. Similarly, a full-size, 21 ft (6.40 m) long and 9 ft (2.74 m) wide concrete slab reinforced with GFRP bars was simply supported and tested to failure with two different span lengths: long span for flexural behavior and short span for shear behavior. One month after the completion of field construction, in-situ load testing was conducted to assess the structural performance of the bridge system and precast components. Both the laboratory test specimens and field deployed precast members were densely instrumented with embedded strain gauges and linear variable differential transformers to measure strains and deflections at critical locations. A wireless communication system was designed and developed for long-term bridge monitoring but not used during the field testing due to weak signal at the bridge site.

9.2 Conclusions

Based on the design, construction, laboratory and field testing of the proposed three-span bridge, the following conclusions can be drawn:

- The uses of two conventional steel/concrete girder spans and one innovative concrete box girder span in one bridge system allowed a fair comparison in identical environmental setting. Furthermore, the equal simply-supported length of the three

spans allowed a comparative study on the performance and behavior of different structures in terms of dynamic effects, and load and deflection distributions.

- The precast and erection procedures of the proposed modular bridge system demonstrated that the precast bridge elements erected and post-tensioned at the bridge site resulted in significant saving in construction time.
- The laboratory test results indicated that the GFRP-bar reinforced concrete slab had sufficient flexural and shear strengths, meeting the design specifications. The flexural failure of the long span occurred by concrete crushing after the slab experienced excessive deflections. The shear failure of the short span occurred after the concrete shear strength was reached at small deflections. In both cases, the load capacity of the precast concrete slab significantly exceeded the required design strength. The shear capacity predicted by the ACI 440 guidelines was quite conservative.
- The laboratory test results also indicated that the box girder reinforced with GFRP bars failed in concrete crushing at 3 in. (76 mm) deflection in mid-span with no GFRP bar rupture, exhibiting satisfactory performance as designed. The girder capacity at failure greatly exceeded the required design strength.
- In-situ bridge load testing demonstrated that the newly erected bridge with precast components behaved like a system and provided the expected structural integrity to carry design loads. The relative displacement between parallel precast components was negligible. The measured deflection was only 18% of the allowable value for the steel-girder span and 7% for the concrete box-girder span. The average live load impact factor of over 50 test cases was 0.16 for the steel-girder span and 0.12 for the concrete box-girder span, both significantly less than the design value (0.33) in

AASHTO specifications. The deflection distributions under various load cases follow the superposition principle, indicative of an elastic behavior of the bridge system.

9.3 Recommendations

Based on the laboratory failure tests, field serviceability tests, and bridge analysis, the following recommendations are made:

- The precast bridge members (GFRP-bar reinforced concrete slabs and girders) and the bridge system meet both strength and deflection requirements, and are thus recommended as corrosion-free solutions to achieve long-term durability of short-span bridges.
- Long-term performance data of the constructed bridge should be collected over a long period of time, documenting the durability of various bridge decks and analyzing their relative merits in life-cycle cost reduction.
- The creep of concrete bridge decks and girders may induce additional deformation, potentially resulting in concrete cracking and structural degradation. It should be investigated in the following few years.
- The bridge system integrity should be further investigated by monitoring the relative displacement between adjacent precast components under design loading and the potential change in prestress level of the CFRP tendons over time.

References

- [1] AASHTO T277. Standard Method of Test for Rapid Determination of the Chloride Permeability of Concrete. American Association of State Highway and Transportation Officials, Washington, D.C., 1983.
- [2] AASHTO. AASHTO LRFD Bridge Design Specifications, 5th Edition, American Association of State Highway and Transportation Officials, Washington, DC, 1450 pp., 2010.
- [3] ACI Committee 201. Guide to Durable Concrete (ACI 201.2R-1). American Concrete Institute, MI: Farmington Hills, 2001.
- [4] ACI Committee 440. Guide to the Design and Construction of Structural Concrete Reinforced with FRP Bars (ACI 440.1R-06). American Concrete Institute, MI: Farmington Hills, 2006.
- [5] ACI 318. Building Code Requirements for Structural Concrete and Commentary (ACI 318-11), American Concrete Institute, MI: Farmington Hills, 2011.
- [6] Aldea C, Shah SP, and Karr A. "Effect of Cracking on Water and Chloride Permeability of Concrete." *ASCE Journal of Materials in Civil Engineering*, 11(3): 181-187, 1999.
- [7] Bertolini, L., Elsener, B., Pedferri, P., Polder, R. Corrosion of Steel in Concrete: Prevention, Diagnosis, Repair, Wiley-VCH, 2004.
- [8] Boothby, T. E. and J. A. Laman. "Bridge Concrete Deck Slab Cumulative Damage due to Vehicle Loading." *ASCE Journal of Bridge Engineering*, 4(1): 80-82, 1999.
- [9] Breña, S.F., Bramblett, R.M., Benouaich, M.A., Wood, S.L., and Kreger, M.E. Use of Carbon Fiber Reinforced Polymer Composites to Increase the Flexural Capacity of

- Reinforced Concrete Beams. Preliminary Review Copy, Center for Transportation Research, The University of Texas at Austin, 243 pp., 2001.
- [10] Cady P. and Weyers R. “Deterioration Rates of Concrete Bridge Decks.” *Journal of Transportation Engineering*, 110(1): 34-44, 1984.
- [11] Cao L., Allen J., Shing P., and Woodham D. “Behavior of RC Bridge Decks with Flexible Girders.” *ASCE Journal of Structural Engineering*, 122(1): 11-19, 1996.
- [12] CEB. Durability Concrete Structures: CEB Design Guide, Bulletin d’ Information No. 182, Switzerland: Comite Euro-International du Beton, 1992.
- [13] Choi, H., “Structural Health Monitoring System Based on Strain Gauge Enabled Wireless Sensor Nodes.” *Proceedings of the 5th International Conference on Networked Sensing Systems*, June 17-19, Kanazawa, Japan, pp. 211-214, 2008.
- [14] Deitz, D.H., Harik, I.E., and Gesund, H. “One-way Slabs Reinforced with Glass Fiber Reinforced Polymer Reinforcing Bars.” *Proceedings of the 4th International Symposium on Fiber Reinforced Polymer for Reinforced Concrete Structures*, Baltimore, MD, pp. 279-286, 1999.
- [15] El-Sayed, A., El-Salakawy, E., and Benmokrane, B. “Shear Strength of One-way Concrete Slabs Reinforced with Fiber-reinforced Polymer Composite Bars.” *ASCE Journal of Composites for Construction*, 9(2): 147-157, 2005.
- [16] Elzafraney, M., and Soroushian, P. “Quantitative Micro-structural Investigation of Deteriorated Reinforced Concrete Bridge Deck.” *ASCE Journal of Materials in Civil Engineering*, 17(2): 150-167, 2005.
- [17] FHWA. Federal Highway Administration Conditions and Performance Report: Chapter 11, <http://www.fhwa.dot.gov/policy/2006cpr/es11.htm>, 2006.

- [18] FHWA. Federal Highway Administration Deficient Bridges by State and Highway System, <http://www.fhwa.dot.gov/BRIDGE/britab.htm>, 2008.
- [19] Gunasekaran, A., Cross, S., Patel, N., and Sedigh, S. “Recent Enhancements to and Applications of the SmartBrick Structural Health Monitoring Platform.” *Proceedings of the SPIE Annual Symposium on Sensors and Smart Structures Technologies for Civil, Mechanical, and Aerospace Systems*, Vol. 8345, 2012.
- [20] Harms T., Shah P., Sedigh S., Bourque Z., Bastianini F. “Zigbee-enabled Structural Health Monitoring with the SmartBrick Network.” Proceeding of the 7th International Workshop on Structural Health Monitoring.” Stanford University, CA, 2009.
- [21] Huria, V., Lee, K., and Aktan, A. “Different Approaches to Rating Slab Bridges.” *ASCE Journal of Structural Engineering*, 120(10): 3056–3062, 1994.
- [22] Kornmann, X., Rees, M., Thomann, Y., Necola, A., Barbezat, M., and Thomann, R. “Epoxy-layered Silicate Nanocomposites as Matrix in Glass Fiber-reinforced Composites.” *Science and Technology*, 65: 2259-2268, 2005.
- [23] Laman, J. A. and Ashbaugh, J.R. “Highway Network Bridge Fatigue Damage Potential of Special Truck Configurations.” *Journal of the Transportation Research Board*, No. 1696, Vol. 1, pp. 81-92, National Research Council, Washington, D.C., 2000.
- [24] Lin, Z., Zhao, J., and Tabatabai H. Impact of Overweight Vehicles (with Heavy Axle Loads) on Bridge Deck Deterioration. Final Report CFIRE 04-06, USDOT’s RITA by CFIRE and UW-Milwaukee, WI, March 2012.
- [25] Mehta, P.K. and Gerwick, B.C. “Cracking-corrosion Interaction in Concrete Exposed to Marine Environment.” *Concrete International*, 4:45-51, 1982.

- [26] MoDOT. Standard Specifications for Road and Bridge Construction. Missouri Department of Transportation, MO, 1999.
- [27] Nanni, A. "Composites: Coming on Strong." *Concrete Construction*, 44, pp. 120, 1999.
- [28] Nanni, A. "FRP Reinforcement for Bridge Structures." *Proceedings of the Structural Engineering Conference*, the University of Kansas, Lawrence, KS, March 16, 2000.
- [29] Nanni, A., and Lopez, A. "Validation of FRP Composite Technology through Field Testing." *Proceedings of the 16th World Conference on NDT*, Montreal, Canada, August 30 - September 3, 2004.
- [30] Nystrom, H., Watkins, W.D., and Nanni, A. Laboratory and Field testing of FRP Composite Bridge Decks and FRP-Reinforced Concrete Bridge for the City of St. James, Phelps County, MO, RDT02-012, Center for Infrastructure Engineering Studies, UMR, 278 pp., 2002.
- [31] Oh, B. "Cumulative Damage Theory of Concrete under Variable Amplitude Fatigue Loading." *ACI Materials Journal*, 88(1): 41-48, 1991.
- [32] Poston, R., Carrasquillo, R., and Breen, J. "Durability of Post-tensioned Bridge Decks." *ACI Materials Journal*, 84: 315-326, 1987.
- [33] Sarja, A. and Vesikari, E. (Eds) Durability Design of Concrete Structures, RILEM Report 14, E&FN Spon, London, UK, 1996.
- [34] Winkelman, T.J. "Fiberglass Reinforced Polymer Composite Bridge Deck Construction in Illinois." FHWA/IL/PRR 145, Illinois Department of Transportation, 20 pp., 2002.
- [35] Wipf, T.J., Phares, B.M., Klaiber, F.W., and Lee, Y. "Evaluation of Post-tensioned Strengthened Steel Girder Bridge Using FRP Bars," Final Report, Center for Transportation Research and Education, Iowa State University, 76 pp., 2003.

- [36] Yan, D., Chen, G., Galati, N., and Sedigh, S. Design, Construction and Load Testing of the Bridge on Arnault Branch, Washington County, Missouri Using Innovative Technologies. Final Report CIES 10-001, Center for Infrastructure Engineering Studies, Rolla, Missouri, January 10, 2010.
- [37] Zararis, P.D. “Shear Strength and Minimum Shear Reinforcement of RC Slender Beams.” *ACI Structural Journal*, 100: 203-214, 2003.
- [38] Zarkaria, M., Ueda, T., Wu, Z., and Meng, L. “Experimental Investigation on Shear Cracking Behavior in Reinforced Concrete Beams with Shear Reinforcement.” *Journal of Advanced Concrete Technology*, 7: 79-96, 2009.

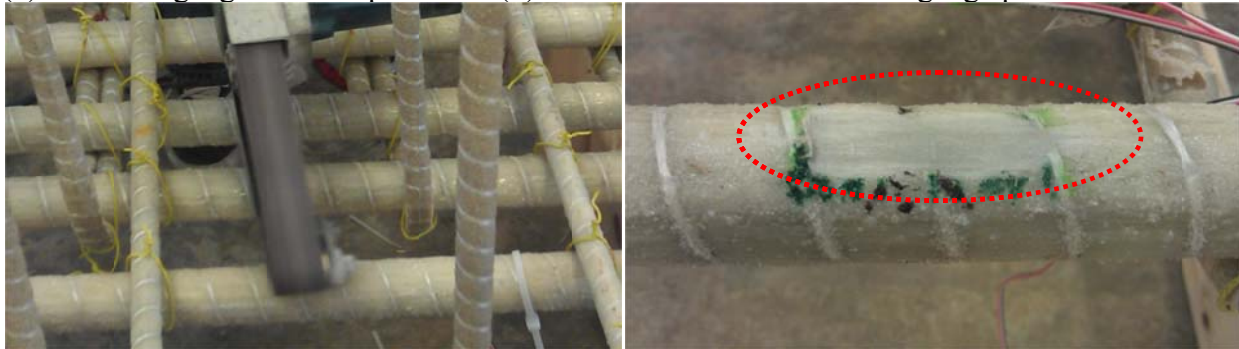
Appendix A: Strain Gauges (Half-bridge) Installation and Protection Procedures for Long-term Bridge Monitoring

1. Preparation for strain gauge installation

- (a) Set strain gauge wires in place for convenience of gauge installation
- (b) Mark the location of a pair of strain gauges on an FRP bar cage
- (c) Grind the top and bottom surfaces of the FRP bar using grade 60 sand papers to create two flat surfaces
- (d) Polish the flat surfaces using finer grade 120 sand papers to ensure that the flat surfaces are smooth for good contact with the two strain gauges to be installed, clean the mounting area with methyl alcohol, and remove any dust on the ground surfaces



(a) Set strain gauge wires in place (b) Mark the location of a strain gauge pair on a GFRP bar

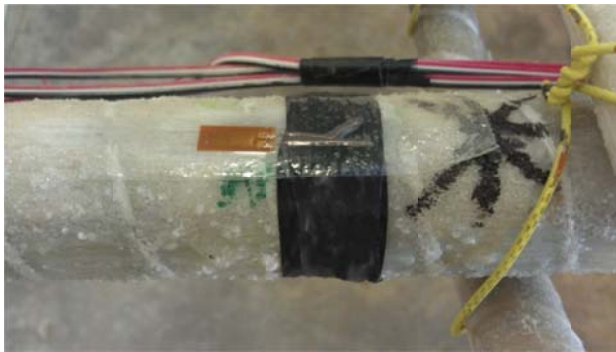


(c) Grind top and bottom of the bar to flat surfaces (d) Polish the flat surfaces to smooth surfaces

Figure 9.1: Preparation for strain gauge installation

2. Installation of strain gauges

- (a) Position two strain gauges on the top and bottom surfaces of the FRP bar by taping down their lead wires with an electrical (or insulating) tape
- (b) Fold up free ends of the strain gauges to expose the smooth bar surface for the firm attachment of the gauges
- (c) Stir up resin for about 5 minutes and let it set for another 5 minutes
- (d) Apply some resin on the smooth surface of the FRP bar with a plastic stick
- (e) Fold back the strain gauges and firmly press them down with foam, squeezing out any excessive adhesive and air
- (f) Carefully wrap one layer of rubber around the strain gauges and tie it down with a pipe clammer by applying 5 MPa pressure with a screw driver
- (g) Cure the adhesive for about 6 hours



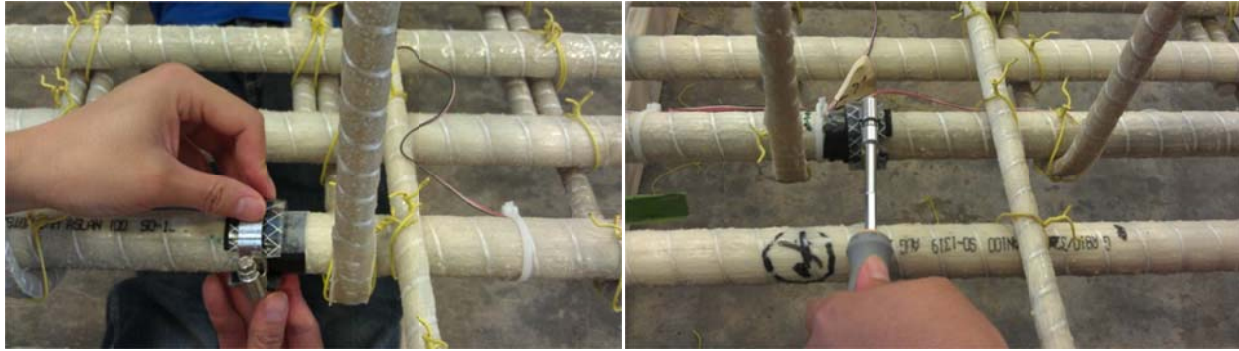
(a) Position each gauge by taping down lead wires (b) Fold up free end of the strain gauges



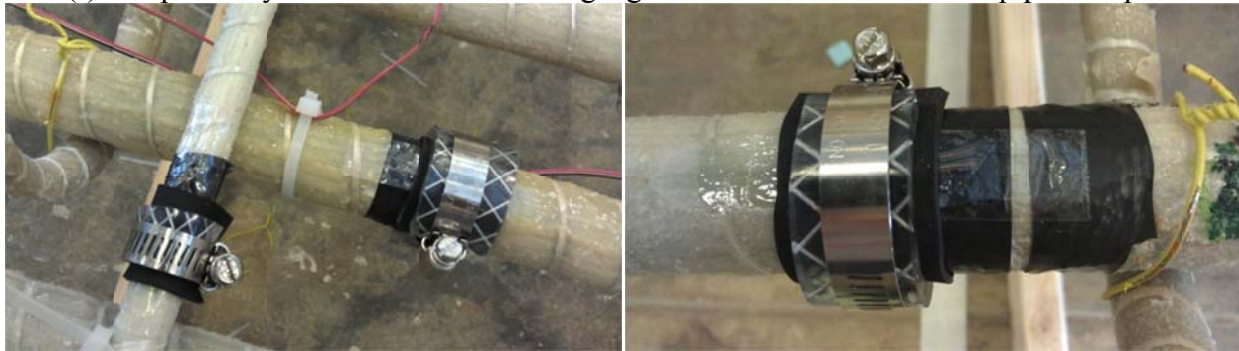
(c) Stir up resin for about 5 minutes and let it set for another 5 minutes



(d) Apply some resin on the smooth surfaces (e) Fold back and press down the gauges with foam



(f) Wrap one layer of rubber around the gauges and tie the rubber with a pipe clamer

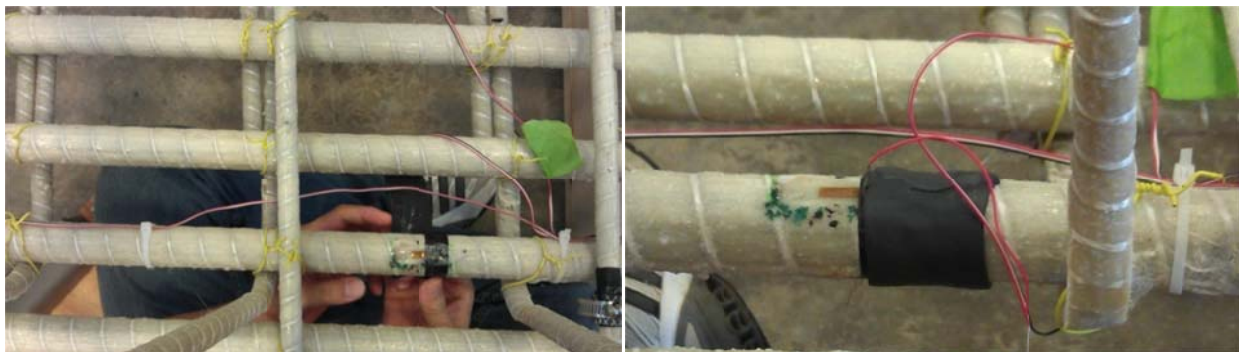


(g) Cure adhesives for about 6 hours

Figure 9.2: Installation of strain gauges

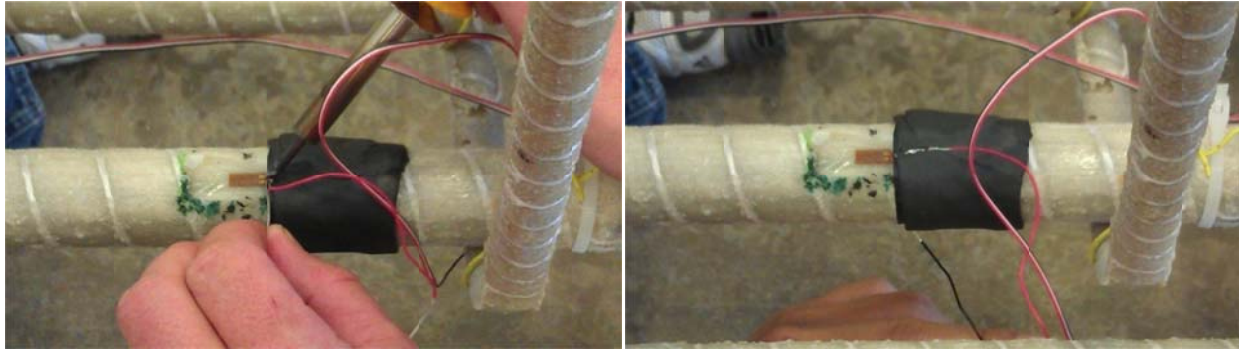
3. Soldering and protection of strain gauges

- (a) Untie the pipe clamer
- (b) Wrap an isolator around the FRP bar in front of lead wires of the gauges
- (c) Solder the wires to strain gauge leads
- (d) Press the soldered wires into the isolator to hold them in position
- (e) Solder the bottom strain gauge and other connections to create a half-bridge configuration
- (f) Seal all wires and joints using M-COAT rubber coating
- (g) Cover the strain gauges and all wires with a rubber tape
- (h) Protect the strain gauges and their wire connections with a durable plastic tape for long-term monitoring



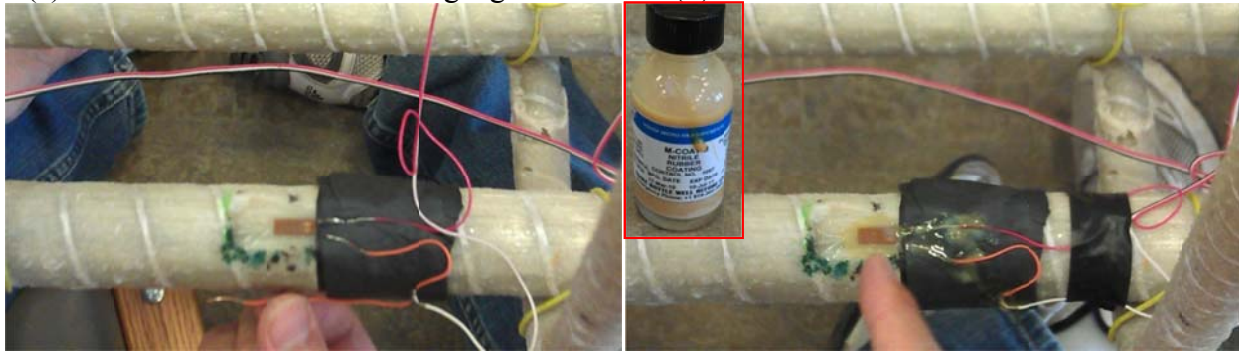
(a) Untie the pipe clamer

(b) Wrap an isolator around the bar in front of lead wires



(c) Solder the wires to the strain gauge leads

(d) Press soldered wires into the isolator



(e) Solder the wires to the bottom strain gauge

(f) Seal joints using Nitrile rubber coating



(g) Cover gauges and joints with additional rubber tape

(h) Protect gauges from disturbance with plastics

Figure 9.3: Soldering and protection of strain gauges